Fluidic-driven Cooling of Electronic Hardware
Part I: Channel Integrated Vibrating Reed
Part II: Active Heat Sink

A Dissertation
Presented to
The Academic Faculty

by

Donavon Gerty

In Partial Fulfillment
Of the Requirements for the Degree
Doctor of Philosophy in the
School of Mechanical Engineering

Georgia Institute of Technology

December 2008

Fluidic-driven Cooling of Electronic Hardware
Part I: Channel Integrated Vibrating Reed
Part II: Active Heat Sink

Approved:

Ari Glezer, Chairman
School of Mechanical Engineering
Georgia Institute of Technology

Donald Webster
School of Civil Engineering
Georgia Institute of Technology

Yogendra Joshi
School of Mechanical Engineering
Georgia Institute of Technology

Silas Alben
School of Mathematics
Georgia Institute of Technology

Marc Smith
School of Mechanical Engineering
Georgia Institute of Technology

Date Approved: August 20, 2008

This thesis is dedicated to my parents and sister who supported me thoroughly throughout the journey of graduate school and helped me to reach my goals.

ACKNOWLEDGEMENTS

First, I would like to thank my advisor, Dr. Ari Glezer, who has provided me with invaluable guidance and patience in completing this research. I would also like to thank the other members of my committee, Drs. Yogendra Joshi, Marc Smith, Donald Webster, and Silas Alben. Funding for this work was provided in part by NSF-ERC, DARPA MTO and Georgia Institute of Technology. I am also grateful for the additional financial support provided by the G.W.W. School of Mechanical Engineering. Also, the financial support of Mr. and Mrs. Warren Jobe, through the Achievement Rewards for College Scientists foundation, was much appreciated.

The role of secondary advisor has fallen to various lab members throughout the years, including Tom Crittenden, John Culp, Raghav Mahalingam, Bojan Vukasinovic, and Jelena Vukasinovic. Their advanced knowledge in various technical subject matters is truly astounding.

I am truly indebted to the ME machine shop run by John Graham and his never ending rotation of student workers. I doubt they truly realize how important they are to the completion of so many thesis projects.

My friends and labmates through the years have always been a source of entertainment, exploration, and stress release. Those of note are Philip Abramson, Adya Ali, Ulf Andresen, Prasad Bhave, Dan Brzozowski, Maria-Isabel Carnasciali, Zach Douglas, Dathan Erdahl, Dave Garth, Pierre Gerardin, Hanif Hunter, Chris Healey, Celine Lascar,

Thao Le, Anne Marie Lerner, Haifeng Li, Charlotte Kotas, Peter Nagy, Ashok Rajendar, Asim Nisar, Edison and Judy Rincon, Erick Rios, Aditya Sachan, Akiva Sklar, Vish Subramaniam, Steven Tillery, Emily Torres, Rachel Valade, Brett Warta, Paul Wickersham, the weekly volleyball group, and the American Pie Buckeyes. I especially want to thank Tim Koehler for his goofy friendship, and his low-rent condo.

Finally, I need to thank my parents and sister for all the support that they've given me through the years. It's beyond words how much it's meant…you've kept me who I am.

TABLE OF CONTENTS

LIST OF TABLES

LIST OF FIGURES

NOMENCLATURE

A	area, mm^2
A_c	total area of central cavity orifices, mm^2
$A_{c,v}$	total area of central cavity orifices plus vent area, mm^2
A_o	total area of outside cavity orifices, mm^2
$A_{p\text{-}p}$	peak to peak tip deflection, mm
Bi	Biot number, $\frac{hs}{k}$
c_p	specific heat, J / g K
C_p	coefficient of pressure, $\frac{P - P_{atm}}{0.5\rho_{air}U_{avg}^2}$
C_T	coefficient of thrust
d_{31}	piezoelectric coefficient, m / V
D_h	hydraulic diameter, mm
f_d	actuation frequency, Hz
f_{mod}	modulation frequency, Hz
f_{res}	resonant frequency, Hz
g	gravitational coefficient, 9.8 m / sec^2
$Gr^*_{x_{LE}}$	modified Grashof number
h	convective coefficient, W / m^2 K
h_o	height of channel, mm
H	total height of heat sink, mm
$H(t)$	heaving distance, mm
ΔH_r	head rise, Pa

k	thermal conductivity, W /m K
k_{air}	thermal conductivity of air, W / m K
KE_f	fluctuation kinetic energy, m^2 / s^2
L_a	channel length added, mm
L_r	length of reed, mm
$\dot{m}$	mass flux, kg / s
N	image pairs
Nu	Nusselt number, $\frac{hD_h}{k_{air}}$
Pr	Prandtl number of air, 0.7
q''	heat per unit area, W / m^2
Q	volume flow rate, m^3 / s (CFM)
Q''	average heat flux per unit area, W / m^2
Q_{st}	steady flow rate, m^3 / s
P	pressure, Pa
Re	Reynolds number, $\frac{\rho \overline{U} h_o}{\nu}$
s	thickness, mm
St	Strouhal number, $\frac{fA_{p-p}}{U}$
t	time, sec
t_r	reed thickness, mm
T	actuation period, sec
T'	thrust per unit width, N / m

T_{ex}	exit temperature, °C or K
$\Delta T_{rise,avg}$	average temperature rise, °C or K
T_s	surface temperature, °C or K
T_{surr}	temperature of surroundings, °C or K
T_∞	ambient temperature, °C or K
U, V	streamwise and cross-stream velocity, m / s
$u'u', v'v', u'v'$	Reynolds stresses, m^2 / s^2
V_i	input voltage, V
V_{max}	maximum input voltage, V
w	width, mm
w_o	standard channel width, mm
w_r	width of reed, mm
Y	Young's modulus of elasticity, N / m^2
x, y, z	*streamwise, cross stream, and spanwise location*, mm
x_s	reed separation distance, mm
x_w	shedding wavelength, mm

Greek Symbols

$\alpha(t)$	angle, degrees
β	Boussinesq approximation, 1 / K
ε	average surface emissivity
λ	wavelength, nm
ω	angular frequency, 1 / rad

v	kinematic viscosity, kg / m s
ρ_a	air density, kg / m^3
ρ_f	electrical resistance, $\Omega\, m$
ρ_r	reed shim density, kg / m^3
σ	Stefan-Boltzmann constant, 5.67×10^{-8} W / m^2 K^4
$\Delta\Phi$	phase difference, degrees
$\tau_{x_{1,2}}$	shear stress, N / m^2
Θ	thermal resistance, K / W
Θ_o	thermal resistance of LBHS, K / W
Θ'	dimensionless temperature

Subscripts

amb	ambient
cond	conduction
conv	convection
max	maximum
min	minimum
nat	natural convection
prop	propagation
o	nominal
O	origin, tip of reed
rad	radiation
tot	total

SUMMARY

Enhanced heat transfer in electronic hardware by direct, small-scale actuation is investigated experimentally in two test bed configurations. In Part I of this work, a method for cooling compact electronics that exploits the unsteady motions induced by a vibrating reed embedded within a heated duct (in contact with hardware that needs cooling) to enhance forced convection transport heat from the duct surfaces is introduced. The time-harmonic oscillations of the PiezoElectric Reed (PER) induce a reverse Kármán vortex street through the channel, introducing small scale motions throughout the length of the duct. The flow characteristics of this device are investigated with PIV for various reed operating conditions, including placing two reeds in tandem and in parallel. The effect of altering the channel configuration is also determined. For high heat flux applications, an externally induced bulk flow can be augmented by the small scale motions induced by the reed.

The small scale motions enhance the heat transfer over that of conventional time invariant flows at similar or higher Reynolds numbers. The vibrating reed helps to disrupt the thermal boundary layer as well as fully mix the heated fluid near the wall with the cooler core flow. In both the presence or absence of an externally induced core flow, streamwise distributions of local Nusselt number indicate that the heat transfer can increased by a factor of two.

In Part II of this work, the effect of small scale motions induced by a synthetic jet on heat transfer within an advanced heat sink is investigated. The synthetic jet module is optimized and several flow configurations are tested. The optimal design directs the

synthetic jets to emanate directly through the base of the heat sink and induce a recirculating flow between the fins. This results in a lower thermal resistance than what is typically achieved with traditional fans at the same flow rate.

Chapter 1

Introduction and Literature Review

Enhanced heat removal by direct actuation of small scale fluid motions is investigated in two configurations. In Part I (Chapters 2-4), small scale motions are induced by a vibrating reed within a heated duct to enhance forced convection from the duct surfaces in the presence and absence of a core flow. The time-harmonic oscillation of the reed results in the regular shedding of vortical structures that lead to small-scale mixing. Part II (Chapter 5) focuses on enhanced heat transfer within an active heat sink by small scale motions that are induced by an array of synthetic jets. The jets emanate directly through the base of the heat sink and lead to a recirculating flow between the fins, resulting in higher convective heat transfer than can be attained with conventional fan

1.1. Flow Locomotion by Vibrating Surfaces

A heated duct ejector comprises a conductive thin wall duct which is attached to heated elements and uses an internal air stream to transport the heat to the ambient. This approach to heat removal is of particular interest for compact electronic equipment where higher capacity cooling is necessitated by increased processing power which may not be handled by natural convection.

The present work focuses on the investigation of forced convection heat transfer within a high aspect ratio, millimeter scale height channel. A unique feature of this configuration is that the flow is driven by a vibrating reed. This device consists of a cantilevered reed with thin piezoelectric ceramic plate elements bonded to the surface. In the absence of

bulk flow, the time harmonic motion of the Piezoelectric Reed (PER) results in thrust and net flow through the duct. The flow is characterized by time-periodic shedding of vortices of alternating sense that increase the local heat transfer compared to steady flows at the same Reynolds number.

The fundamental mechanism of the flow induced by a vibrating plate is outlined by Lighthill (1971) as part of the discussion of fish propulsion where the thrust force is derived from the movement of the tail. This motion changes the momentum of the surrounding water in a direction that is normal to the spine with a magnitude that is equal to the product of virtual mass of the water (m_f) and the local normal velocity of the tail, (w_f). The total thrust is obtained by considering the rate of change of momentum within a volume that includes the fish and the surrounding fluid. The calculation can be simplified considerably by including the volume surrounding the fish without the complex vortical structures within the wake. Lighthill showed that the mean thrust, $\overline{T}$, is

$$\overline{T} = \left[\overline{m_f w_f \left(\frac{\partial z}{\partial t} - 0.5 w \frac{\partial x}{\partial a} \right)} \right]_{a=0} \tag{1.1}$$

where a is the distance from the tip of the fish's tail, along the spine. This analysis can be related to the motion of the vibrating reed that is discussed in Part I of this thesis. Because the reed is stationary, the thrust produced in this manner is imparted to the air surrounding the reed and induces a net flow.

The locomotion of fish uses a "flapping" motion that sheds vortices similar to the PER, as shown schematically in Figure 1.1. Fish use this motion for continuous production of thrust or bursts of short duration forces for maneuvering (Triantafyllou et. al., 2000).

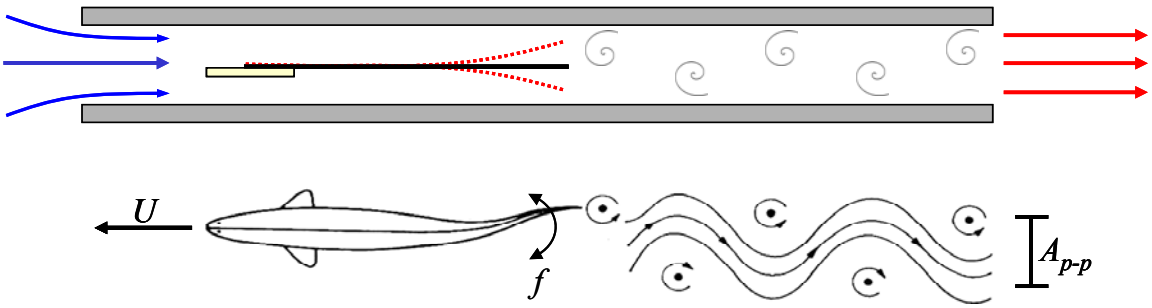

Adapted from Lighthill (1969)

Figure 1.1: Comparison of reverse Kármán vortices created by PER motion and carangiform motion of fish

Many scientists have studied the correlation between the hydrodynamics and propulsion methods of fish, eels, aquatic mammals, etc., and engineering principles. Most aquatic animals use one of two forms of body motion for propulsion: anguilliform or carangiform (Lighthill, 1960, 1969). Eels use anguilliform motion for propulsion where the entire body undulates, although the amplitude may increase along the body. Lighthill (1969) showed that undulation of the entire body does not result in efficient propulsion. Carangiform motion is used by most classes of fish and aquatic mammals and consists of movement mostly in the posterior half or third of the animal. Carangiform motion provides the same thrust as the anguilliform motion and improves efficiency because the fluid is accelerated over a shorter distance and parasitic losses are reduced by eliminating vortex formation that is created in anguilliform motion at the vertices upstream of the trailing edge of the fish. One reason carangiform motion is highly efficient is because the

majority of motion is confined in the posterior regions where the fish mass is low (Lighthill, 1960). The reed does not completely conform to carangiform motion, but it is possible to control the magnitude and distribution of its mass to optimize efficiency.

The flow around biomimetic foils has been investigated to aid in modeling the flow produced by aquatic animals. Biomimetic foils are airfoils designed to mimic the fins of biological organisms. Anderson et al. (1998) varied the angle of attack (α) and Strouhal (St) number of an oscillating airfoil to obtain distinctly different patterns of vortex shedding and measured the thrust and efficiency. The maximum thrust was found when $0.25 < St < 0.4$ and $15° < \alpha < 25°$. The highest efficiency is obtained when the heave amplitude is comparable to the chord length, the angle of attack is high, and St is sufficiently high to produce a reverse Kármán vortex street (where the sense of the shed vortices is opposite to the vortices in the wake of a stationary cylinder). They observed a reverse Kármán street for $\alpha < 50°$ and $0.2 < St < 0.5$. The PER operates at $St \approx 0.45$ and it angle of attack is estimated as 6.3°. Increasing St results in the formation of more vortices per cycle but this results in a degradation of thrust. A reverse Kármán vortex street was also observed by Lighthill (1969), Triantafyllou et al. (2000), and Gopalkrishnan et al. (1994).

The flow induced by heaving airfoils has been investigated for many years (Theodorsen, 1934). An airfoil, heaving with amplitude $H(t)$ and angle of attack $\alpha(t)$, creates both lift and pitching moment. As shown in Equations 1.2 & 1.3 (Hodges and Pierce, 2002), in quiescent air, when the airfoil first begins to move, $U = 0$, but the resultant lift and moment are not zero, inducing air motion around the airfoil.

$$L = 2\pi\rho_\infty UbC(k)\left[\dot{H}(t) + U\alpha(t) + b\left(\frac{1}{2} - a\right)\dot{\alpha}(t)\right] + \pi\rho_\infty b^2\left(\ddot{H}(t) + U\dot{\alpha}(t) - ba\ddot{\alpha}(t)\right) \quad (1.2)$$

$$M_{\frac{1}{4}} = -\pi\rho_\infty b^3\left[\frac{1}{2}\ddot{H}(t) + U\dot{\alpha}(t) + b\left(\frac{1}{8} - \frac{a}{2}\right)\ddot{\alpha}(t)\right] \quad (1.3)$$

Similar to the biomimetic studies, the flow around pitching and heaving plates has also been studied in air. Bürmann et al. (2002) present images of flow induced by a vibrating plate directed normal to a surface. Ihara and Watanabe (1994) placed a vibrating plate in still air and visualized the vortices rolling off of the tip and measured the volume flow rate of the induced flow achieved. They also investigated the effect of placing two vibrating plates near each other and actuating them in-phase and out of phase. They determined that the volume flow rate induced by two plates is greater than twice the volume flow rate induced by a single plate vibrating in free air, with the in-phase operation slightly more effective.

In this work, the effect of placing two vibrating plates is tandem is investigated because it has been shown that a vibrating plate can affect the strength and propagation of vortices that are generated farther upstream. Gopalkrishnan et al. (1994) showed that it is possible to reposition and change the vortex strength. They found three modes of interaction: 1) an expanding wake when the initial vortices and newly generated vortices pair up; 2) destructive interaction when a vortex of the incoming flow merges with a newly formed vortex of opposite sense and cancel each other; and 3) constructive interaction when an incoming vortex merges with a generated vortex of the same sign and forms a stronger

vortex. The spacing between the vortex generator creating the initial vortex street and the trailing edge of the pitching airfoil is the governing parameter for the different modes. In all cases, the foil chord must be of comparable length to the dimension of the oncoming vortex because shorter foil chords are ineffective. Zhu et al. (2002) also performed experiments that showed how a fish is able to improve its thrust capability by using its tail fin to increase the strength of the vortex initially shed by the fish's dorsal fins. Similarly, Akhtar and Mittal (2005) showed how a vortex shed from the dorsal fin improves the thrust and moment coefficients and is more efficient than a single foil (tail fin only). The improvements can be furthered by fine tuning the phase difference between the shed vortex and the tail motion.

1.2. Heat Transfer Enhancement by Unsteady Flows

An important aspect of the present approach is that the unsteady flow induced by the PER in a channel can result in higher heat transfer than with steady flow. Enhanced heat transfer is achieved by small-scale motions near the heated surface disrupting the thermal boundary layer and by enhanced mixing with the core flow. Increased small scale mixing, and therefore enhanced heat transfer, in channel and flat plate flows can be achieved by shedding of vortices from vortex generators, vibrating plates, etc. Li (1996) performed numerical calculations to determine the variation of Nusselt (*Nu*) number when a square cylinder is placed in a channel flow. He compared *Nu* in the presence and absence of the cylinder, and noted the effect of cylinder orientation and the cylinder-wall gap. He was able to obtain an increase of 42% in *Nu* over a channel without the cylinder.

Vortex generators are typically created by placing a small protrusion in the channel wall that leads to the formation of either a single sign or counter rotating streamwise vortices along the surface. These vortices help to transport high-speed fluid towards the surface and lower-speed fluid away from the surface thereby improving heat transfer. The shape, inclination angle, orientation, pattern, etc. of vortex generators has been investigated in a number of earlier works. Tanaka et al. (2003), Tiggelbeck et al. (1991), Edwards and Alker (1974), Russell et al. (1982), Fiebig et al. (1989), Zhu et al. (1993), Biswas et al. (1996) and Turk and Junkhan (1986) investigated the effects of various vortex generators on heat transfer in channel flow. Tiggelbeck et al. (1991) found an increased local *Nu* of nearly six times immediately downstream from a pair of delta wing shaped vortex generators. The global increase is near 60%. He also determined that the increase is linear with *Re*. Zhu et al. (1993) presented flow visualization and heat transfer results for several configurations of vortex generators, showing an 35% increase in *Nu*. Brockmeier et al. (1989) showed that turbulence generators improve the heat transfer as both *Re* and angle of attack increased, and the improvement was measured even 18 channel heights downstream. Blackwelder et al. (1998) investigated the effects of a piezoelectrically driven plate that was mounted flush with the surface and oscillated into the flow. The motion of the plate produced small scale vortices that were generated on command. Although not studied, this concept could be used to increase heat transfer when necessary without creating a substantial increase in pressure drop. Sano (2003) created a different type of vortex generator by placing a flat plate into the center of a channel. He varied the physical dimensions, shape, and location of the flat plate and determined that a thin body close to the surface increases the cooling performance.

Vibrating plates also introduce the unsteady mixing and enhanced heat transfer. The concept of using a PER to introduce controlled vortices near the surface has only been superficially investigated. Schmidt (1994) used two piezoelectric reeds 3.38 cm apart vibrating 180° out of phase to create a jet normal to a heated vertical surface and determined the local and average heat transfer coefficients. He showed that the heat transfer obtained from the piezoelectrically driven jet is equivalent to that of a conventional jet of much higher *Re*. Similarly, Kimber et al. (2007) also investigated the localized effects of using a piezoelectric reed mounted normal to a heated surface. They obtained a maximum $Nu \approx 45$. Açikalin et al. (2005) placed a piezoelectric reed adjacent to a heat sink and measured the increase in heat transfer performance for various configurations. They also installed several PERs within a laptop computer which already had a conventional fan. After reaching steady state temperature using only the fan, the PERs were activated and the decrease in the temperature of the processor was noted. Açikalin et al. (2005) also noted the differences in thermal resistance and heat transfer coefficient for tangentially cooling a simulated electronic die by varying the horizontal and vertical spacing between heat source and tip of the piezoelectric reed.

Pulsatile flow in a channel has been shown to increase the heat transfer over steady flow. Moon et al. (2005) investigated the effect of jet pulsing frequency for cooling an array of heated blocks in a channel. The *Nu* increased with increasing *St* until $St = 1.16$ where it then decreased. They also achieved a *Nu* 30% higher for the pulsatile flow over steady flow near the inlet of the channel. Farther down the channel the increase diminishes. Olayiwola and Walzel (2008) investigated the correlation between the fluid flow and heat

transfer for pulsing channel flow. They found a 250% enhancement in heat transfer at the $Re \approx 550$, with little enhancement for very low or high Re.

The author is unaware of earlier work in the archival literature that has demonstrated the effect of a vibrating reed on confined flows including heat transfer effects.

Chapter 2

Experimental Apparatus and Techniques

The study of the ducted heat ejector encompasses fundamental fluids and heat transfer processes and are the focus of the present investigation. As discussed in §1.1 the thrust produced by the vibrating reed induces flow through the channel and is accompanied by the formation of a train of vortices. The first part of the current work focuses on the mechanics of the induced flow. The ultimate goal is to assess the improvement in heat transfer that is enabled by the induced unsteady flow. The effects of PER configurations and operating conditions are examined, as well as the channel configuration for both the fluid dynamics and heat transfer investigations.

2.1. PER Design and Construction

The design criteria of both components of the ducted heat ejector, the channel and the PER, were driven by its proposed implementation in small-scale electronic hardware. In the present investigation the maximum height of the channel, h_o, was limited to 7.62 mm and width, w, of 27.6 mm and the reed's resonant frequency, f_{res}, was kept within the inaudible range, less than 100 Hz.

The basic design of the PER consists of a thin, vibrating cantilevered beam. The design uses a shim material bonded with a piezoelectric ceramic plate to create a unimorph structure as shown in Figure 2.1. A bimorph structure is created by bonding piezoceramic on both sides of the shim and is used where greater force is required to move the reed When a sinusoidal voltage is applied across the piezoelectric electrodes the plate and

contracts and due to the bonding, transfers shear to the metal shim which causes bending and displacement of the free end of the shim. The reed is typically operated at the resonant frequency of the unimorph (or bimorph) cantilever.

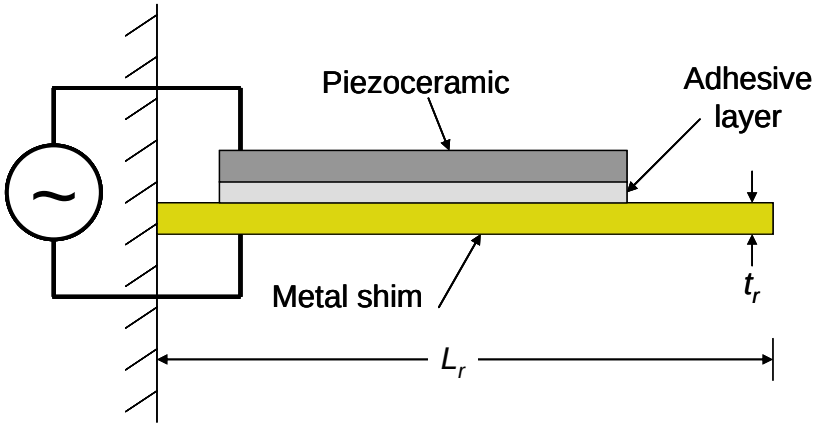

Figure 2.1: Schematic of unimorph

The present investigation utilized PZT-5H (Lead Zirconate Titanate) due to its high elongation properties at relatively low voltage input. The piezoceramic plates are 0.127 mm thick and have a maximum input voltage of 8 V_{RMS} / mil (V_{max} = 40 V_{RMS}). The bonded reed required up to 14 mA (or up to 200 mW). The footprint of the piezoceramic plate measured 23 × 23 mm. The reed was made from 0.154 mm thick brass, 25.4 mm wide and 40.6 mm long. A scaled drawing is shown in Figure 2.9.

Toda (1979) performed theoretical calculations of a resonant bimorph and calculated the performance characteristics of the reed. He studied the tip's deflection and velocity, and the velocity of the induced air flow. The air velocity normal to the length of the reed (along the arc of movement) is proportional to the tip velocity. The air flow parallel to the length of the reed is inversely proportional to the reed length. Yao and Uchino (2001)

also performed analytical calculations of displacement and frequency performance for a bimorph PER. They characterized the tip displacement as a function of resonant frequency, input voltage, and reed length. Mathew et al. (2006) performed theoretical calculations to parametrically study the effect of material stiffness, thickness, density, piezoceramic plate length, and overall length. Açikalin et al. (2003) numerically calculated the 2-D velocity field induced by PER.

The governing equations of a cantilevered beam were used to guide the selection of the shim material and PER size. The analysis performed by Timoshenko (1955) and later summarized by Jacobson (1995) was used (see Appendix A). Several parametric studies are shown in Figure 2.2 and Figure 2.3. The piezoceramic plates were included in these calculations. Using this analysis, along with the desired dimensions and ensuring that the resonant frequency remained < 100 Hz, 0.15 mm thick brass was selected as the shim material. The thickness of brass was not reduced any further because the material had to remain stiff enough to support the piezoceramic plate. The length of the shim, L_r, was selected to be 40 mm. The analysis also showed that the resonant frequency has no dependence on PER width, as long as the widths of the shim and ceramic are approximately equal. A rectangular reed has been the standard design for all of the present experiments because Yoo et al. (2000) tested several reed shapes and materials at constant resonant frequency and found that a rectangular shim with a constant aspect ratio produces the largest tip displacement.

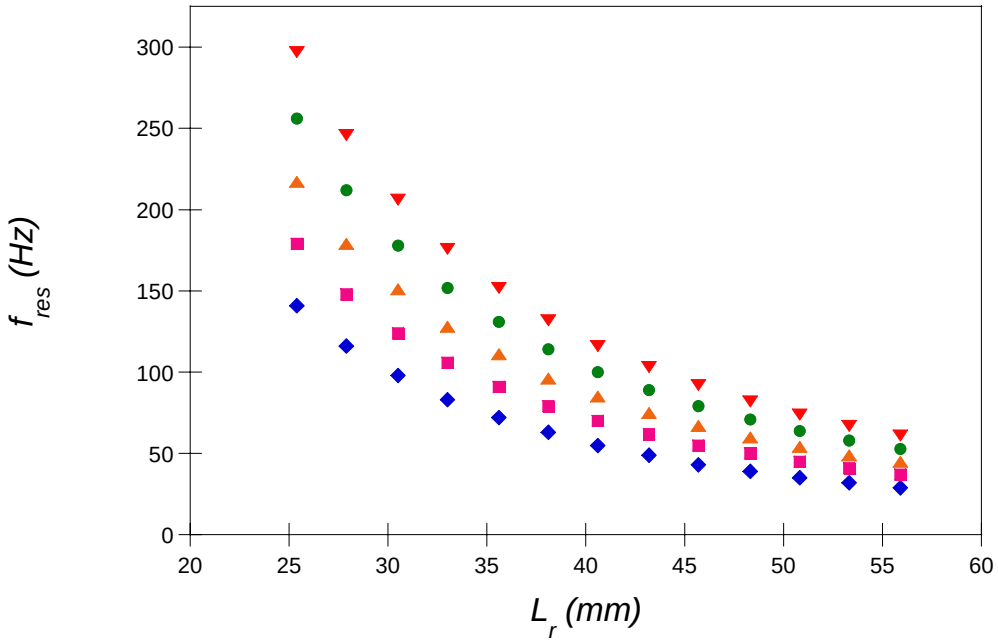

Figure 2.2: Variation of PER resonant frequency with reed length, using brass, for t_r = 0.05 mm (◆), 0.10 mm (■), 0.15 mm (▲), 0.20 mm (●) and 0.25 mm (▼)

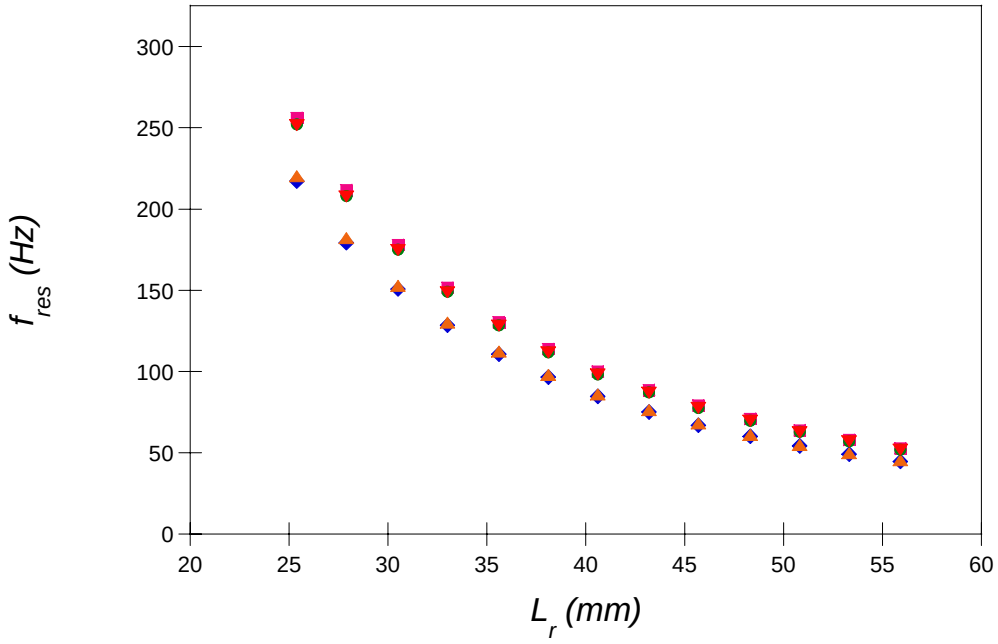

Figure 2.3: Variation of resonant frequency with reed length for various shim materials (t_r = 0.15 mm); brass (◆), copper (▲), aluminum (■), steel (●), and Inconel 600 (▼)

The process for manufacturing the PER devices was standardized to help minimize variability between devices. The brass shim was cut from flat stock material using an electrical discharge machine (EDM) to ensure the shim remained flat. The piezoelectric sheets were scored and cut with a diamond tip scribe. Several sizes of piezoceramic were tested, and it was found that covering half of the shim achieved the maximum deflection. Each piezoelectric plate was cut into several smaller elements to prevent excessive stresses that could crack the material. The piezoelectric elements were bonded to the shim material with spacing between them (each reed has two elements 2.5 mm apart) with adhesive for relatively high tensile lap shear at elevated temperatures (2320 psi at 100°C). A fixed weight placed on the piezoelectric elements during the curing process ensured consistent compression and an approximately similar bond line thickness

Several methods were employed to measure the deflection of the reed. First, a laser vibrometer is used when the top of the reed is visually accessible. For experiments where only the side of the reed is visible (such as PIV experiments), the deflection was manually measured using a traversable telescope with a Vernier scale. Figure 2.4 shows the comparison between the sinusoidal input signal and the average displacement of the reed tip for one cycle in free air, as measured with the vibrometer. The deflection (dashed line) and the input signal (solid line) do not show any appreciable phase difference. Figure 2.5 shows the total peak to peak deflection of the reed along its length, L_r = 40.6 mm. These data shows that the majority of the reed's bending occurs near the mounted end of the PER. Figure 2.6 shows that there is only a small amount of deflection across the width of the reed. This is because the piezoelectric plate covers 90% of width, adding stiffness and not allowing for bending in this direction. Figure 2.7 shows that

there is a linear increase in $A_{p\text{-}p}$ with increasing input voltage ($A_{p\text{-}p} / h_o = 0.75\ V_i / V_{max}$). The piezoelectric constant, d_{31}, determines the elongation of the ceramic per unit voltage. This is a linear function of input voltage, until the maximum voltage is exceeded when the piezoceramic then becomes unpoled. The spectral power of the airflow induced by the vibrating reed was measured using an uncalibrated hotwire probe. Figure 2.8 shows the power spectrum of the airflow, measured 25 mm from the tip of the reed. The resonant frequency of the reed was 73 Hz and the spectral power shows a spectral component at this frequency. There are several other harmonics at higher resonant multiples, but with lower spectral powers. The first harmonic is the result of two vortices being created in each cycle of the reed vibration.

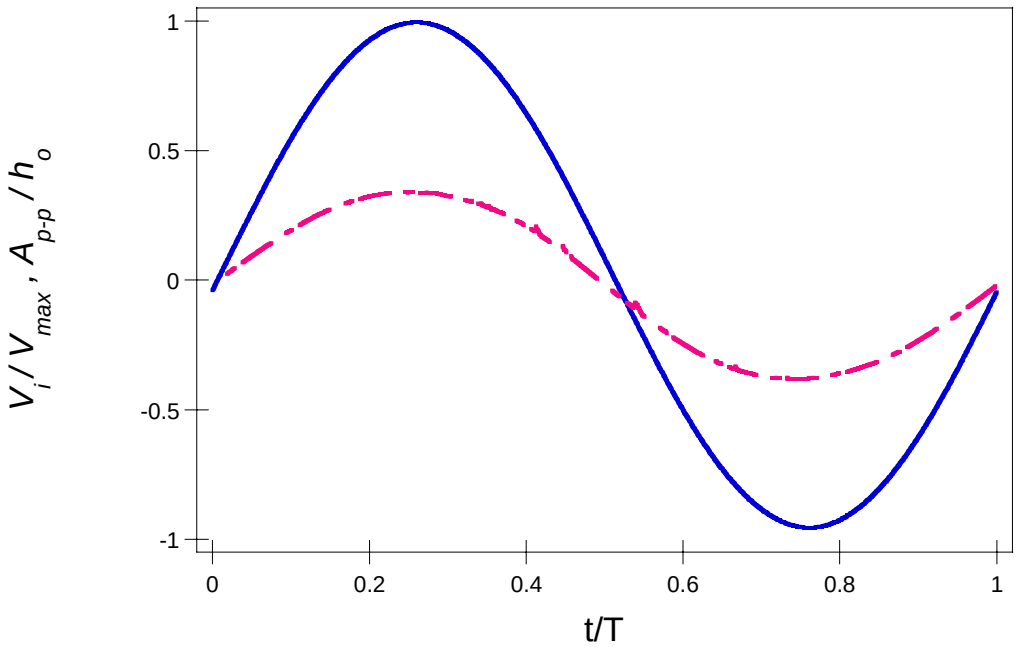

Figure 2.4: Sinusoidal input voltage and average deflection of tip of reed for one cycle, signal input (solid), deflection (dashed) (f_d = 73 Hz)

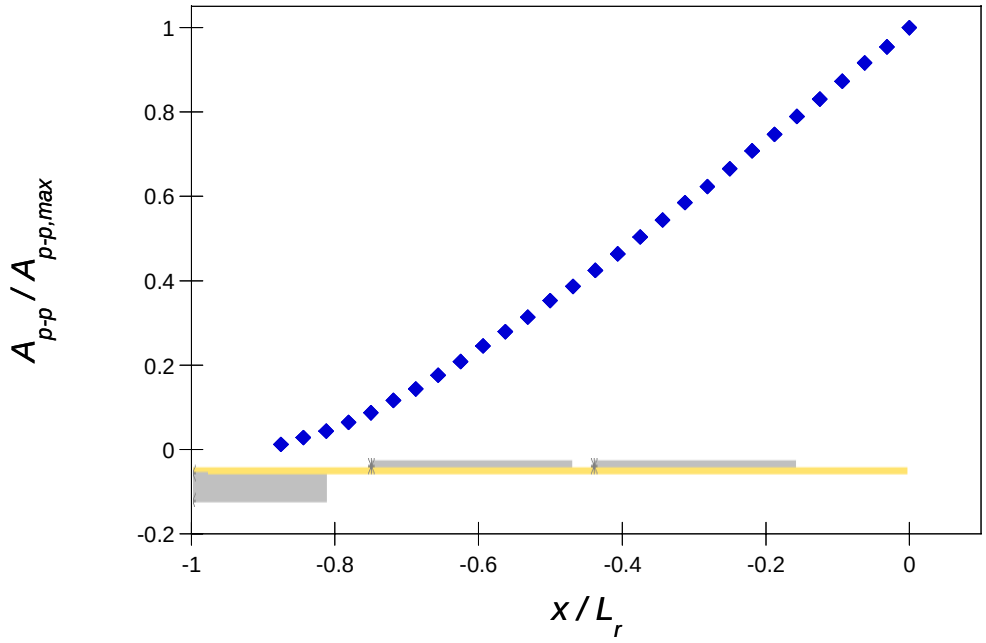

Figure 2.5: Deflection of PER along the axial length along with corresponding diagram of PER, (L_r = 40 mm, $A_{p\text{-}p,\,max}$ = 5.76 mm)

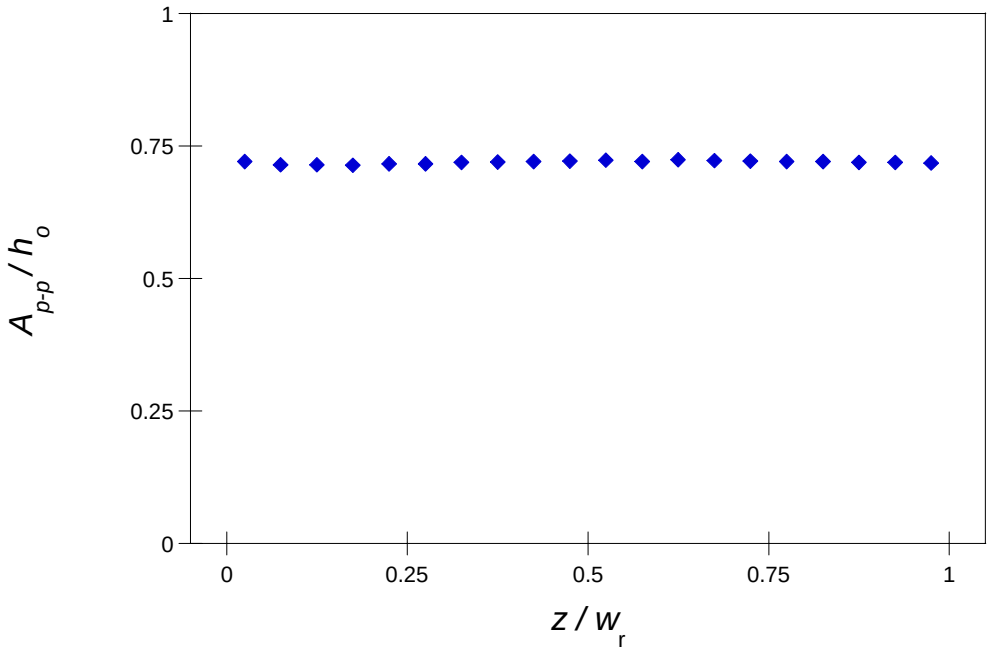

Figure 2.6: Deflection of reed tip across its width (w_r = 25.4 mm)

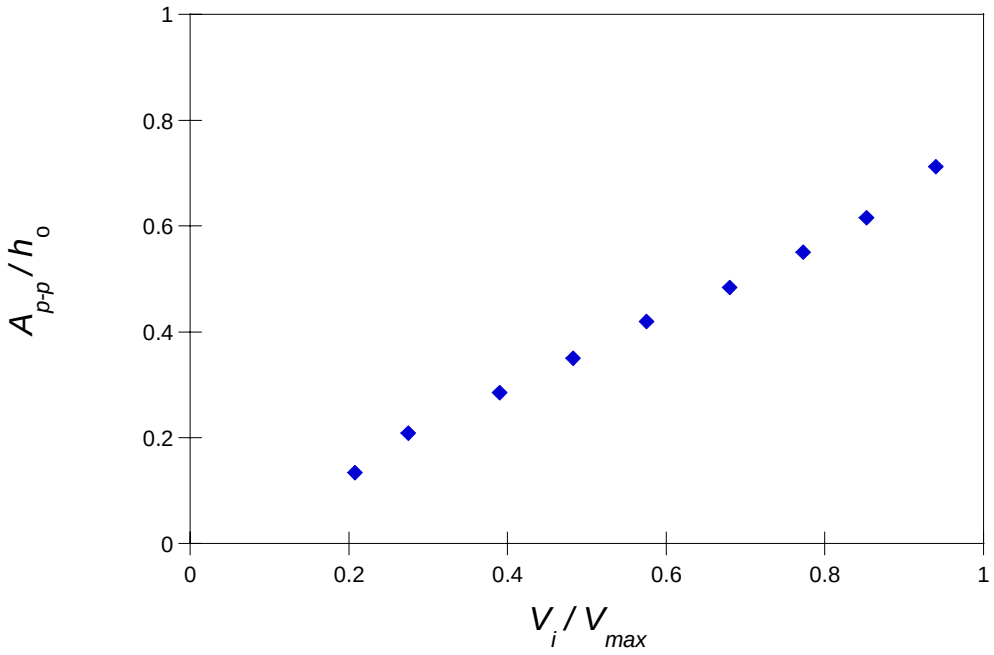

Figure 2.7: Peak to peak amplitude of the PER tip with increasing input voltage (h_o = 7.62 mm, V_{max} = 40 V)

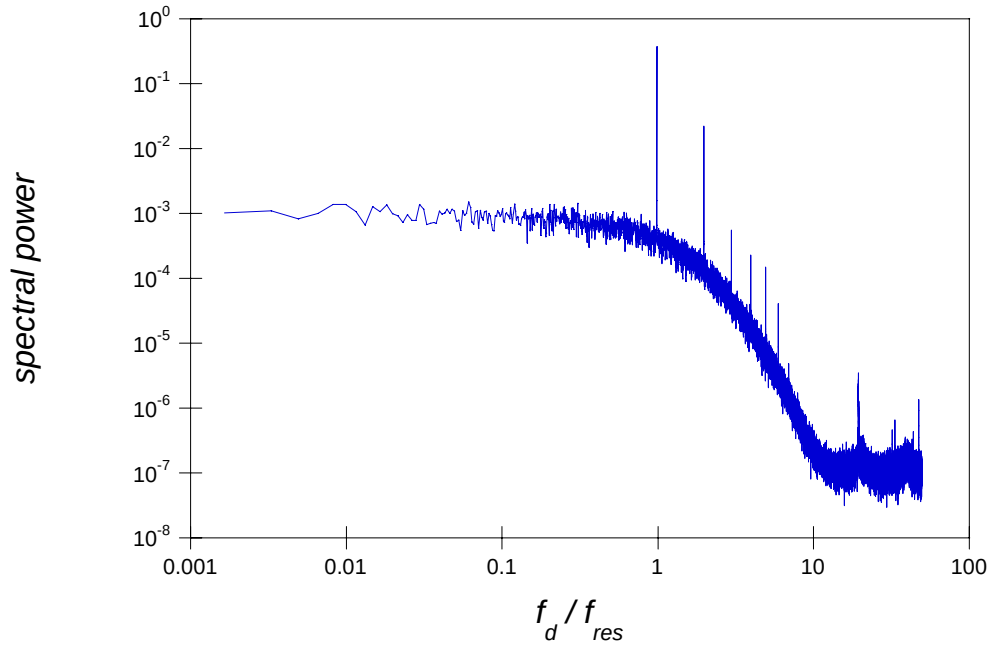

Figure 2.8: Spectral power of reed-induced flow versus frequency (f_{res} = 73Hz)

There have been several numerical studies completed to characterize and optimize the flow created by a PER through varying the design parameters. Cattafesta III et al. (2001) compared their numerical simulation to experimental results and showed remarkable similarity. They optimized the dc response and frequency of the PER in relation to the stiffness ratio of piezoceramic to shim, thickness ratio, density ratio, and piezo length. Mathew et al. (2006) performed similar investigations. Although these results were not used in the design of the PER, their results reinforce some of the design parameters that were selected, especially that the optimal piezoceramic plate length = 0.5 L_r.

The affect of the resonant frequency on the total volume flow rate was beyond the scope of this project, but from theoretical equations, it can be shown that the volume flow rate per time depends linearly with frequency for a constant $A_{p\text{-}p}$. Toda (1979) states that the volume flow rate of the air induced by the reed is:

$$\dot{Q} = A_{p-p} w \left[B \left(d_{31} V \frac{\rho_r}{\rho_a} \right)^{\frac{1}{3}} \left(\frac{Y}{\rho_r} \right)^{\frac{1}{2}} \frac{t_r}{L_r} \left| \cos(\omega t) \right| \right] \tag{2.1}$$

where B is a constant involving several factors, including the mechanical efficiency, V is the applied voltage, ρ_r is the composite density of the reed, ρ_a is the density of air, Y is the composite Young's modulus of the reed, t_r and L_r are the thickness and length of the reed respectively, and ω is the angular frequency based on resonance. When this equation is integrated with respect to time (and condensing terms),

$$\int_0^T \dot{Q} dt = C \frac{\sin(\omega t)}{\omega} = D * f \,, \tag{2.2}$$

it is clear that that the total volume flow is a linear function of frequency when all other terms are held constant. Altering the frequency, while keeping the other parameters constant, is hard to achieve though because many of the parameters are coupled with the resonant frequency.

The flow induced by the reed clearly depends on its construction and placement within the channel. As noted above, the reed's manufacturing procedure was standardized in an effort to minimize variation between devices. While the typical variations in the resonance frequency where within 10 Hz, the resonance frequency changes slowly with time due to microscopic cracks in the epoxy bondline and the piezoceramic material, which cause a reduction in the stiffness of the beam and therefore in f_{res}. When a reed is first constructed, this reduction is rapid ($\Delta f_{res} \approx 20$ Hz in one hour of operation), but after several hours the change is less than 1 Hz over 10 hours of operation. During the thermal experiments, the stiffness changes somewhat due to heating but can be compensated for by measuring $A_{p\text{-}p}$.

The repeatability of the measurements is also affected to some extent by the reed's placement and orientation within the channel. The reed's angle with respect to the channel's walls could vary by 1.5° resulting in a maximum vertical displacement of the tip relative to the center of the channel by about 1 mm and consequently a slight change in the flow symmetry, as shown for example in Figure 3.5.

2.2. Channel Design

The modular channel design is comprised of four separate walls as shown in Figure 2.9. The sidewalls of the channel are made from clear polycarbonate to allow visual access for particle image velocimetry (PIV), which is discussed further in §2.3. The channel height can be varied, but in all present experiments the height of the channel is held constant at h_o = 7.62 mm. The reed is cantilevered in the center of the channel using small diameter (4.8 mm) spacers. The top wall could be instrumented with a plate that has static pressure ports at the spanwise centerline at various streamwise locations, as specified in Table 2.1. The length of channel could be increased using extensions manufactured using stereolithography (SLA) fabrication. These extensions also had static pressure ports placed along their length. The inlet to the channel had an interchangeable SLA piece that allowed the entrance to be changed from a standard 90° corner to a rounded bellmouth to reduce inlet head loss.

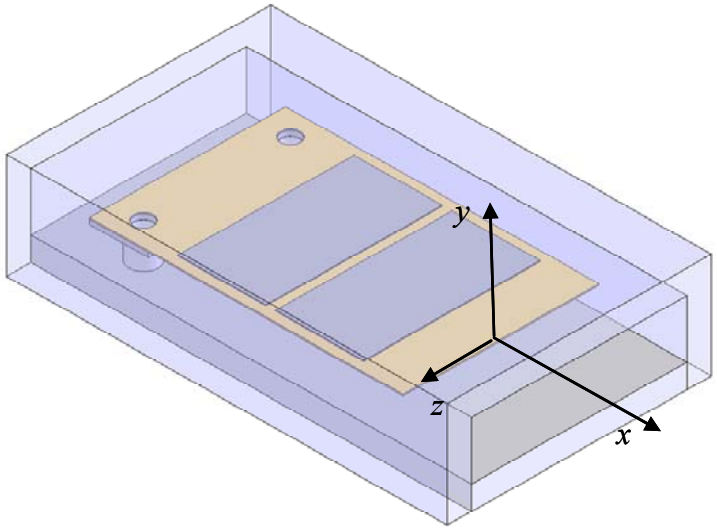

Figure 2.9: Overview of PER mounted in the channel

Table 2.1: Static pressure port locations in relative to the downstream tip of the reed

Port	Distance from tip (mm)	Port	Distance from tip (mm)
1	-40.64	12	-12.70
2	-38.10	13	-10.16
3	-35.56	14	-7.62
4	-33.02	15	-5.08
5	-30.48	16	-2.54
6	-27.94	17	0.00
7	-25.40	18	2.54
8	-22.86	19	5.08
9	-20.32	20	7.62
10	-17.78	21	10.16
11	-15.24	22	12.70

2.3. Particle Image Velocimetry

Particle image velocity (PIV) computes the in-plane velocity components via a statistical determination of the displacement of particles (Adrian, 1991). In the present investigation, spatial distributions of the streamwise (U) and cross stream (V) velocity components are measured in cross-stream (x-y) planes An in-depth description of the experimental technique (including pre- and post-processing of the data) can be found in Honohan (2003).

A dual-processor PC with 2 gigabytes of RAM running TSI software is used to acquire images and compute the velocity fields. The flow is illuminated using a dual head, 50 mJ per pulse, frequency-doubled ($\lambda = 532$ nm) Nd: YAG laser. The laser beams are focused into a thin sheet using cylindrical and spherical lenses. The lenses are mounted on optical rails so that their spacing can be precisely controlled, and the sheet is steered into the test section. The optics allow the sheet height and focal point location to be altered (for use in multiple experimental setups). The flow is seeded using smoke particles. Images of the flow field are captured using a 1000×1016 pixel CCD camera with 8-bit intensity resolution, positioned using a three-axis traverse. A Navitar Zoom 6000 II lens is used with variable zoom to obtain image magnifications as low as 2 μm / pixel. Master timing of the experiment is performed using a TSI Synchronizer allowing image separation times as short as 600 nanoseconds when operating in double-frame, single exposure mode. The synchronizer also accepts an external trigger signal, enabling the acquisition of phase-locked or conditionally sampled data.

Both phase-locked and time-averaged PIV data sets are acquired. The time-averaged flow field can be computed from the ensemble average of the phase-averaged field. Time-averaged fields are also computed by selecting the trigger frequency such that the acquired image pairs are equally distributed over the actuation cycle (to ensure unbiased estimates for the mean quantities). This is accomplished by purposely aliasing n complete cycles over N image pairs, where N is sufficiently large to determine the mean quantities to the desired uncertainty, and n is an arbitrary integer. In all cases, a function generator is used to input a TTL trigger signal to the synchronizer at the proper frequency (and phase in the case of phase-locked data). In most of the phase-locked cases, the starting phase was nominally chosen when the PER reached the upper apex of it motion. This was done using the images during PIV setup.

The PIV images are pre-processed in order to remove the effects of surface reflections as well as noise introduced by bad pixels within the CCD array. Using a user specified subset of the images acquired in an experiment, an average image is generated. The background light and surface reflections are then removed from each image by subtracting the mean image. The final step is the application of a gain and offset to rescale the image intensities over the full 8-bit range.

Velocity vectors are then computed using cross-correlation computation. Extraneous vectors are eliminated by using the dynamic mean value operator technique outlined in Raffel et al. (1998).

Almost all of the experiments have several overlapping sets, or views, of images acquired for a single set of experimental parameters to maintain high spatial resolution over a large domain. The multiple views are merged into a single composite grid in order to facilitate post-processing of the velocity fields. The method of meshing is explained in depth in Honohan (2003). The time- and phase-averaged velocity components and Reynolds stresses are then computed for the composite grid.

The uncertainty of the velocity measurements is determined using the method of root sum square uncertainty, Δu_{RSS} :

$$\Delta u_{RSS} = \sqrt{\left[\left(\frac{\partial f}{\partial m_1}\Delta m_1\right)^2 + \left(\frac{\partial f}{\partial m_2}\Delta m_2\right)^2 + \ldots + \left(\frac{\partial f}{\partial m_N}\Delta m_N\right)^2\right]} \tag{2.3}$$

where f is the functional dependence of the measurements, and m_n are Δm_n the measurement quantity and corresponding uncertainty, respectively. The accepted measurement uncertainty for PIV measurements is ±0.5 pixels for the location of a particle. The optical zoom for the majority of PIV experiments was approximately 3 μm / pixel, which equates to an uncertainty in velocity of 6.3% at the maximum velocity.

2.4. Pressure Measurement

Time-averaged measurements of the streamwise, static pressure distribution along the channel were made using a 48 port Scanivalve connected to a Dwyer Microtector 1430

hook gauge to measure the differential pressure between the channel flow and atmosphere. The measurement resolution was 0.06 Pa. Using Equation 2.3, the uncertainty of these measurements is approximately ±4.2% at the maximum measured pressure. The pressure was allowed to equalize for approximately 60 seconds when switching between ports. The measurements were recorded manually. Typically five measurements were averaged to obtain the average pressure. The static ports are spaced as discussed in §2.2.

2.5. Channel Setup for Thermal Measurements

A channel integrated with a controlled heater was designed and constructed for measurements of the improvement in heat transfer induced by the reed. The local heat transfer coefficient is determined using Newton's law, $Q_{conv} = hA\left(T_s - T_\infty\right)$ where Q_{conv} is the convective heat loss, h is the local convection coefficient, T_s is the surface temperature and T_∞ is the local fluid temperature above the surface. In the present experiments an array of thermocouples is used to measure the local air and surface temperatures while keeping the surface at a constant heat flux using a thin foil heater on one wall made of 0.05 mm thick Inconel 600 (Figure 2.10).

Seventeen type-T thermocouples are mounted on the backside of the heater. Because the Biot number ($Bi = h\,s\,/\,k$) is << 0.01, the temperature gradient across the foil is negligible (Incropera and DeWitt, 1996). The foil was chemically etched using a Nitric acid solution to increase the microscopic surface roughness. The thermocouples were then fed through a template that held the beads close to the foil surface in a uniform alignment. The

thermocouples were spaced from upstream of the tip of the reed to the downstream end of the channel as outlined in Table 2.2. The thermocouples were carefully placed so that they touched the surface, then a small amount of adhesive was placed over each bead to temporarily attach it to the surface. The entire backside surface of the foil was then potted with a self-leveling RTV which provided support and a more permanent adhesion of the thermocouples to the foil, and helped to thermally insulate the backside of the foil

The foil is attached to two copper bus bars that provide electrical connection. These bus bars are placed along the long length of the channel, with the foil spanning across its width. This particular design was chosen because the variation in h across the width is expected to be low. Inconel has a relatively low coefficient of thermal expansion (13.3 μm / m °C), thus helping to maintain a flat surface when heated. Also, the temperature resistivity coefficient of Inconel 600 is low (1.48×10^{-8} °C^{-1} at 20 °C), ensuring that the resistance of the foil does not change appreciably with temperature. This minimal change reduces the difference in local resistance values, thus providing a constant heat flux surface. The Inconel foil, 0.05 mm thick, with a surface area of 44.5 mm × 82.5 mm, has a resistance of 0.011 Ω ($\rho_f = 1.03 \times 10^{-4}$ Ω m).

Table 2.2: Streamwise locations of thermocouples for measurement of localized surface temperatures

Thermocouple number	Distance from tip of PER (mm)	Thermocouple number	Distance from tip of PER (mm)
1	19	10	-9.6
2	15.9	11	-12.7
3	12.7	12	-19.1
4	9.5	13	-25.4
5	6.3	14	-31.8
6	3.1	15	-38.1
7	0	16	-44.5
8	-3.2	17	-50.8
9	-6.4		

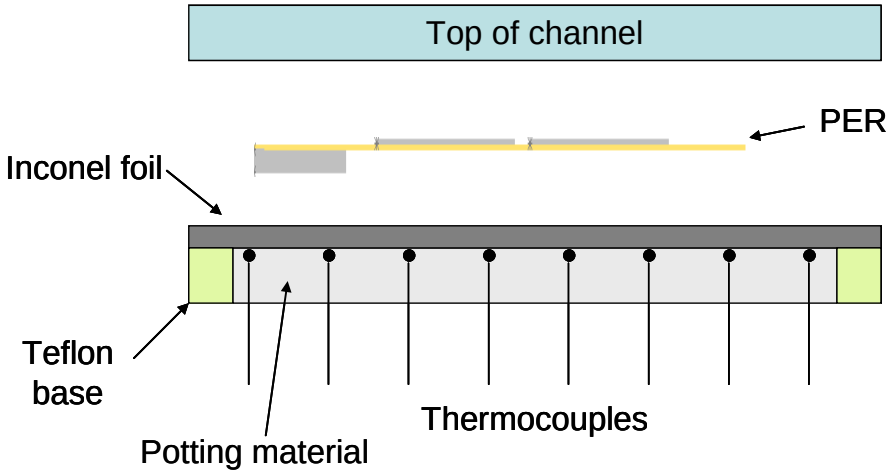

Figure 2.10: Basic heater schematic (not to scale)

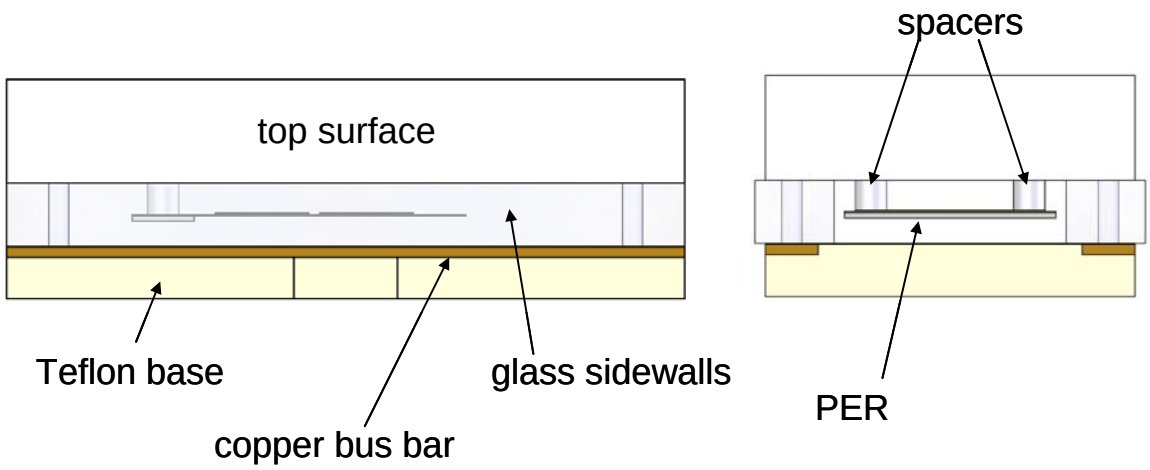

Figure 2.11: Side and end views of heater assembly

The foil and copper bus bars are built into a Teflon structure to provide a mold for the potting RTV and some insulation. The Teflon base has machined recesses to allow for mounting of the copper bus bars as shown in Figure 2.11. The bus bars are attached to the foil by a silver-filled epoxy to reduce contact resistance. The bus bar and the foil are then compressed between the Teflon base and the channel sidewalls. The channel is assembled using nylon screws to eliminate the possibility of a voltage short from the foil. The PER is attached to the upper channel surface in the same manner as in the flow experiments. The entire channel structure can be placed in either a vertical or horizontal orientation to test the effect of natural convection. The channel also has a removable SLA bellmouth attached to the entrance to reduce inlet head loss.

For calculating the local convection coefficient, conventional methods use the inlet air temperature for T_∞. For more accurate local measurements, the temperature immediately above the surface can be used. This local air temperature is measured using a single

thermocouple routed through a small diameter plastic hypodermic tube to help reduce flow disturbances. This thermocouple is lowered into the channel and moved to the various locations over the surface thermocouples. The global increase in heat transfer coefficient is determined by measuring the average air temperature entering and exiting the channel thus determining the amount of heat transferred to the air. This is done by measuring and averaging the temperatures across the channel height and width using the equation (assuming constant incompressible air, with constant properties):

$$Q_{conv} = c_p \rho_{air} \int_A U(x,y)\left(T_{ex}(x,y) - T_\infty\right) dA\,. \tag{2.4}$$

where c_p is the specific heat of the flow, ρ_{air} is the air density, $U(x, y)$ is the local air velocity, $T_{ex}(x, y)$ is the spatial average exit air temperature, and T_∞ is the average inlet air temperature.

Smyth and Salman (1991) studied the heat transfer in laminar channel flow through a channel that is heated in a very similar manner to that examined in this study. They created a constant heat flux foil heater similar to that discussed with the ability to heat the bottom and top wall independently, while the sidewalls were unheated. They calculated several different empirical formulas to relate *Nu* and *Re*. Garg et al. (2005) created a vertical, heated plate similarly, and used an infrared camera to measure the local temperatures.

The thermocouples are all connected to a Fluke Hydra data acquisition unit, and then read through a RS-232 connection. The Hydra has a resolution of 0.1°C, and an error of 0.7°C. T-type thermocouples have an accepted error of 0.5°C, for a total uncertainty of 1.2°C, or 3.75% at the highest measured temperatures. The total heater power is determined by measuring the current through the foil using a current sensor (Amploc AMP25) and multiplying by the resistance. The total uncertainty of the power measurements is approximately 0.8% of the maximum power measured. The total uncertainty in the thermal resistance (or convection coefficient or Nusselt number) is 3.84%.

Chapter 3

Investigation of the Reed Driven Flow

This chapter reports measurements of the flow field induced by the vibrating reed with the objective of identifying the mechanisms that enhance heat transfer within. The reed-induced flow is investigated in the presence and absence of bulk flow through the channel.

3.1. The Baseline Configuration – Flow Characteristics

The baseline channel configuration in the absence of bulk flow is discussed in §2.2. Figures 3.1a-i are raster plots of spanwise vorticity concentrations and distributions of velocity vectors within the channel. The flow is from left to right and each image includes the streamwise domain of $-0.6 \leq x / h_o \leq 2.25$ (i.e. $-0.6\ h_o$ upstream of the tip of the reed through the channel's downstream end). These data are measured phase-locked to the motion of the reed and are shown at nine increments ($\Delta t = 0.11\ T$ where T is the actuation period) during the cycle (18 total phases were investigated). The Strouhal number ($St = f_{res}\ A_{p\text{-}p} / U_{avg,\ exit}$) is based on the reed's resonance frequency, peak to peak displacement, and the average channel centerline velocity at the exit. In the present experiments, $St = 0.53$ ($f_{res} = 78$ Hz, $A_{p\text{-}p} = 6.3$ mm, $U_{avg,\ exit} = 0.92$ m / s). The onset of the actuation cycle is taken to be the upper most deflection (Figure 3.1a). As the reed moves downward though the first half of the cycle (Figures 3.1a-e), a clockwise (CW) vortex (centered at $x / h_o = 0.25$, $y / h_o = 0.10$) is visible just downstream of the tip. This vortex is formed during the upward motion in the previous cycle and migrates downstream and towards the upper wall as it weakens and becomes diffused (Figures

3.1b and c). The downward motion of the reed results in the formation of a counterclockwise (CCW) vortex near its tip (Figure 3.1b). The vortex is formed by vorticity flux from the bottom surface of the reed that wraps around the tip and accumulates near the top surface. Note also that the magnitude of the streamwise velocity below the reed increases as the reed approaches the bottom surface. At $x / h_o = 0$, $y / h_o = 0.1$, the phase-averaged maximum velocity ($U / U_{avg,\,O} = 2.79$) occurs at $t / T = 0.39$, as shown in Figure 3.2 ($U_{avg,\,O}$ is the average velocity at $x = 0$, $y = 0$, the origin). At $t / T = 0.39$, the reed is 78% through its downward sweep, but is not completely impeding the flow by blocking it. The phase-averaged data in Figure 3.1, shows that the vortices begin to lose their phase coherence for $x / h_o > 1$. The instantaneous realizations exhibit the presence of the vortices through $x / h_o < 2.5$.

It is noteworthy that the formation of the vortex leads to an induced velocity near the top surface of the reed and to the formation and ingestion of vorticity of the opposite sense. As the reed continues to move down (Figures 3.1d-f) the cross stream cross-section of the vortex increases until its induced flow scales with the channel height. It is remarkable that the vortex does not migrate downstream of the tip until the reed begins its upward motion (Figure 3.1f). At that point the similar formation of a CW vortex begins on the bottom surface of the reed (upstream of its tip) as the previous CCW vortex migrates towards the bottom surface and downstream while the flow accelerates between the reed and the top surface. Finally, the time-averaged flow is shown for reference in Figure 3.3. While this image clearly does not represent the instantaneous flow, it gives some measure of the average flow field that is induced through the channel by the thrust of the reed. Figure 3.4 shows the trajectories of the centers of the CW and CCW vortices through a

complete actuation cycle. This data shows that the vortex cores move slightly upstream before they are advected across the height of the channel and eventually downstream. It is remarkable that the centers of the CCW and CW vortices remain slightly below and above the centerline of the channel, respectively. Also, Figure 3.1 shows the downstream propagation speed, U_{prop}, of the vortices represented by a line through the vortex centers. The U_{prop} is only determined for $t / T > 0.5$ because prior to this the vortex has not begun to move away from the reed. The $U_{prop} \approx 1.3$ m / s.

Figure 3.1 indicates that there is a region of vorticity extending away from the channel walls into the core flow just downstream from the tip of the reed due to vertical transport of the fluid away from the walls. Figures 3.1a and f show this vorticity extends approximately 0.25 h_o away from the walls at $x / h_o = 1$. These regions move downstream with the CW and CCW vortices. This vorticity suggests boundary layer disruption and may provide the highest localized heat transfer coefficient.

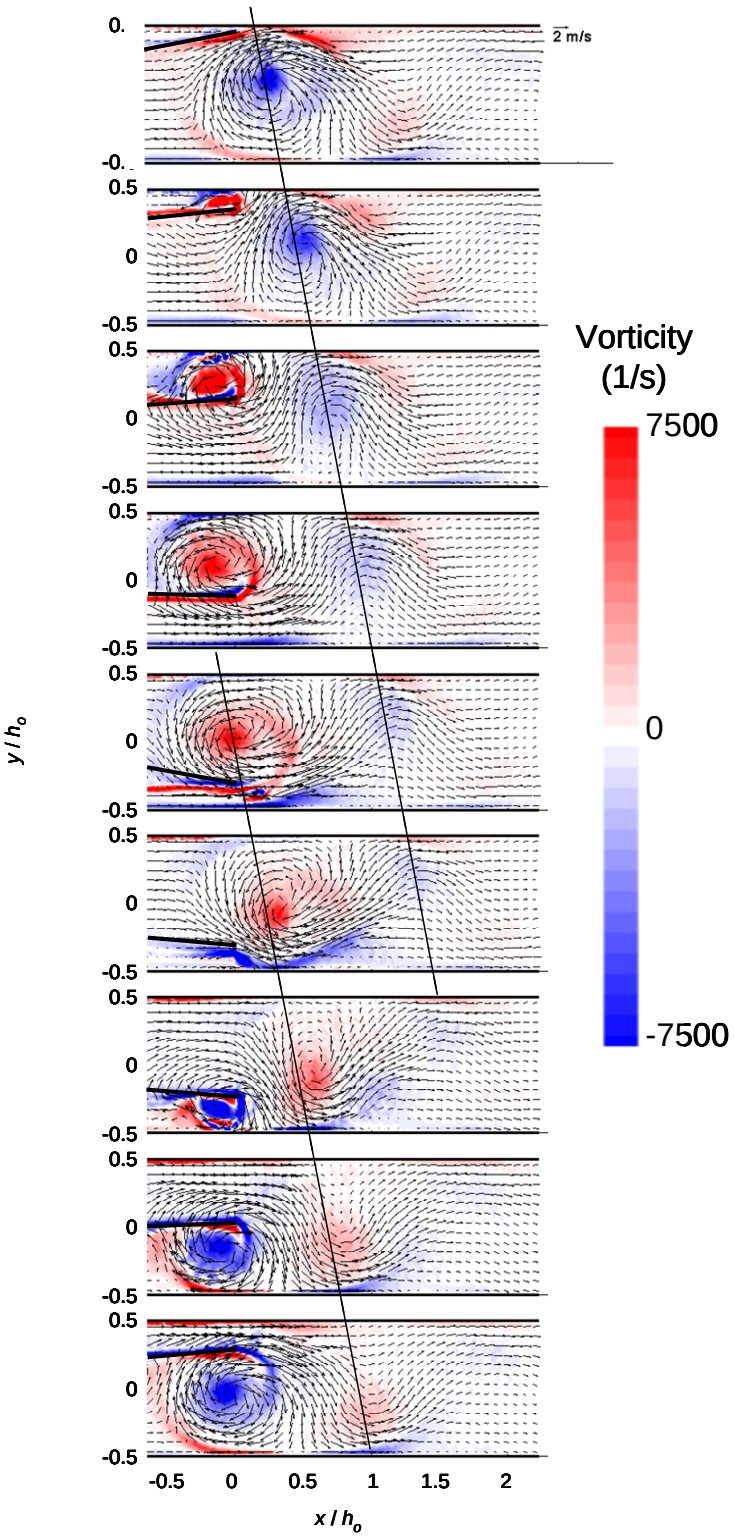

Figure 3.1: Distributions of phase-averaged vorticity and velocity within the channel during the reed actuation cycle with vortex propagation speed shown, t / T = 0 (a), 0.11 (b), 0.22 (c), 0.33 (d), 0.44 (e), 0.55 (f), 0.66 (g), 0.77 (h), and 0.88 (i). (St = 0.53, f_{res} = 78 Hz, $A_{p\text{-}p}$ = 6.3 mm, $U_{avg,exit}$ = 0.92 m / s)

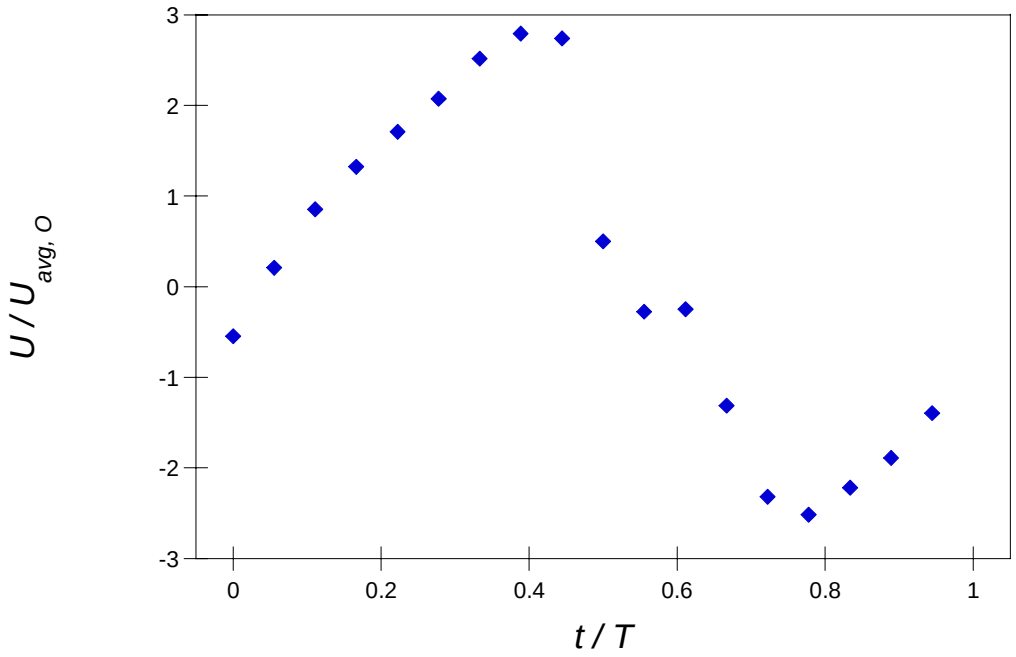

Figure 3.2: Streamwise velocity at $x / h_o = 0$, $y / h_o = 0.1$ for complete cycle ($U_{avg,\,O} = 1.75$ m / s)

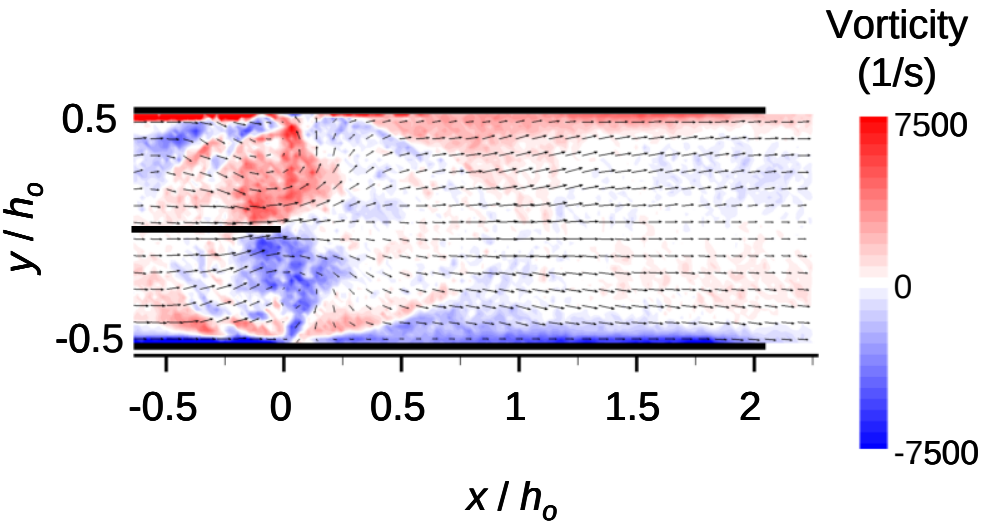

Figure 3.3: Time-averaged vorticity and velocity within the channel ($St = 0.53$, $f_{res} = 78$ Hz, $A_{p\text{-}p} = 6.3$ mm, $U_{avg,exit} = 0.92$ m / s)

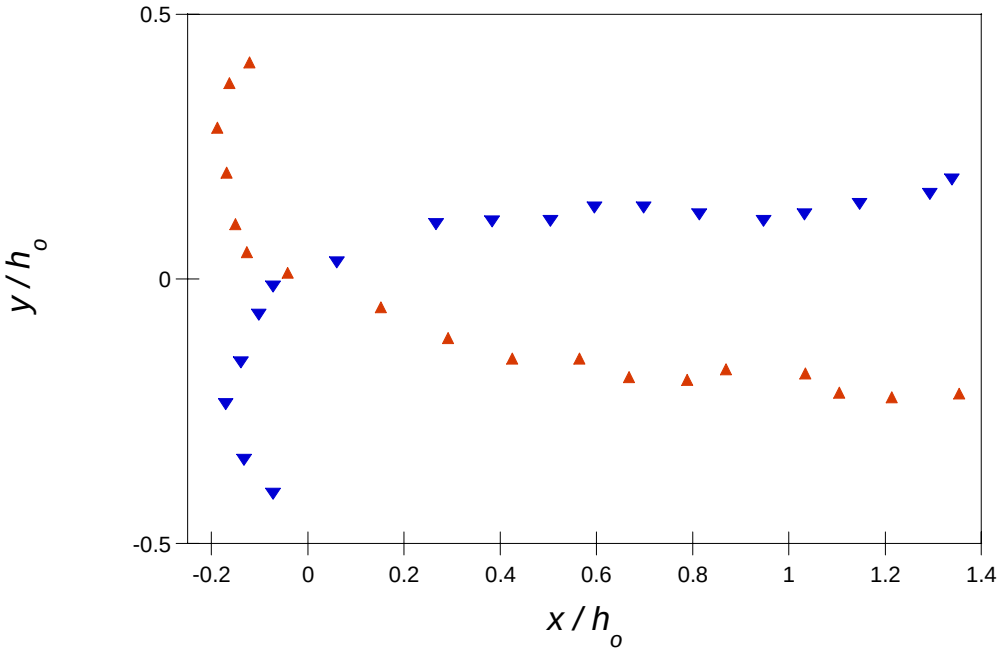

Figure 3.4: Trajectories of the vortex for one cycle; CW (▼) and CCW (▲) vortices

Cross steam distributions of the time-averaged, streamwise velocity at various streamwise stations are shown in Figure 3.5 where it is normalized by the peak (centerline) air velocity at the origin ($U_{max,\,O} = 1.75$ m / s). The maximum time-averaged velocity in the channel ($1.17\ U_{max,\,O}$) is measured at the center of the channel at $x / h_o = -0.125$. The reverse flow near the walls is caused by the vortex rotation and may increase the local heat transfer coefficient in this region. At $0.125 \le x / h_o \le 0.75$, the maximum velocity occurs near the walls (represented by the double peaks in velocity), corresponding to the migration of the counter-rotating vortices. The inflection point of the maxima and minima velocities near the wall correspond to the vortex centers as shown in Figure 3.4. Farther downstream, $x > 0.75$, the velocity dissipates more uniformly across the cross-span, resulting in the typical developed profile near the exit. The slight asymmetry in the

velocity distributions is the result of the slight displacement of the tip (at rest) relative to the centerline as discussed in §2.1.

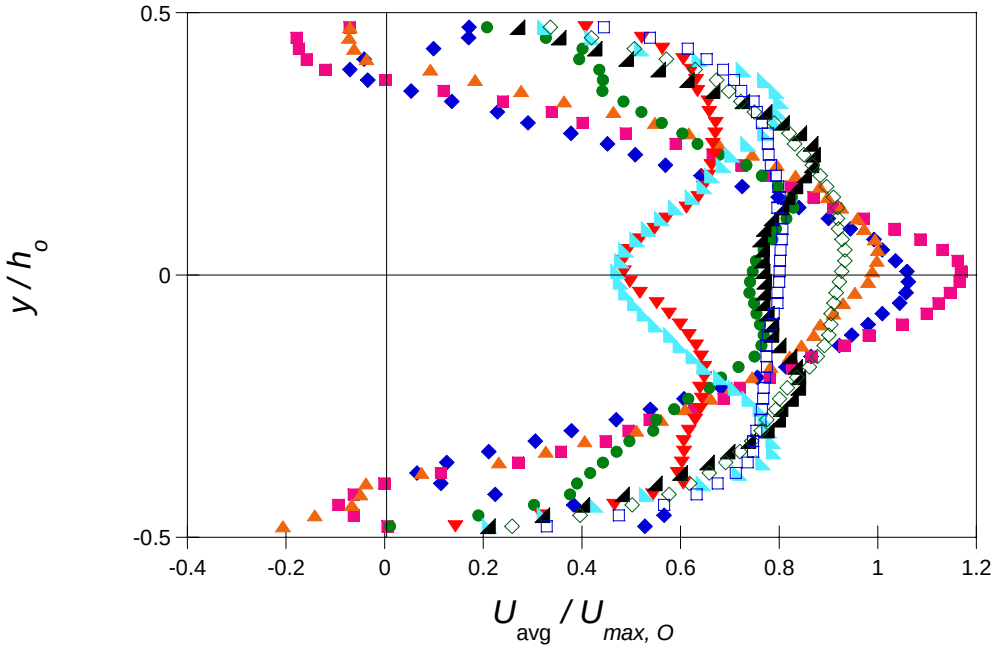

Figure 3.5: Normalized time-averaged streamwise velocity distribution at x / h_o = -0.25 (◆), -0.125 (■), 0 (▲), 0.125 (●), 0.25 (▼), 0.5 (◣), 0.75 (◢), 1.0 (◇), 1.25 (□) ($U_{max,\,O}$ = 1.75 m / s)

The coefficient of thrust produced by the vibrating reed can be calculated from the velocity profiles above, along with knowledge of the incoming velocity distribution and the pressure gain across the length of the reed, as discussed later. Assuming a control volume surrounding the reed, bounded by the channel walls, the thrust per unit width is calculated from:

$$T' = \int_0^{h_o} U_2^2 \rho dy - \int_0^{h_o} U_1^2 \rho dy + (P_2 - P_1)h + \int_0^{L_r} \tau_{x_{1,2}} dx \qquad (3.1)$$

where U_1 and P_1 are the inlet velocity and pressure, U_2 and P_2 are the exit velocity and pressure, ρ is the density of air, $\tau_{x_{1,2}}$ is the shear stress at the wall, and L_r is the length of the reed. The calculated T' is 0.025 N / m, and the corresponding coefficient of thrust, $C_T = 0.525$. This corresponds well with the published values of $C_T \approx 0.45$ for an airfoil at $St = 0.45$ by Anderson et al. (1998).

The time-averaged velocity distribution for the vibrating reed in free air is shown in Figure 3.6. Because no walls bound the flow, the velocity distribution spreads radially outward. The maximum induced velocity at the tip of the reed is approximately equal that obtained with the channel flow (1.56 m / s). The vortices move away from the reed at an angle of approximately ±45°. The maximum vorticity intensity is approximately one third than that in the channel configuration. The thrust produced by the reed in the channel is nearly 2.5 times that produced by the reed in free air. The increase in thrust is the result of the jet ejector effect.

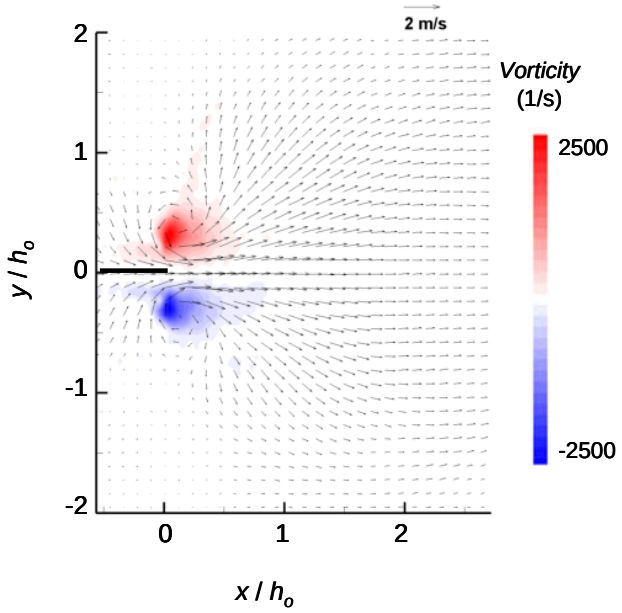

Figure 3.6: Time-averaged velocity and vorticity distribution of vibrating reed in free air ($A_{p\text{-}p} = 0.47\ h_o$)

Figure 3.7 is a raster plot of the y-component vorticity and velocity distributions across the span of the channel at $y / h_o = 0$. The channel width, w, is 1.1 w_r, normalized by the width of the reed, $w_r = 25.4$ mm. The vorticity is bounded between $w = \pm 0.35\ w_r$ and extends from the tip of the reed to the exit, suggesting bending of the spanwise vortices seen earlier. The CW vorticity for $w < 0$ and CCW vorticity for $w > 0$ induce a jetting effect along the centerline resulting in the highest streamwise velocity across the span. The velocity slowly spreads towards the sidewalls, as the peak velocity begins to decrease. Near the tip, there is little velocity near the walls. The normalized time-averaged streamwise velocity across the span at the channel's exit is shown in Figure 3.8 for $w / w_r = 1.1$, 1.16, and 1.23 ($U_{o,\,max} = 0.90$ m / s, the maximum, average velocity). When the channel's width is increased the maximum velocity at the centerline is increased slightly, but the reverse flow near the channel walls increases as well, resulting

in that the total volume flow rate is invariant. The reverse flow is undesired because this indicates hot air is being recirculated and the heat transfer near the exit of the channel will be reduced, therefore, it is preferable to minimize w / w_r. The effect of the channel width will be investigated more thoroughly in §3.5.

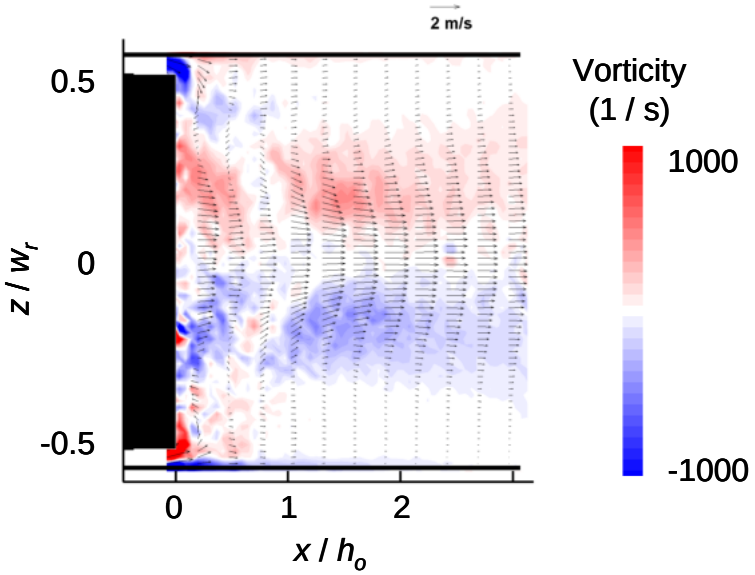

Figure 3.7: Distributions of time-averaged *y*-component of vorticity and velocity across span ($y / h_o = 0$)

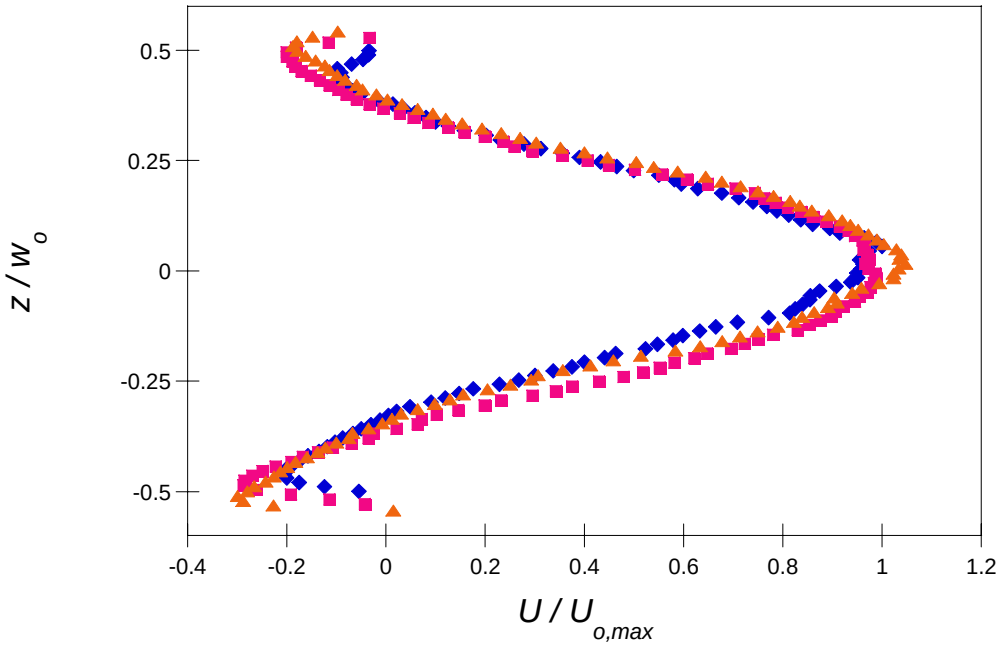

Figure 3.8: Time-averaged streamwise velocity distribution of air exiting channel across span for w / w_r = 1.1 (◆), 1.16 (■), and 1.23 (▲) ($U_{o,\,max}$ = 0.90 m/s)

The peak to peak amplitude ($A_{p\text{-}p}$) of the reed displacement has a profound effect on the evolution of the flow. Figure 3.9 shows time-averaged cross stream distributions of the streamwise velocity at $x = 0$ at the channel's midspan for several $A_{p\text{-}p}$. Similar to Figure 3.5, for all $A_{p\text{-}p}$ the maximum velocity occurs at the center of the channel and there is a region of reverse flow near the walls. As $A_{p\text{-}p}$ is decreased from $A_{p\text{-}p} / h_o = 0.54$ to 0.10, the reverse flow penetrates farther into the center of the channel ($U < 0$ at $y / h_o > \pm 0.38$ and ± 0.14 respectively). Also, the maximum velocity increases with $A_{p\text{-}p}$ until $A_{p\text{-}p} / h_o = 0.45$, and then decreases slightly. It is possible that when the tip of the reed is too close to the wall, the vortex formation becomes hindered. However, as shown in Figure 3.10, the volume flow rate increases monotonically with increasing $A_{p\text{-}p}$ and eventually saturates. In the present configuration, the maximum volume flow rate

induced by the reed is approximately 0.53 CFM. Once again, the asymmetry in the velocity profiles exists due to vertical asymmetry in the bending of the reed.

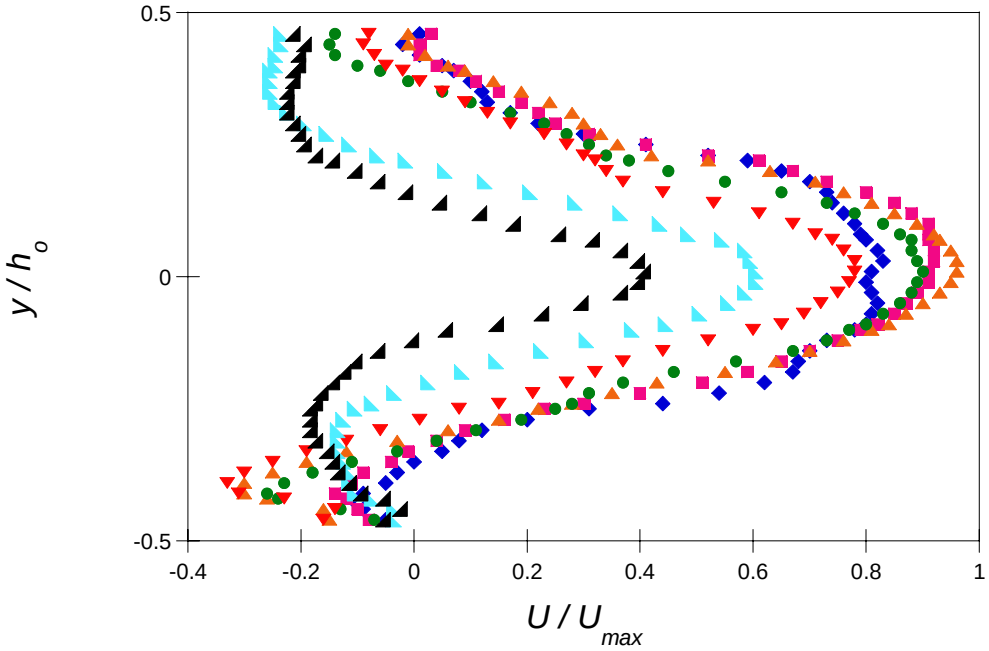

Figure 3.9: Streamwise velocity at $x / h_o = 0$ for $A_{p\text{-}p} / h_o = 0.54$ (◆), 0.49 (■), 0.42 (▲), 0.33 (●), 0.24 (▼), 0.17 (◣), and 0.10 (◢) ($U_{max} = 2.45$ m / s)

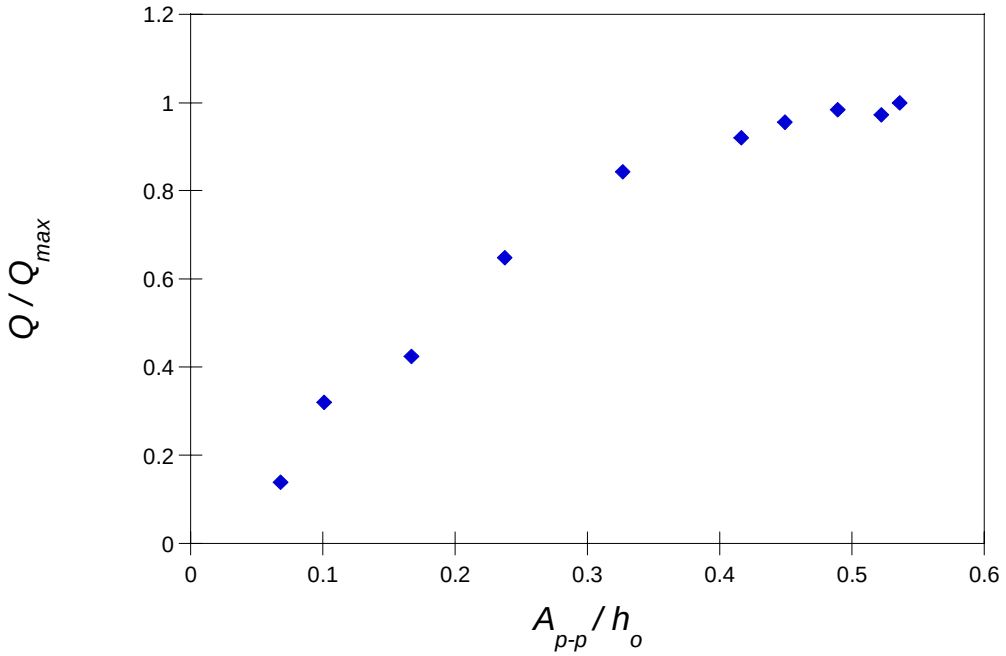

Figure 3.10: Variation of volume flow rate with $A_{p\text{-}p} / h_o$ (Q_{max} = 2.97 × 10^{-4} m^3 / s, 0.53 CFM)

The variation of the channel exit volume flow rate over the reed cycle is shown in Figure 3.11. These data show that the magnitude of flow rate is nearly invariant with phase, although there is a time-periodic variation, with the maxima occurring when the reed is nearly horizontal, i.e. t / T = 0.28 and 0.72, whereas the minima occur when the reed is at its upper or lower apex.

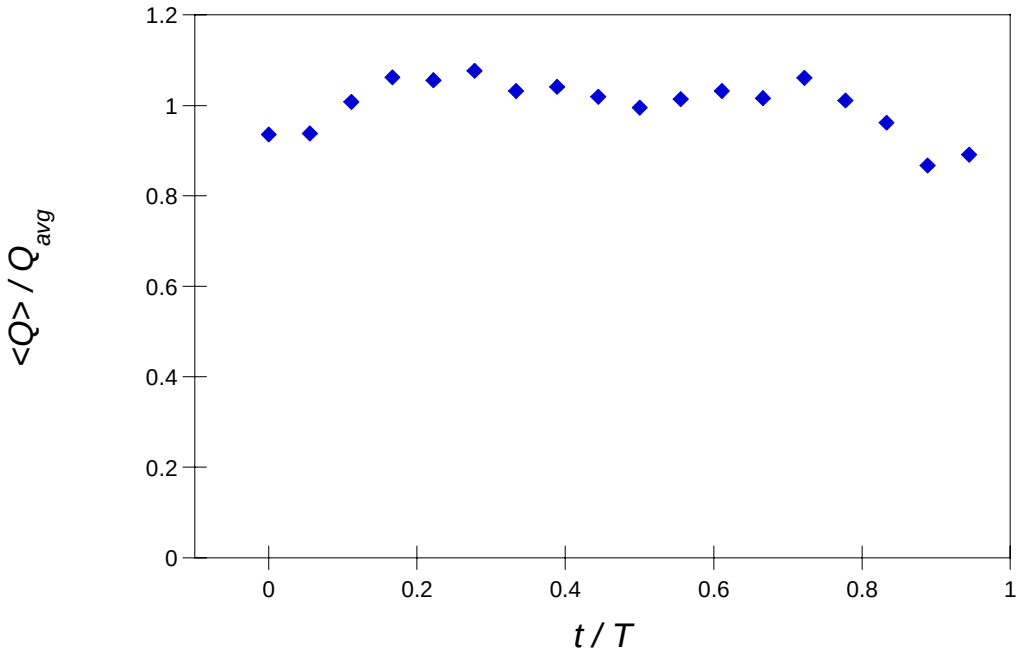

Figure 3.11: Phase-averaged volume flow rate for one cycle at channel exit, $Q_{avg} = 2.03 \times 10^{-4}$ m^3 /s (0.43 CFM)

As shown in the present work, the reed-induced flow results in a substantial increase in heat transfer achieved compared to steady channel flow. This is the resultant of flow instability created by the vibrating reed. Although the Reynolds number of the reed-induced flow is relatively low (e.g. $Re \approx 600$) there are strong concentrations of small-scale motions as is evidenced by the phase-averaged Reynolds stresses, $u'u'$ and $v'v'$, shown in Figures 3.11, and 3.12a-i respectively. All three Reynolds stresses indicate that there is small scale mixing throughout the entire channel length with the maximum occurring concomitantly with the movement of the vortex center. Figure 3.12a indicates that the maximum $u'u'$ is centered at $x / h_o = 0.25$, $y / h_o = 0.10$, the same location as the CW vortex shown in Figure 3.1a. Figure 3.13a similarly indicates that the maximum $v'v'$ is centered at $x / h_o = 0.25$, $y / h_o = 0.10$. It is noteworthy that there is a region of high Reynolds stress extending from the walls, just downstream from the tip of the reed,

similar to that found in the vorticity plots. Figures 3.12b and g indicate that this region stretches from $x / h_o = 0.6 - 1.25$, and extends from the top and bottom channel walls, respectively, to $y = 0$. This indicates that there is boundary layer disruption in this location, and may provide the highest localized heat transfer. The phase-averaged fluctuation kinetic energy (KE_f) distribution is shown in Figures 3.13a-i. The KE_f is an indicator of the mixing of the fluid, it is a strong indicator of the expected increase in localized heat transfer. Because $KE_f = 0.5\ (u'u' + v'v')$, the relation between it and the vorticity is identical to that already discussed for $u'u'$ and $v'v'$.

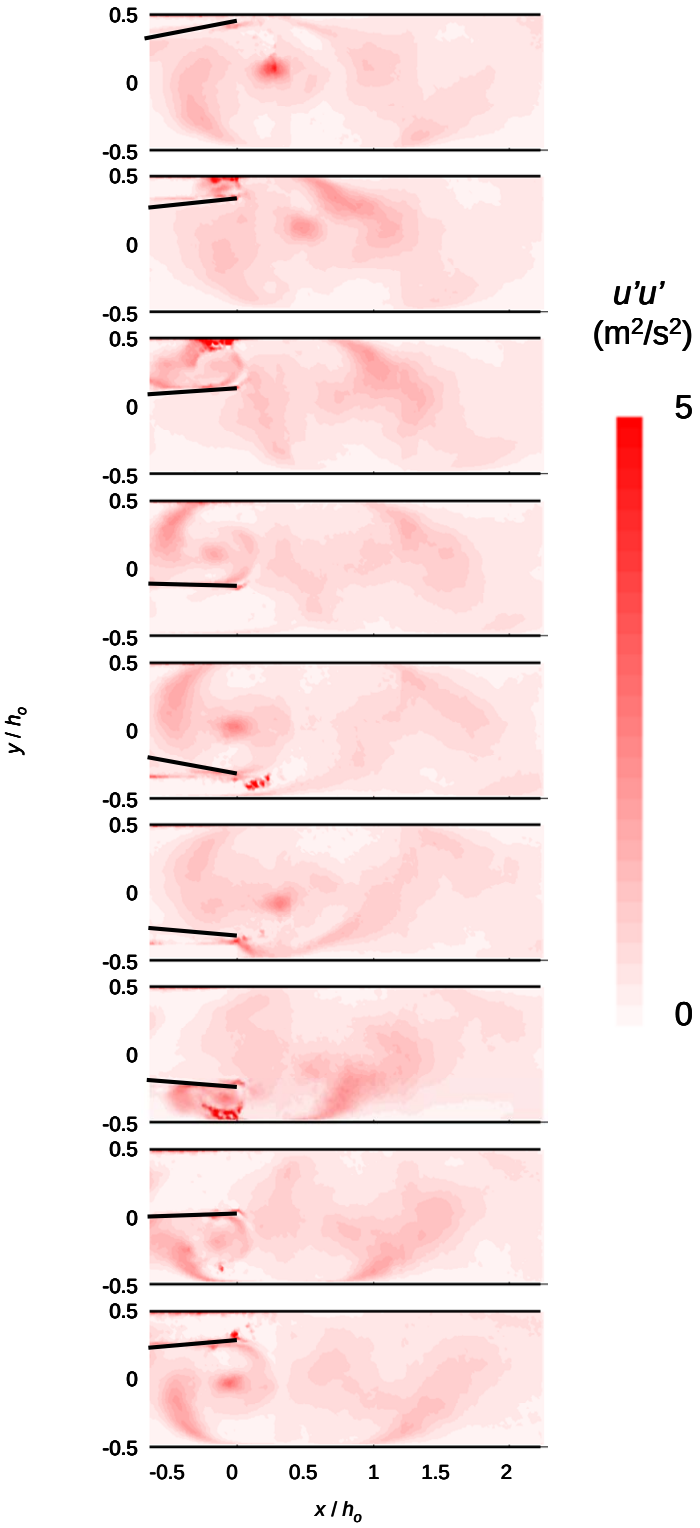

Figure 3.12: Phase-locked *u'u'* Reynolds stress distribution for one cycle of PER, *t / T* = 0 (a), 0.11 (b), 0.22 (c), 0.33 (d), 0.44 (e), 0.55 (f), 0.66 (g), 0.77 (h), and 0.88 (i) (*St* = 0.53)

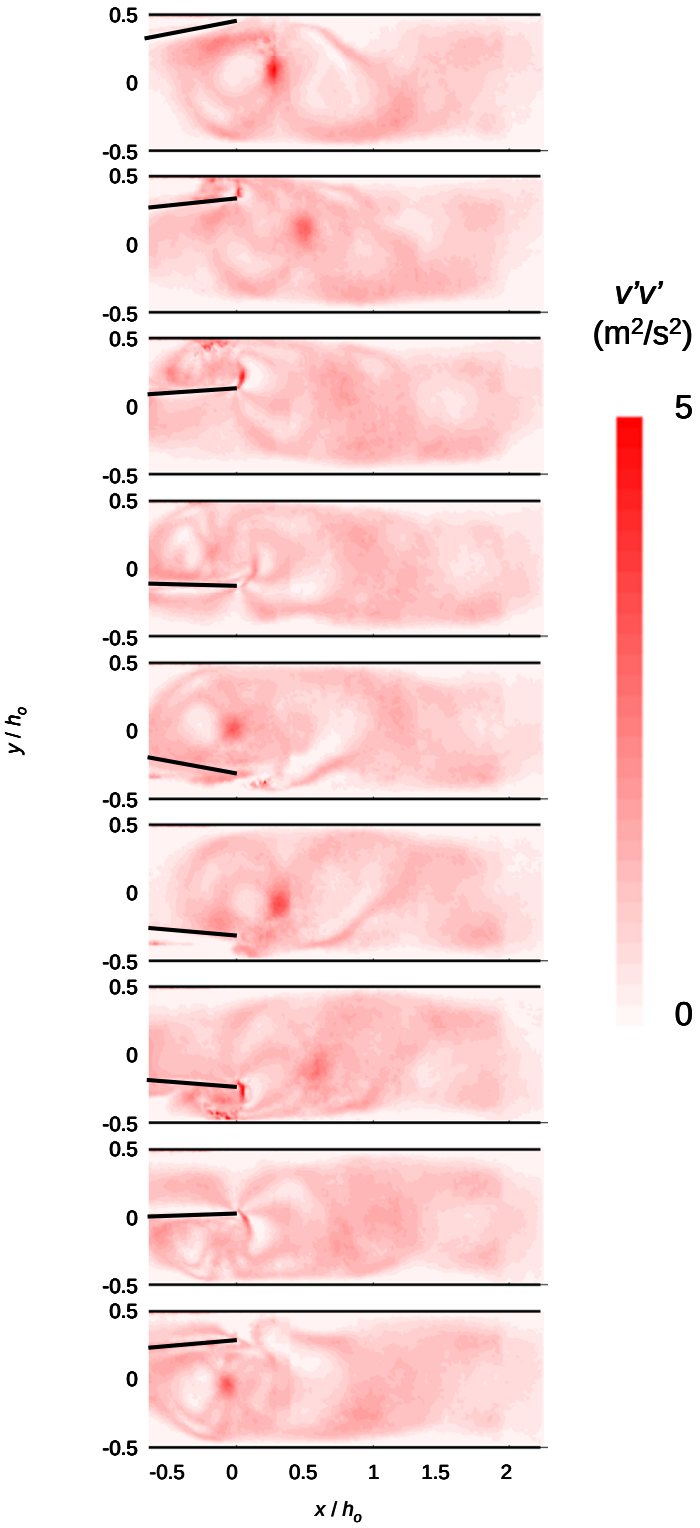

Figure 3.13: Phase-locked *v'v'* Reynolds stress distribution for one cycle of PER, *t / T* = 0 (a), 0.11 (b), 0.22 (c), 0.33 (d), 0.44 (e), 0.55 (f), 0.66 (g), 0.77 (h), and 0.88 (i) (*St* = 0.53)

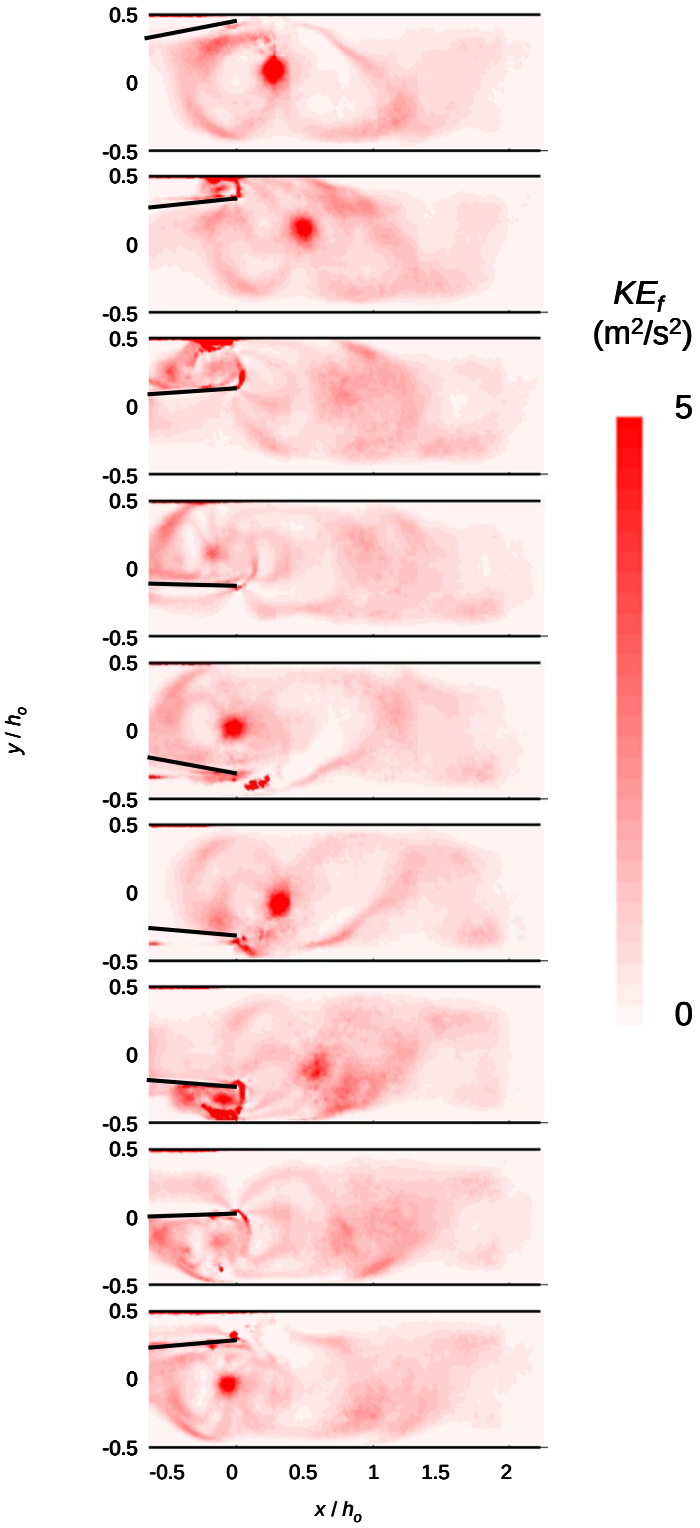

Figure 3.14: Phase-locked turbulent kinetic energy for one cycle of PER, $t/T = 0$ (a), 0.11 (b), 0.22 (c), 0.33 (d), 0.44 (e), 0.55 (f), 0.66 (g), 0.77 (h), 0.88 (i); Time-averaged (j) ($St = 0.53$)

The time-averaged Reynolds stresses are shown in Figures 3.14a-c. For the time-averaged $u'u'$, Figure 3.14a, the maximum value occurs above and below the tip of the reed near the channel walls. This is due to the maximum variation in U occurring at the top and bottom of the vortices as they are formed on the reed. The maximum time-averaged $v'v'$, Figure 3.14b, occurs just downstream from the tip at the center of the channel. The $v'v'$ present upstream of the tip is artificially enhanced by the motion of the reed, and therefore should be discounted. The $v'v'$ region stretches vertically across the height of the channel because the maximum variation in V is vertically across the vortices. Also, this is a factor of the vortices moving vertically across the channel height at this location. The time-averaged $u'v'$, Figure 3.14c, is nearly symmetric with positive $u'v'$ for $(x < 0, y > 0)$ and $(x > 0, y < 0)$, and negative $u'v'$ for $(x < 0, y < 0)$ and $(x > 0, y > 0)$. The intensity of the time-averaged stresses is much higher than that of the phase-averaged due to the cyclic nature of the flow. The maximum time-averaged intensity level for $u'u'$ is greater than for $v'v'$, indicating that the flow field has greater variation in the streamwise direction. The intensity of the shear stress ($u'v'$) is much less than either of the normal stresses. The time-averaged distribution of KE_f (Figure 3.15d) indicates the maximum KE_f occurs in a nearly heart shaped region surrounding the tip and propagating downstream. This indicates that the maximum small scale mixing occurs near the tip and across the entire height of the channel.

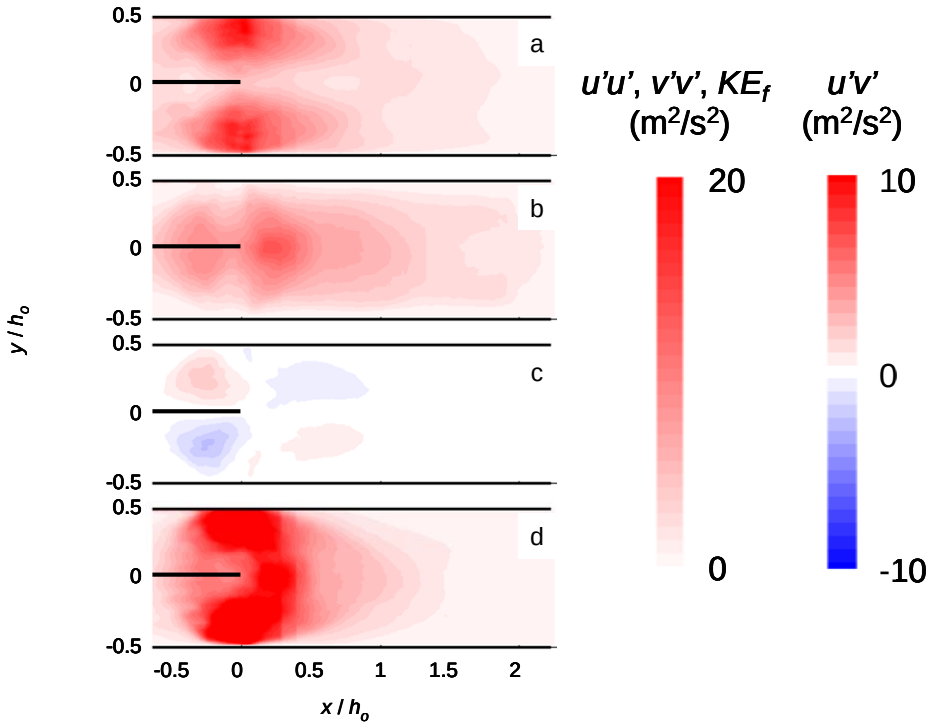

Figure 3.15: Time-averaged distribution of Reynolds stresses (a) *u'u'*, (b) *v'v'*, (c) *u'v'* and (d) fluctuation kinetic energy

3.2. The Baseline Configuration – Streamwise Pressure Distributions

The pressure along the length of the channel is measured using an array of static pressure ports as discussed in §2.4. Figure 3.16 shows the coefficient of pressure, $C_p = \frac{P - P_{atm}}{0.5\rho_{air}U_{avg}^2}$, for $A_{p\text{-}p} / h_o = 0.6$ and 0.9. The measurement domain extends from $x / h_o = -5.33$ (upstream of the reed) to the channel exit. The most salient feature of the pressure distribution is the pressure rise between $C_p = -15.1$ at $x / h_o = 0$ and $C_p = 6.1$ at $x / h_o = 0.33$, for $A_{p\text{-}p} / h_o = 0.9$. The pressure decrease upstream of the tip of the reed (relative to the ambient pressure) provides suction and the pressure decrease downstream of the reed tip provides blowing (both with favorable pressure gradient). It is noteworthy that while the pressure minimum occurs near the tip of the reed, the pressure maximum

occurs farther downstream and may be associated with blockage as a result of the formation of the counter-rotating vortices. As $A_{p\text{-}p}$ is increased, C_p decreases due to the drop in velocity.

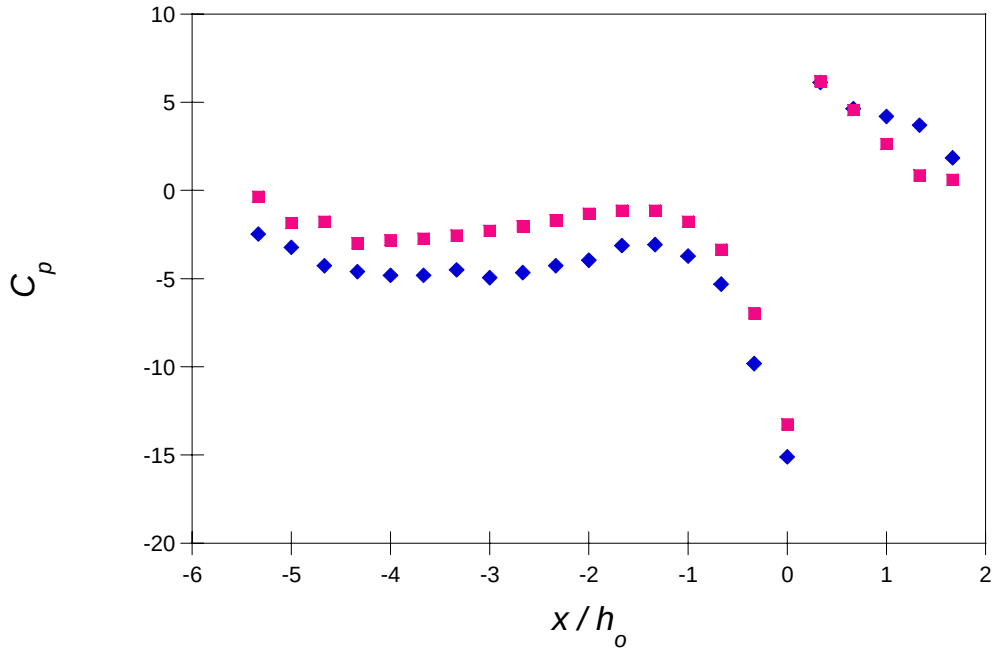

Figure 3.16: Streamwise variation of the static pressure along channel for $A_{p\text{-}p} / h_o$ = 0.9 (◆), 0.6 (■)

The effect of the losses associated with the duct length on the pressure rise and volume flow rate induced by the reed are investigated by extending the duct length upstream and downstream of the reed section. As shown schematically in Figure 3.17, the length of the channel can be increased by adding extensions on either the upstream or downstream ends of the original channel. Figure 3.18 shows the streamwise static pressure C_p for various downstream channel extensions extending from x / h_o = -4.4 to 80. The reed adds available head to the flow resulting in $C_p > 0$, but then as x increases, the pressure decreases linearly until reaching zero at the channel exit, as expected. Figure 3.19 shows

the localized streamwise static pressure C_p for various channel extensions ($\pm L_a$) extending from x / h_o = -4.4 to 0.6. The pressure profile does not change shape compared to the $L_a = 0$ channel for any extension length, upstream or downstream. For positive L_a, the pressure at $x / h_o = 0$ decreases with increasing length. This trend also appears upstream of the tip, $x / h_o < -2$, but the values all collapse closer to the tip, $-2 < x / h_o < -0.5$. The values of C_p for $L_a = -20\ h_o$ is nearly equal to $L_a = +20\ h_o$, but $L_a = -80\ h_o$ does not closely resemble its positive counterpart. This suggests that the induced flow is affected differently in suction vs. blowing. This is reinforced by investigating the head rise, ΔH_r, across the tip of the reed for various extension lengths, as shown in Figure 3.20, normalized by ΔH_{ro}, the head rise of the standard channel. The head rise is calculated by the difference in the pressure across the reed tip ($\Delta H_r = P\big|_{x/h_o=0.25} - P\big|_{x/h_o=0}$). This figure shows asymmetry in ΔH_r between positive and negative L_a. Compared to $L_a = 0$, ΔH_r decreases linearly with upstream extensions ($\Delta H_r / \Delta H_{ro} = 0.85$ for $L_a = -80\ h_o$), but ΔH_r increases by 15% for $L_a = 20\ h_o$. For $L_a > 20\ h_o$, the pressure then decreases with increasing length. This indicates that the reed operates differently in suction than in blowing.

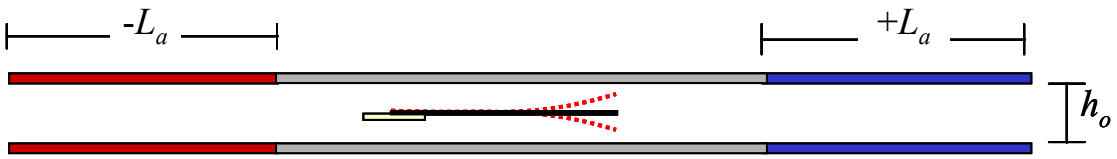

Figure 3.17: Increased channel length

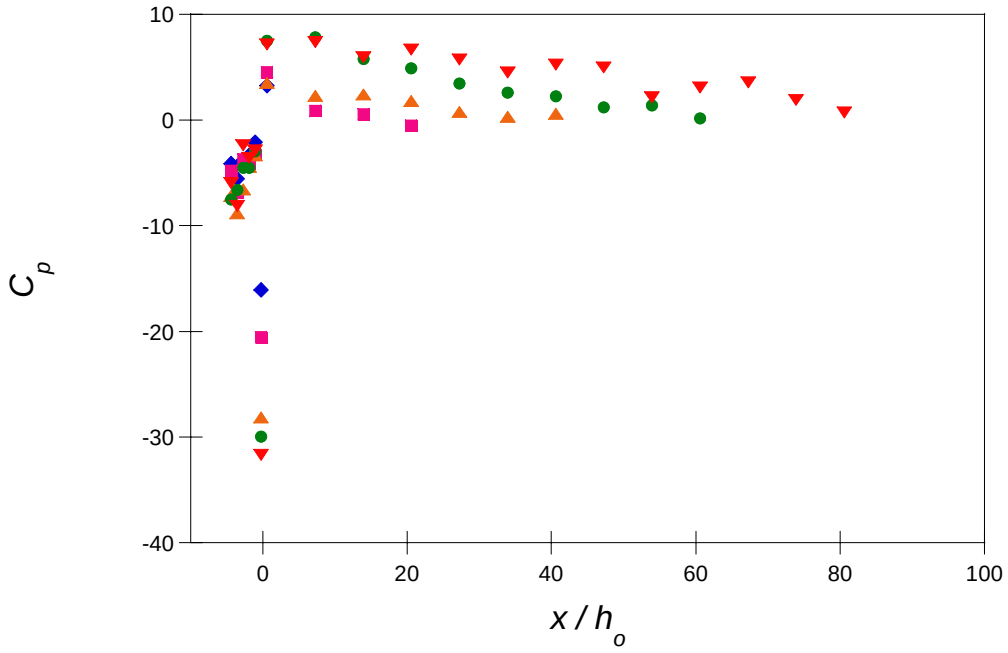

Figure 3.18: Global streamwise static pressure distribution for L_a = 0 (◆), 20 h_o (■), 40 h_o (▲), 60 h_o (●), and 80 h_o (▼)

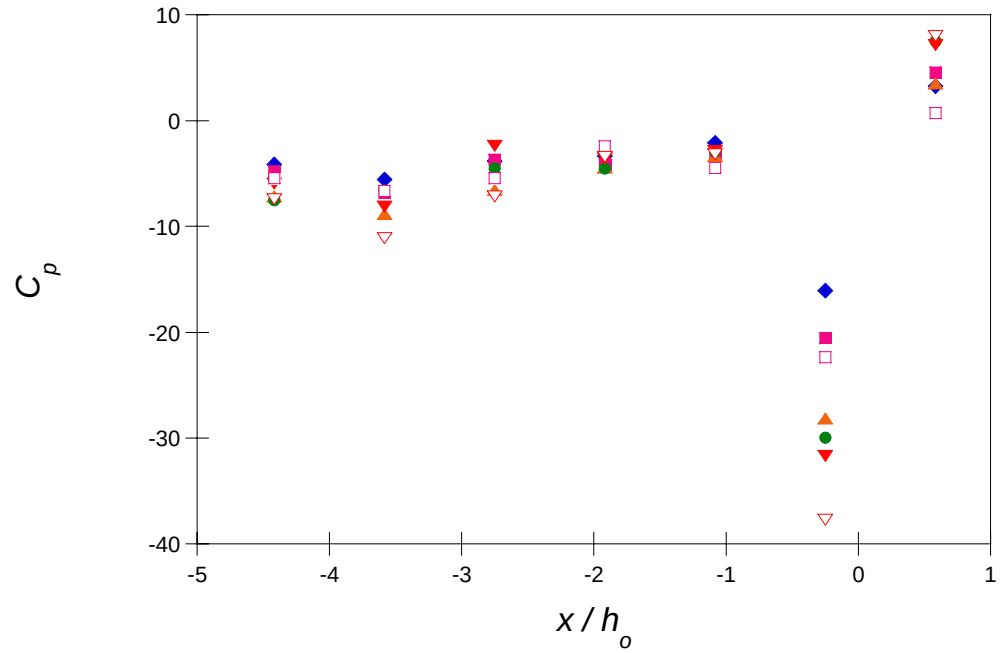

Figure 3.19: Local streamwise static pressure distribution for L_a = 0 (◆), 20 h_o (■), 40 h_o (▲), 60 h_o (●), 80 h_o (▼), -20 h_o (□), and -80 h_o (▽)

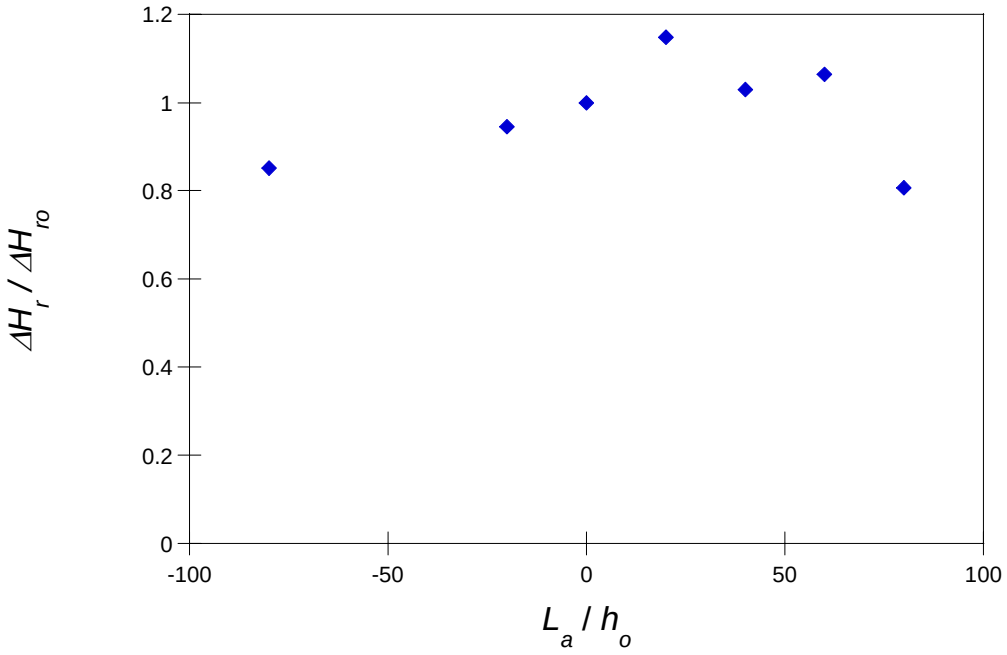

Figure 3.20: Head rise ratio for increased channel length (ΔH_{ro} = 2.51 Pa)

The decrease in ΔH_r indicates extra head losses due to the extended channel that will result in decreased volume flow rate. The volume flow rate through the channel for the various extensions is shown in Figure 3.21, and normalized by the flow rate of the standard channel, Q_o = 0.22 CFM. For constant $A_{p\text{-}p}$, Q decreases with increasing channel length regardless of upstream or downstream loading.

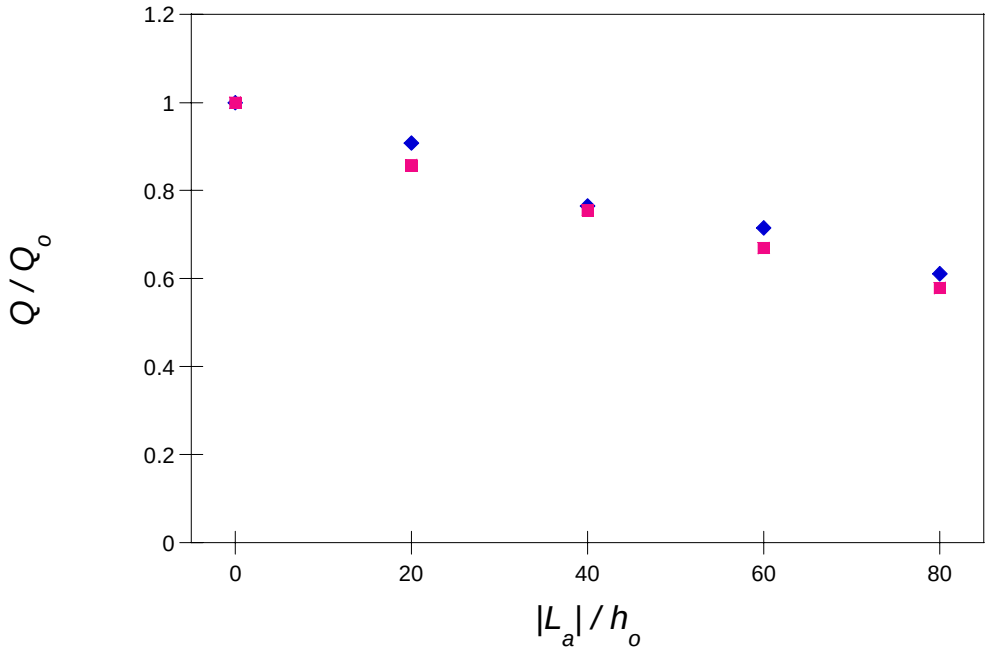

Figure 3.21: Volume flow rate for additional lengths added; $+L_a$ (◆) and $-L_a$ (■), (Q_o = 0.21 CFM)

3.3. Interactions of Reeds in Tandem

The present investigation also considers the effectiveness of reeds that are configured in tandem. To this end, the channel length is increased to accommodate two reeds and they are both operated at the same frequency and amplitude. From a global standpoint, it is expected that the operation of two reeds in tandem increases the available head at a given flow rate, or alternately increases the flow rate at a given head. As discussed in §1.1, Gopalkrishnan et al. (1994) determined that it is possible to increase the strength of a vortex being formed on a pitching airfoil by merging it with a preexisting vortex in the core flow. The criteria for merging the two vortices are determined by the coupling of the spacing between the two airfoils and the phase difference between their pitching.

The series channel configuration is shown schematically in Figure 3.22. The channel height is unchanged from previous experiments (h_o = 7.62 mm) and the upstream reed is placed at the same downstream distance from the channel inlet (2.7 h_o). The spacing between the two reeds, x_s, is varied to investigate its effect on vortex interactions with the downstream reed. Figure 3.23 shows the effect of the separation distance on the normalized average centerline exit velocity when the reeds are operated in-phase. The separation distance is normalized by the shedding wavelength, $x_w = U_{avg} / f_d$ = 10.6 mm. These data show that the velocity increases by less than 10% indicating that the x_w does not significantly affect the flow. It is conjectured that the relatively long reed length (3.8 x_w) reduces the effect of the upstream vortices.

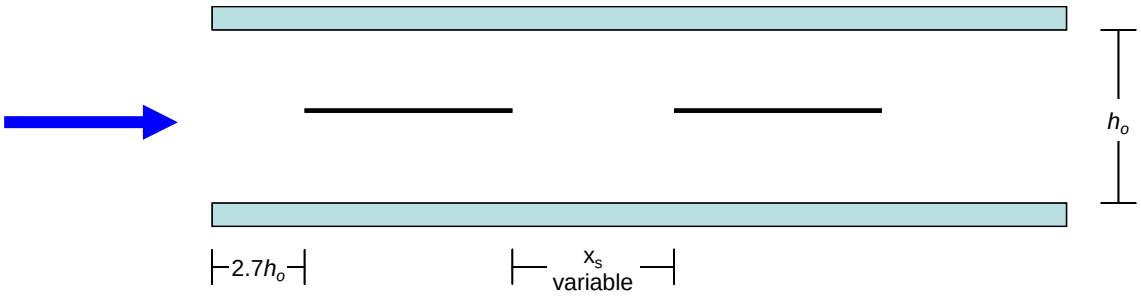

Figure 3.22: Schematic configuration of tandem reeds

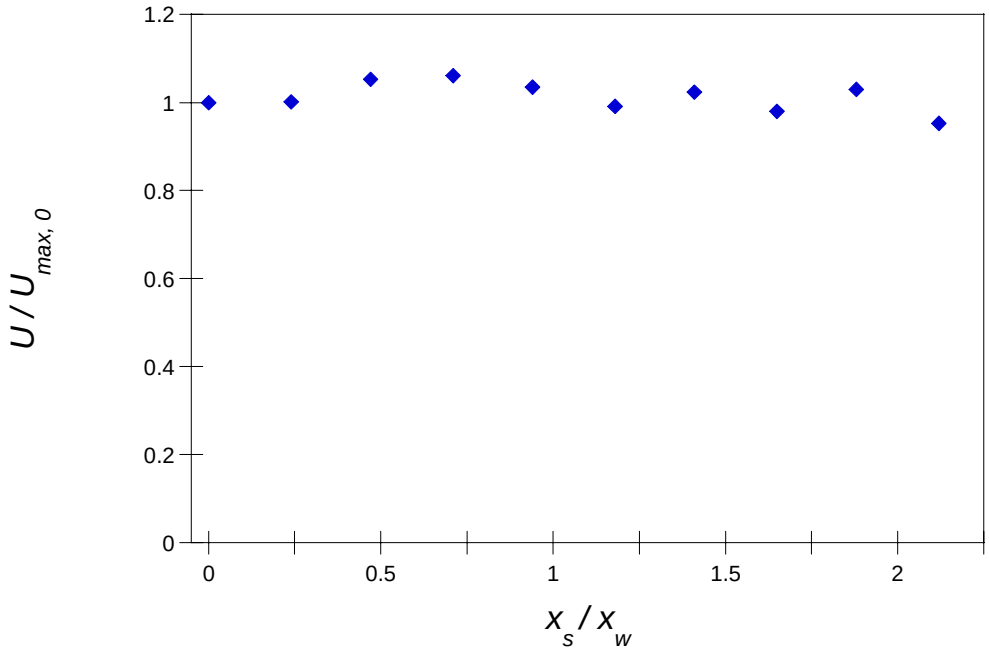

Figure 3.23: Variation of time-averaged channel exit velocity of tandem reeds ($\Delta\Phi = 0$, $U_{max,\,0} = 1.39$ m / s for $x_s = 0$)

Figure 3.24 shows the cross stream distributions of the streamwise velocity at the channel's exit plane for several phase differences between the reeds with $x_s = 2.25\, x_w$. These data show that $\Delta\Phi$ has little effect on either the exit velocity magnitude or distribution for this spacing.

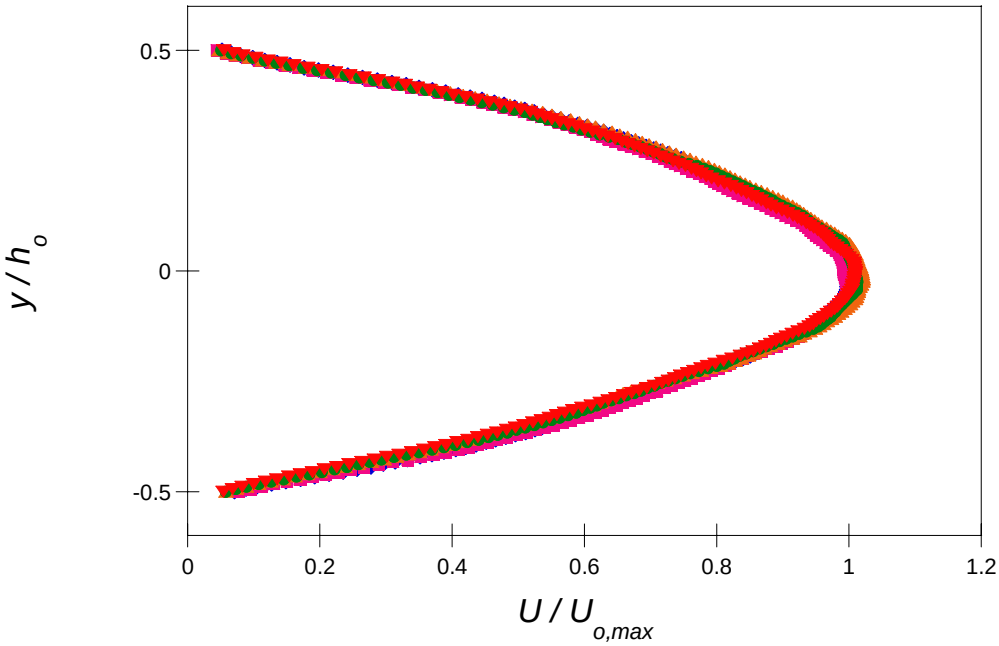

Figure 3.24: Streamwise velocity at channel's exit plane for $\Delta\Phi$ = 0° (◆), 80° (■), 160° (▲), 240° (●), and 320° (▼) (x_s = 3.33 h_o, $U_{o,\,max}$ = 1.39 m / s, $A_{p\text{-}p}$ / h_o = 0.6)

The effect of two reeds in tandem on the cross stream distributions of streamwise velocity at the channel exit for $x_s = 2.25\, x_w$ is shown in Figure 3.25. These data correspond to activation of the upstream reed only, the downstream reed only, and both reeds simultaneously. Operation of the upstream reed results in a (peak) centerline velocity that is about half the velocity induced by the downstream reed. It appears that the reduction is associated with the downstream reed restricting the motion of the counter rotating vortices that are formed by the upstream reed. It is also noteworthy that when both reeds are operated in concert, the resulting centerline velocity is 35% lower than the sum of the two, suggesting that the interaction between the reeds is not optimal.

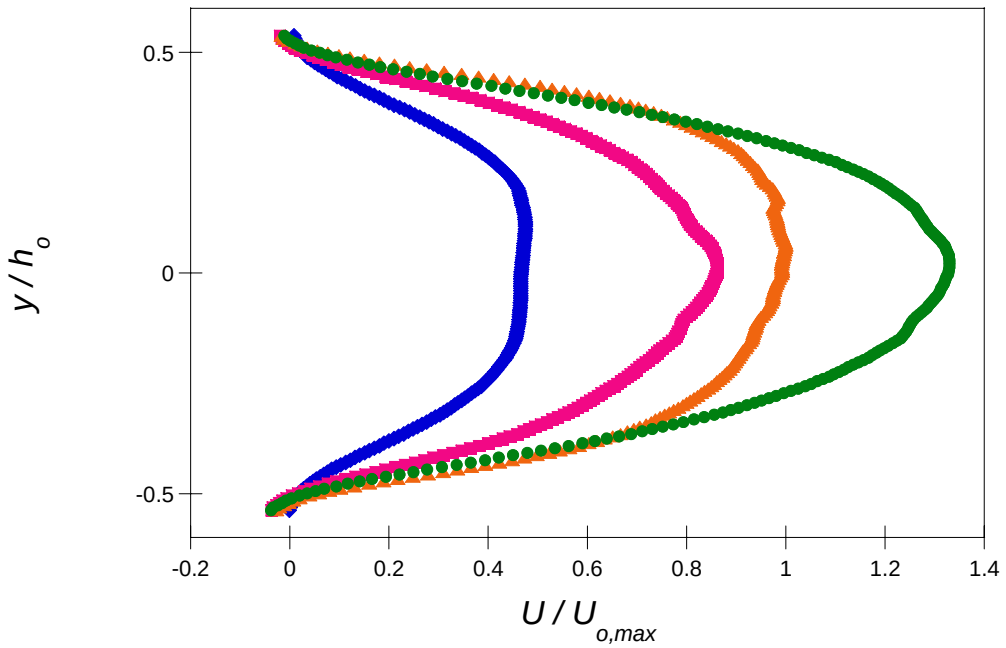

Figure 3.25: Cross stream velocity at the channel exit: upstream reed (◆), downstream reed (■), both reeds (▲), upstream added to downstream (●); (x_s = 2.25 x_w, $U_{o,\,max}$ =1.16 m / s)

The main benefit of using two reeds in tandem is the increased head. The static pressure for the tandem configuration was measured along the center of the top channel wall. Figure 3.26 shows the measured streamwise static pressure distribution for the both reeds operating in-phase, only the upstream reed operating, and only the downstream reed operating. The pressure profile of the standard channel is also shown for comparison superimposed near the upstream reed profile. The pressure is normalized using the average velocity obtained for each corresponding configurations. Under the condition of the both reeds operating, ΔH_r across the tip of the upstream reed is 52% larger than the downstream reed. The coefficient of pressure upstream of the tip of the upstream reed ($x / h_o < -1$) compares closely with the standard channel, but has a much lower ΔH_r. This is attributed to the higher velocity obtained using the two reeds. Also, because the tandem channel is approximately twice the length of the standard channel, the pressure loading is

considerably greater. The C_p measured while operating only the upstream reed has a much larger magnitude, even though the absolute pressure is nearly the same. This is attributed to the lower velocity obtained with operating the upstream reed only. With only the downstream reed operating, once again the absolute pressure is similar, but because of the lower velocity, compared to both reeds vibrating, C_p is lower in magnitude.

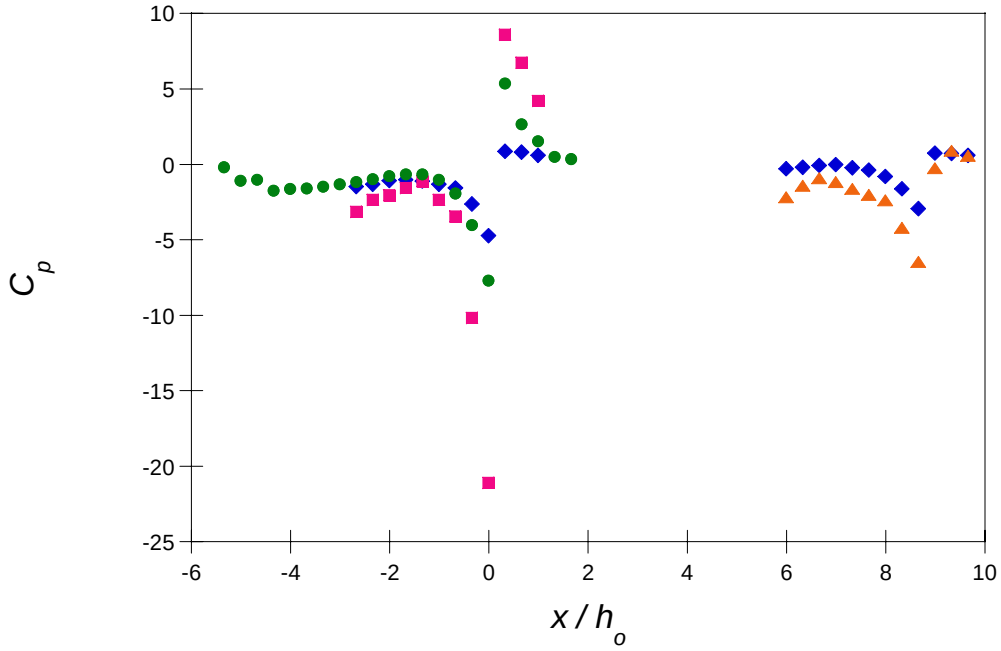

Figure 3.26: Streamwise distribution of pressure for tandem reed configuration with both reeds operating (◆), upstream reed only (■), downstream reed only (▲), and standard channel configuration (●)

3.4. Parallel Reed Configuration

Based on analogy to pumps it is expected that placing two reeds in parallel leads to an increase in volume flow rate for a given available head. A schematic diagram of the parallel reed configuration is shown in Figure 3.27. The channel length is the same as for the single reed, but the height is doubled. The channel has a thin, removable dividing wall

between the two reeds that allows testing of the interactions between the reeds which can result in different flow characteristics. The two reeds are operated at the same resonant frequency and identical $A_{p\text{-}p}$.

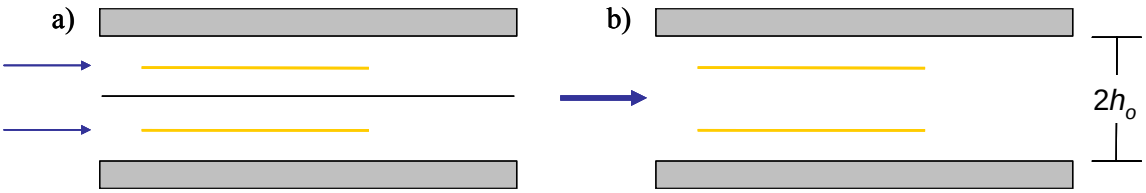

Figure 3.27: Parallel reed configuration; a) with divider, b) without divider

Perhaps the most important parameter in the parallel flow channel is the phase difference ($\Delta\Phi$) between the two reeds. The time-averaged centerline streamwise velocity distributions at $x / h_o = 1.3$ for various $\Delta\Phi$ are shown in Figure 3.28. The velocity is normalized by the maximum velocity obtained from the reeds with the dividing wall inserted. The phase difference was varied from 0° to 180° by shifting the bottom reed in phase increments of 45° ahead of the top reed. The velocity distribution for the configuration of the two reeds with a dividing partition is also shown for reference and the symmetry of the distribution is an indication that the two reeds are nearly identical. In the absence of the partition, the flow interactions induced by the reeds are evident in the phase-dependent distribution. At $\Delta\Phi = 0°$, the velocity distribution is nearly symmetric about $y = 0$ and velocity peaks are closer to the walls, which could indicate higher heat transfer from the walls. The peak velocity is nearly identical to that of the flow with the dividing partition. As the phase difference between the two reeds is altered there is a substantial variation in the velocity distribution. As the phase angle is increased (i.e. the

bottom reed leading), the distribution becomes skewed and the maximum velocity occurs near the bottom surface while the velocity near the top surface decreases. This is most prominent when $\Delta\Phi = 90°$ where $U / U_{o,\,max} = 1.15$ and 0.63 at $y / h_o = -0.71$ and 0.51, respectively. Being able to shift high velocity fluid to the bottom surface could be used to enhance heat transfer along the wall.

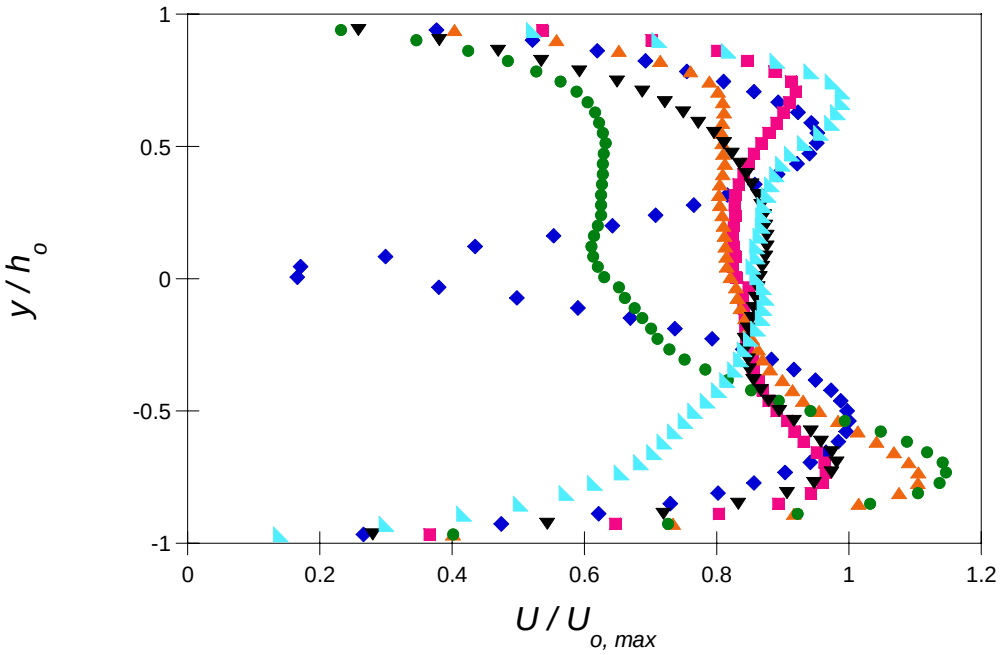

Figure 3.28: Time-averaged, normalized velocity of reed driven flow in parallel reed configuration for $\Delta\Phi$ = 0° (■), 45° (▲), 90° (●), 135° (▼), 180° (◣), divided flow (◆) ($U_{o,\,max}$ = 0.85 m / s, x / h_o = 1.3, St = 0.55)

The corresponding variation of overall volume flow rate in the channel (based on centerline velocity) is shown in Figure 3.29. The volume flow rate has been normalized with the volume flow rate of the two divided reeds. Placing two reeds in parallel results in a total volume flow rate that is slightly higher than twice the flow of a single reed (up

to 2.25 Q_o). The variation with phase with is relatively small (±8%) indicating that the interactions between the reeds (at least at this spacing) may have a secondary effect.

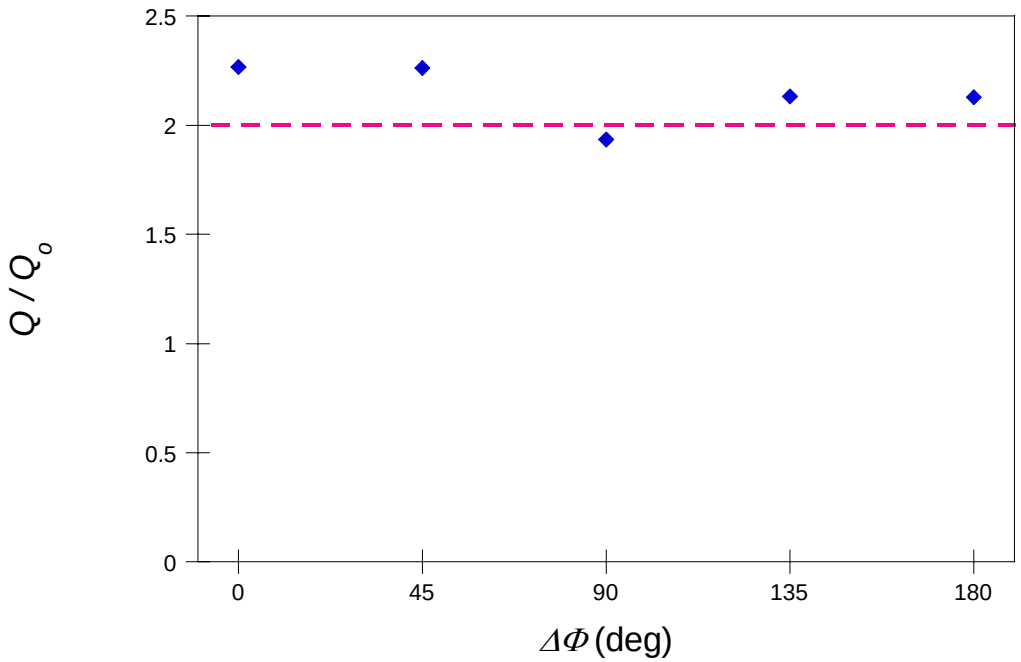

Figure 3.29: Variation with phase of volume flow rate for parallel reed configuration, normalized with Q_o of single reed; total Q of two reeds with partition (- -) (Q_o = 0.55 CFM)

It is instructive to investigate the interactions of the induced flows in the absence of a partition. The phase-averaged vorticity concentrations near the tip of the parallel reeds are shown for $\Delta\Phi = 0°$ and 180° in Figure 3.30 and Figure 3.31 respectively. When $\Delta\Phi = 0°$ (Figure 3.30), CW and CCW vortices are formed only between the outer surface of each of the reeds and the adjacent channel surface. Since the two reeds move synchronously there is no flow separation between them, and therefore no vortex formation, but as shown in Figure 3.30 there is net flow between the reeds for all phases. Similar to the single reed, as each vortex is formed its trajectory first follows the motion of the reed before moving downstream. Similarly, after moving downstream the vortices

also move in the cross stream direction towards the opposite wall. When $\Delta\Phi = 180°$ (Figure 3.31), a CW and CCW vortex pair is formed at the tip of each reed during each cycle. As the two reeds move towards each other ($t / T < 0.5$), a CCW vortex is formed on the outer surface of the upper reed and a CW vortex on the lower reed, and then they are advected downstream together by the induced flow. The trajectory of these vortices follows the motion of the reed at first, but unlike the vortices formed by the single reed or the parallel reeds at $\Delta\Phi = 0°$, the cross stream trajectory never extends beyond the channel centerline ($y = 0$). As the reeds move apart ($t / T > 0.5$), a CW vortex is formed on the inner surface of the upper reed and a CCW vortex on the lower reed, and then these are advected downstream. The phase-averaged velocity indicates that as the reeds move towards each other the net flow is vectored downstream (outward), whereas when the reeds separate, the net flow turns upstream (inward).

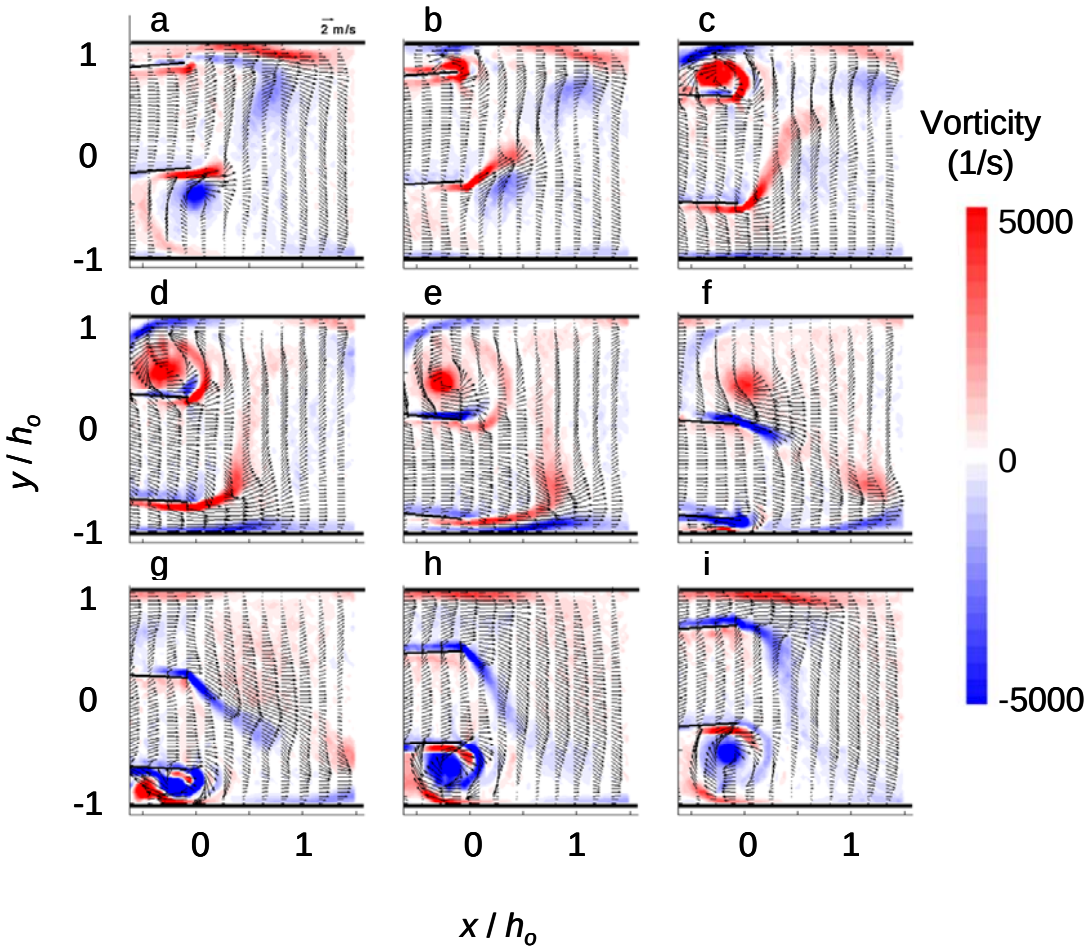

Figure 3.30: Vorticity of parallel reed configuration ($\Delta\Phi = 0°$); $t / T = 0$ (a), 0.11 (b), 0.22 (c), 0.33 (d), 0.44 (e), 0.55 (f), 0.66 (g), 0.77 (h), 0.88 (i) ($St = 0.49$)

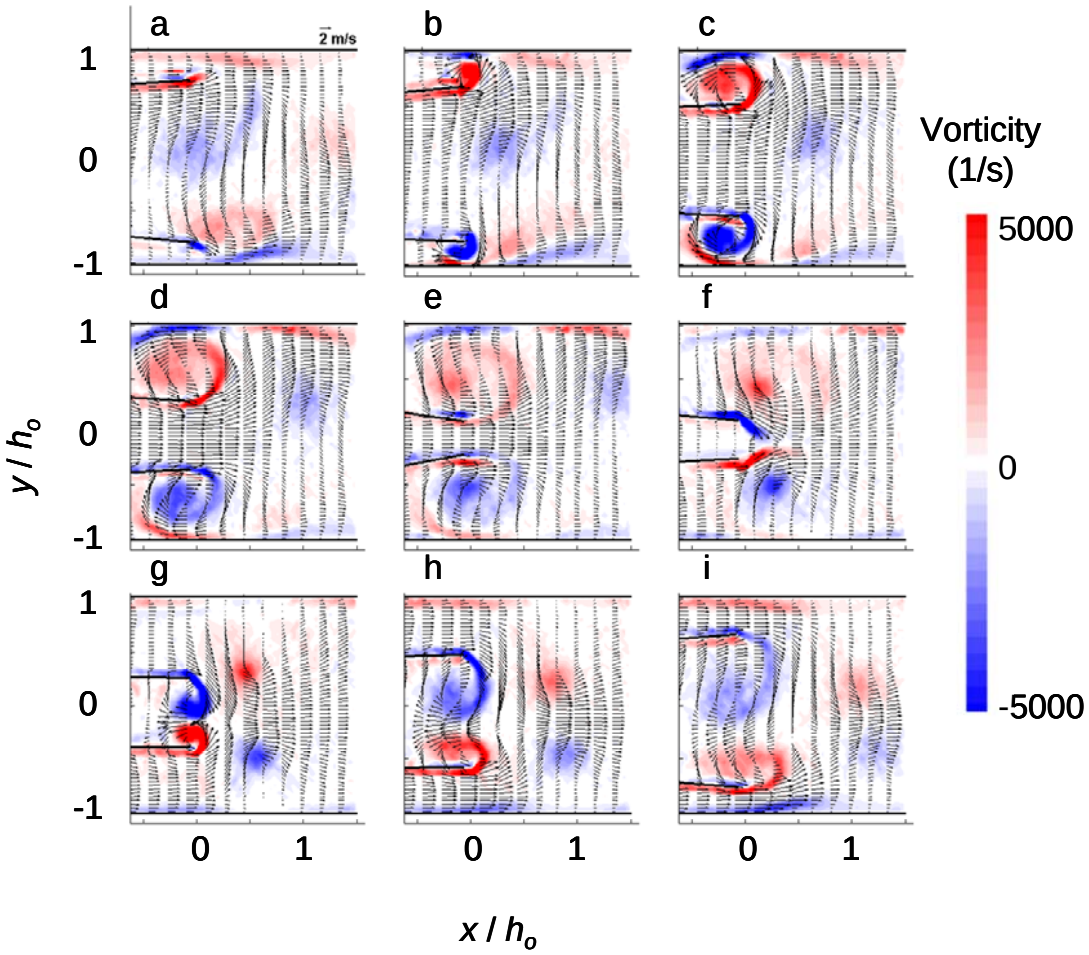

Figure 3.31: Vorticity of parallel reed configuration ($\Delta\Phi = 180°$); $t / T = 0$ (a), 0.11 (b), 0.22 (c), 0.33 (d), 0.44 (e), 0.55 (f), 0.66 (g), 0.77 (h), 0.88 (i) ($St = 0.52$)

The presence of vortices results in enhanced mixing within the channel, and may lead to increased heat transfer. The phase-averaged distributions of KE_f for $\Delta\Phi = 0°$ and 180° are shown in Figure 3.32 and Figure 3.33 respectively. When $\Delta\Phi = 0°$, no KE_f is present between the reeds from $t / T = 0$ - 0.11 and 0.5 - 0.61 (Figures 3.31a-b, f). After $t / T = 0.11$ and 0.61, the KE_f between the reed emanates from upstream and is ejected out into the flow. As noted previously, the flow between the reeds is always flowing downstream so it is conjectured that this flow does not immediately mix with the air near the walls, likely reducing the potential heat transfer. Just as in the single reed

experiments, the maximum phase-locked KE_f corresponds directly to the center of the vortices. Figure 3.30f and Figure 3.32f both show the maximum intensity (vorticity and KE_f) at $x / h_o = 0.25$ and $y / h_o = 0.35$. When $\Delta\Phi = 180°$ the KE_f between the reeds is generated from flow being entrained away from the walls, due to the cyclic velocity vectoring. No KE_f is present at $t / T \approx 0.5$ (Figures 3.32f-g), but as the reed moves apart, KE_f is generated between the reed (Figure 3.33h) due to the flow separation. The flow between the reeds mixes directly with the air near the walls. This condition will likely lead to higher heat transfer as it induces mixing across the channel height more directly.

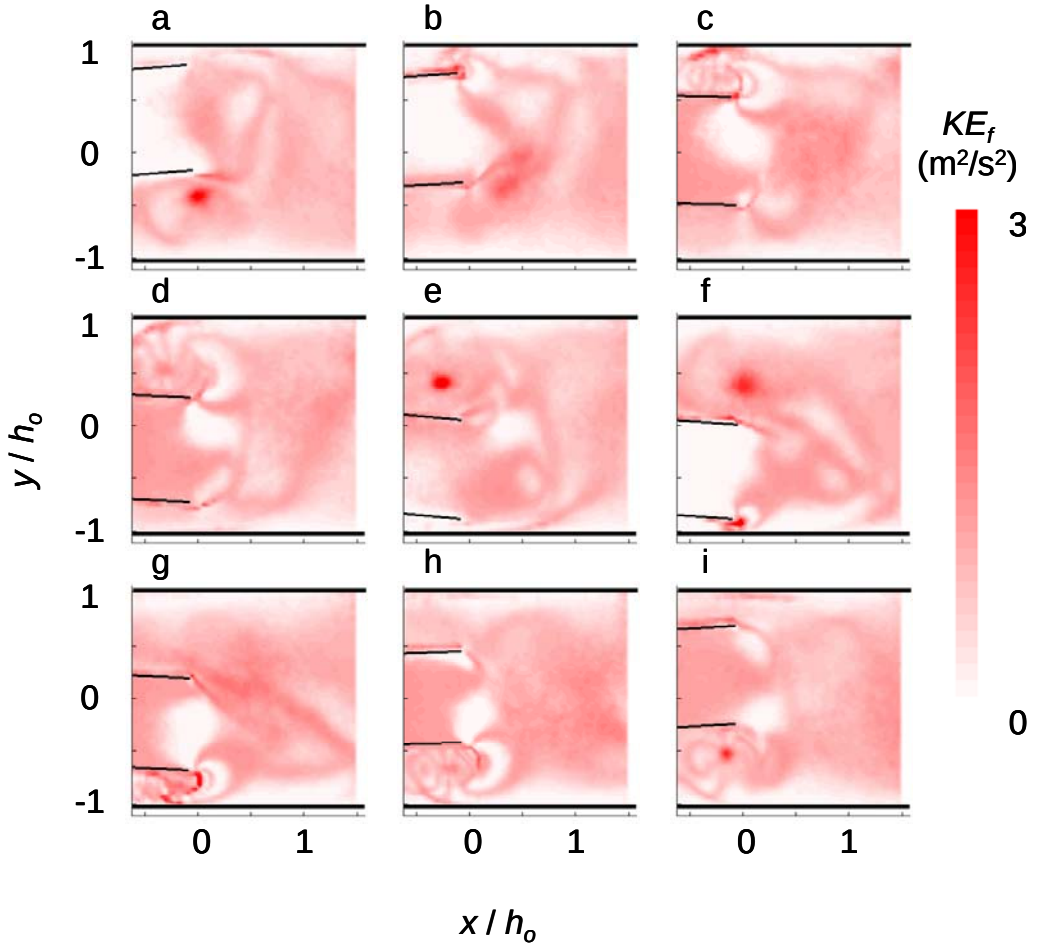

Figure 3.32: Fluctuation kinetic energy of parallel reed $\Delta\Phi = 0°$; $t / T = 0$ (a), 0.11 (b), 0.22 (c), 0.33 (d), 0.44 (e), 0.55 (f), 0.66 (g), 0.77 (h), 0.88 (i) ($St = 0.49$)

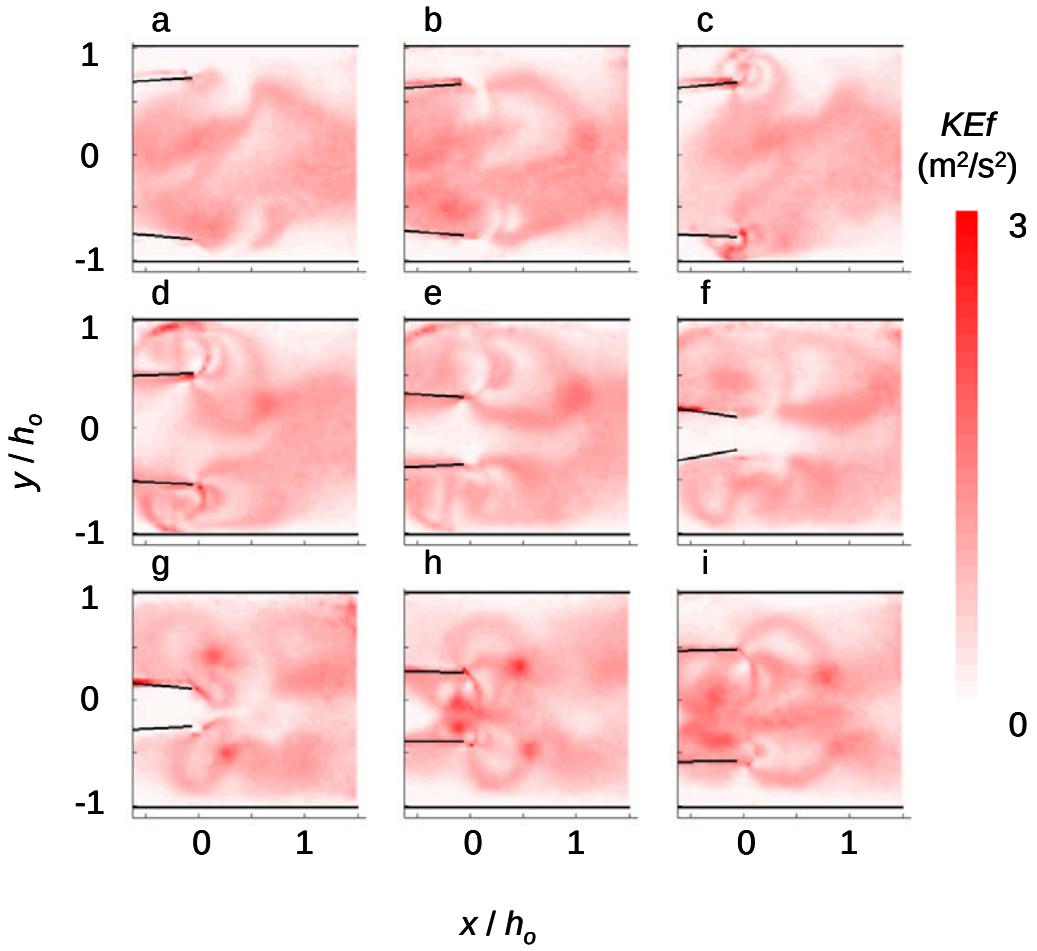

Figure 3.33: Fluctuation kinetic energy of parallel reed $\Delta\Phi = 180°$; $t / T = 0$ (a), 0.11 (b), 0.22 (c), 0.33 (d), 0.44 (e), 0.55 (f), 0.66 (g), 0.77 (h), 0.88 (i), ($St = 0.52$)

The streamwise pressure distribution on the channel walls when the parallel reeds are active is shown in Figure 3.34 for various $\Delta\Phi$. The pressure of the top half of the channel (with center divider inserted) is also shown for comparison. It is noteworthy that the pressure distribution is hardly affected by the dual reed configuration, and is independent of $\Delta\Phi$. While the head provided by the dual reeds is almost unchanged from the single reed, the flow rate is more than doubled.

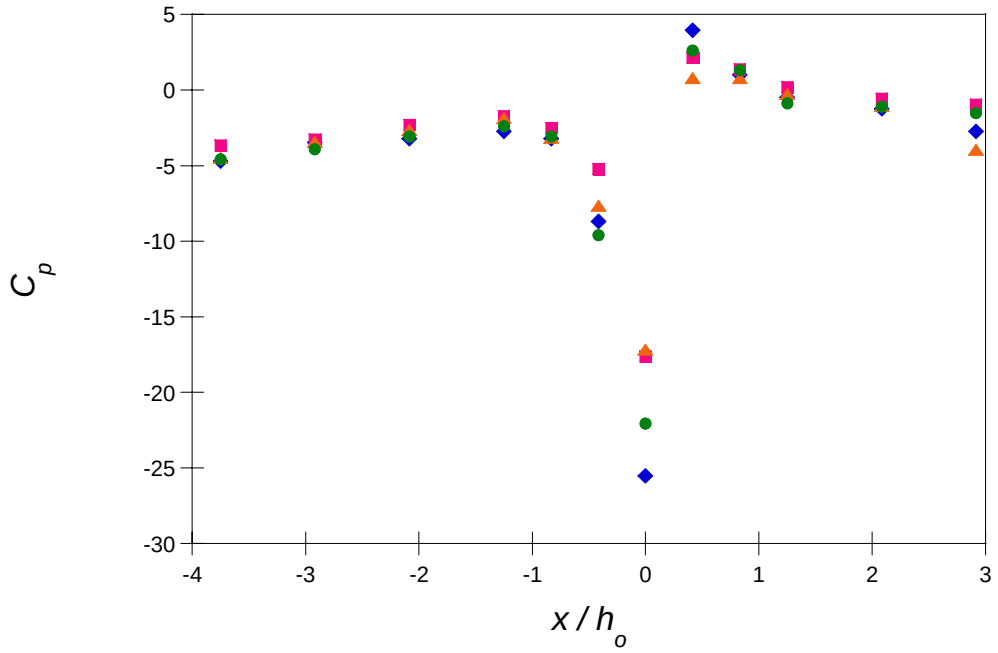

Figure 3.34: Static pressure profile along channel wall for parallel reed configuration for $\Delta\Phi = 0°$ (■), 90° (▲), 180° (●), divided flow (◆)

3.5. Increased Channel Width

The effect of the separation distance between the reed and the channel top and bottom walls is accounted for by varying $A_{p\text{-}p}$. The effect of increasing the width of the channel, while keeping the width of the reed the same, was investigated to determine the how the reed to wall spacing in the spanwise direction affects the flow. Figure 3.35 shows the time-averaged velocity distributions and cross stream component of vorticity, across the span of the channel for six different channel widths. At the exit, the peak centerline velocity varies by ±13%, with the peak velocity occurring at $w / w_r = 1.26$. The volume flow rate, assuming a constant velocity across the height, shows the same trend in Figure 3.36. As the width is increased, the volume flow rate increases until $w / w_r = 1.26$, and then becomes asymptotic. The volume flow rate for the wider channel is approximately

1.4 Q_o, where Q_o is the flow obtained with the standard channel width (1.1 w_r). When the channel width is reduced to $w / w_r = 1.05$, the flow is reduced to 0.78 Q_o. Figure 3.35 also shows that as the width is increased, there is a secondary jet effect at the channel sidewalls near the tip of the reed. As the width is increased, this secondary jet increases in velocity and extends farther down the length of the channel. For $w / w_r = 1.58$, at $x / h_o = 2.62$, the peak of the secondary jet occurs at $z / w_r = \pm 0.63$ and has a magnitude of velocity 45% of the peak centerline velocity. There is a large region of vorticity associated with the secondary jet extending away from the channel sidewalls to approximately $z / w_r = \pm 0.5$ for all width ratios. This secondary velocity peak near the sidewalls would be highly beneficial for cooling if the sidewalls are heated.

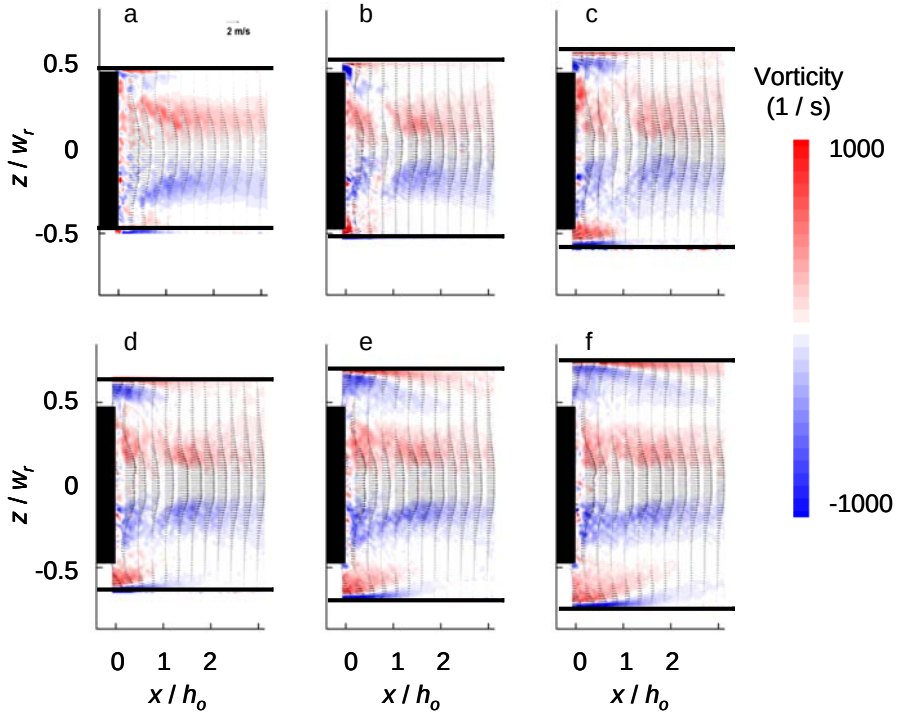

Figure 3.35: Time-averaged velocity distributions and cross stream component of vorticity, across the span of channel for $w / w_r = 1.05$ (a), 1.10 (b), 1.26 (c), 1.37 (d), 1.47 (e), and 1.58 (f) ($y / h_o = 0$, $w_r = 25.4$ mm, $A_{p\text{-}p} / h_o = 0.56$, $f_{res} = 78$ Hz)

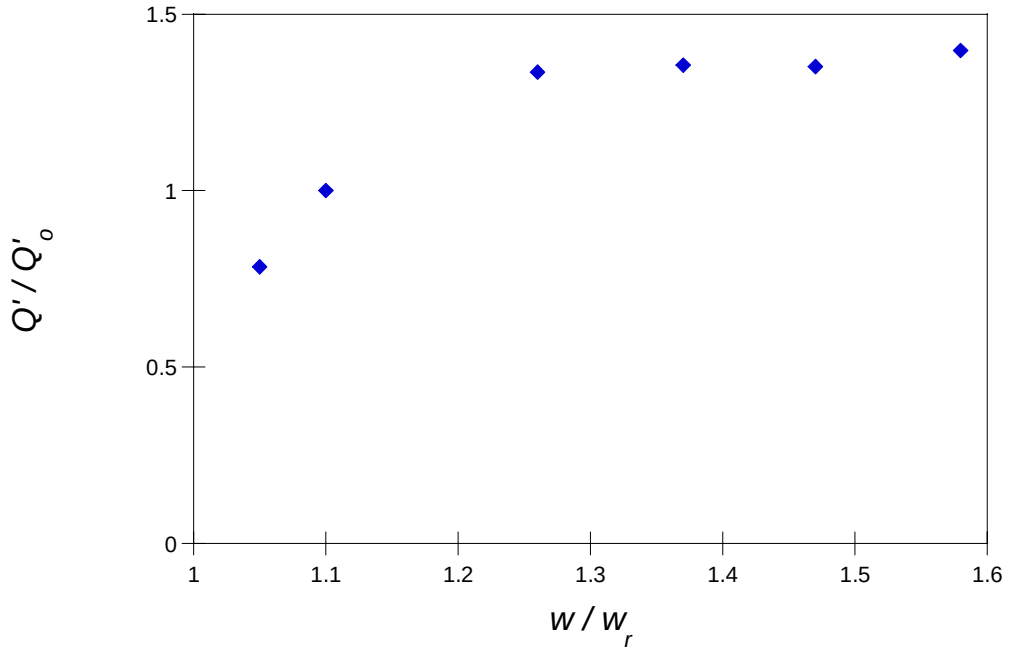

Figure 3.36: Effect of increasing the channel width while keeping the reed width constant at $x / h_o = 2.6$ ($Q_o' = 0.25$ CFM, $w_r = 25.4$ mm)

The turbulent kinetic energy of the flow for the six channel widths is shown in Figure 3.37. The intensity level remains invariant for all widths although the KE_f does propagate farther downstream as w / w_r is increased to 1.26, and then saturates. The spanwise width of the KE_f remains constant for all w / w_r, similar to that seen in the vorticity plots. Also, similar to the vorticity, there is an increase in penetration of the KE_f away from the sidewalls for increasing w / w_r. The heat transfer will likely be increased by the increased streamwise KE_f propagation distance.

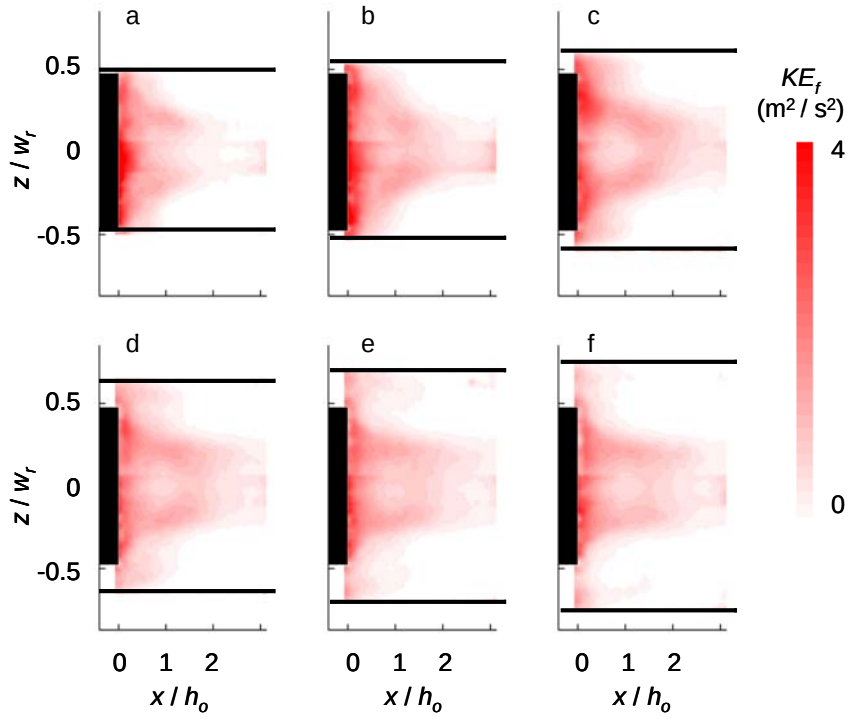

Figure 3.37: Time-averaged turbulent kinetic energy across the span of channel for w / w_r = 1.05 (a), 1.10 (b), 1.26 (c), 1.37 (d), 1.47 (e), and 1.58 (f) (y / h_o = 0, w_r = 25.4 mm, $A_{p\text{-}p} / h_o$ = 0.56, f_{res} = 78 Hz)

3.6. Converging Channel

The effect of converging the channel side walls relative to the reed (Figure 3.38) was also investigated. The earlier work of Yoo et al. (2000) suggested that altering the reed shape does not improve the flow characteristics, but the results of §3.5 indicate that the sidewall spacing effects the flow characteristics, therefore the angle may also have an effect. Figure 3.38 schematically shows a top view of the experimental setup for the angled wall channel configuration. The reed is shown with the direction of the airflow indicated. The width of the channel exit remains constant to all other experiments at 1.1 w_r. The sidewall angle is altered by placing stereolithograph inserts between the base plate and the sidewall. Only small angles were considered ($\alpha < 10°$).

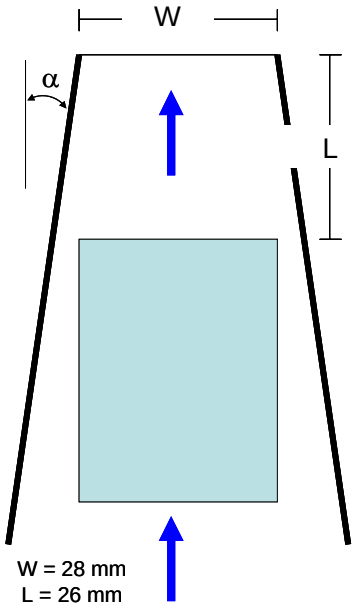

Figure 3.38: Top view of configuration of angled channel sidewalls

Phase-locked velocity and the vorticity distributions for $\alpha = 2.5°$, 5°, and 10° are shown in Figures 3.38a-i through Figures 3.40a-i respectively for the first half of the cycle ($t / T = 0$ - 0.5). Two lines are overlaid on the figures to show the approximate difference in the propagation velocity, U_{prop}, of the vortices present in the first half of the cycle (CCW vortex as it forms) and the second half of the cycle (CW vortex as it moves downstream). The formation evolution of these vortices is similar to that discussed for the straight wall channel ($\alpha = 0°$), so only half the cycle is shown for brevity. Similar to Figure 3.4, as the vortices form, they move in the cross stream direction with the motion of the reed before propagating downstream for $t / T > 0.5$. As the wall angle increases, the propagation velocity of the CW vortex (formed in the second half of the previous cycle) does not increase significantly (2.04 m / s for $\alpha = 2.5°$, 2.27 m / s for $\alpha = 10°$). The propagation velocity of the CCW vortex as it forms though does increase significantly.

When $\alpha = 2.5°$, 5°, and 10°, $U_{prop} = 0.61$ m / s, 0.79 m / s, and 1.25 m / s, respectively. This increase in U_{prop} results in the CW vortex moving 0.36 h_o farther downstream from $\alpha = 2.5°$ to 10° at $t / T = 0$ (Figures 3.37a and 3.39a). Increasing the convergence angle also increases the cross stream velocity transport at the channel walls, as can be seen along the bottom channel wall in Figures 3.37 - 3.39i. For $\alpha = 2.5°$ (Figure 3.39i), the velocity transport only extends to $x / h_o = 0.65$ and $y / h_o = -0.44$, whereas for $\alpha = 10°$ (Figure 3.41i) it extends to $x / h_o = 1.1$ and $y / h_o = -0.29$.

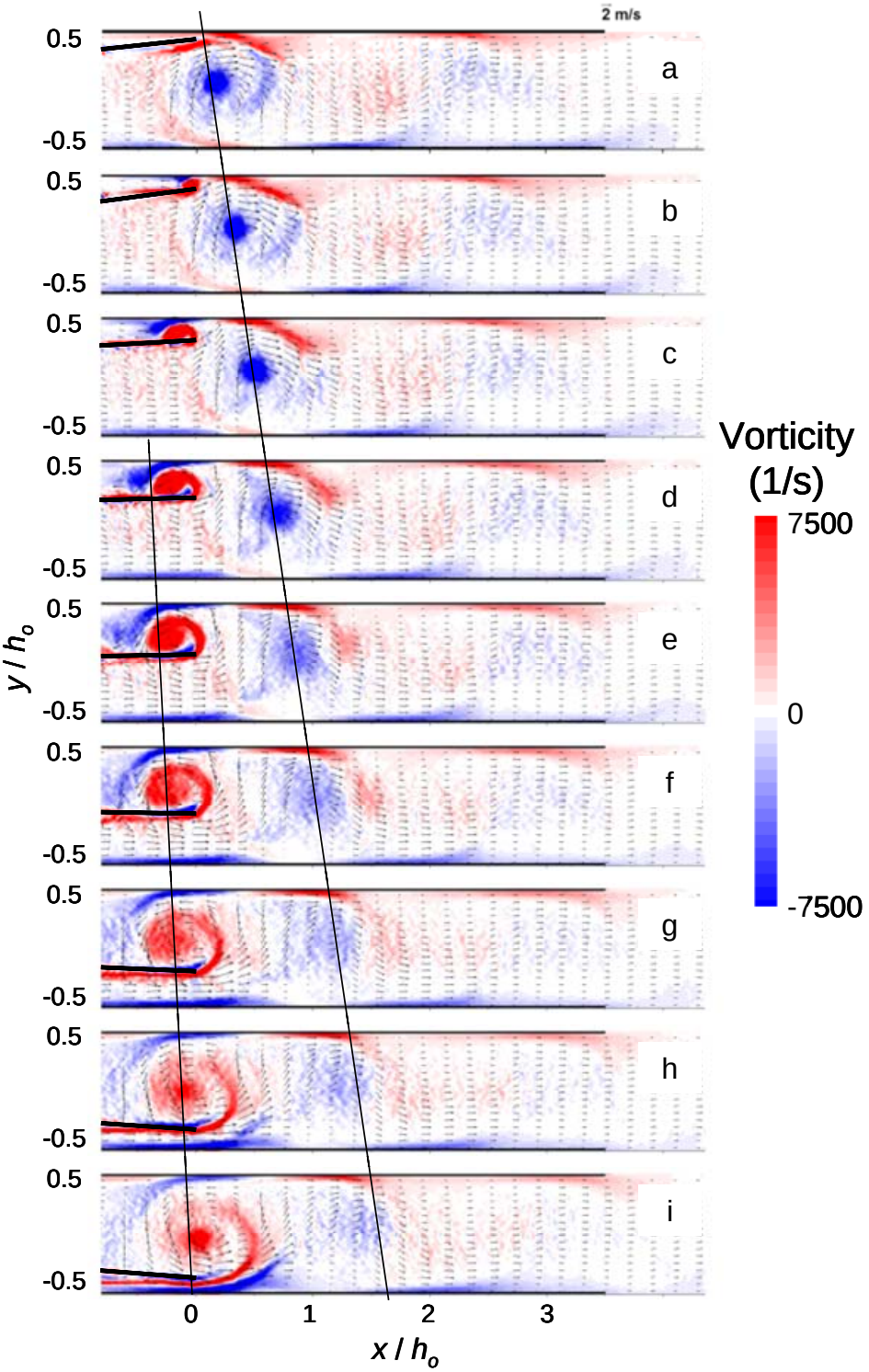

Figure 3.39: Phase-averaged velocity and vorticity distributions for converging channel configuration, one half of complete cycle, α = 2.5°, t / T = 0 (a), 0.06 (b), 0.11 (c), 0.17 (d), 0.22 (e), 0.28 (f), 0.33 (g), 0.39 (h), and 0.44 (i) (St = 0.50)

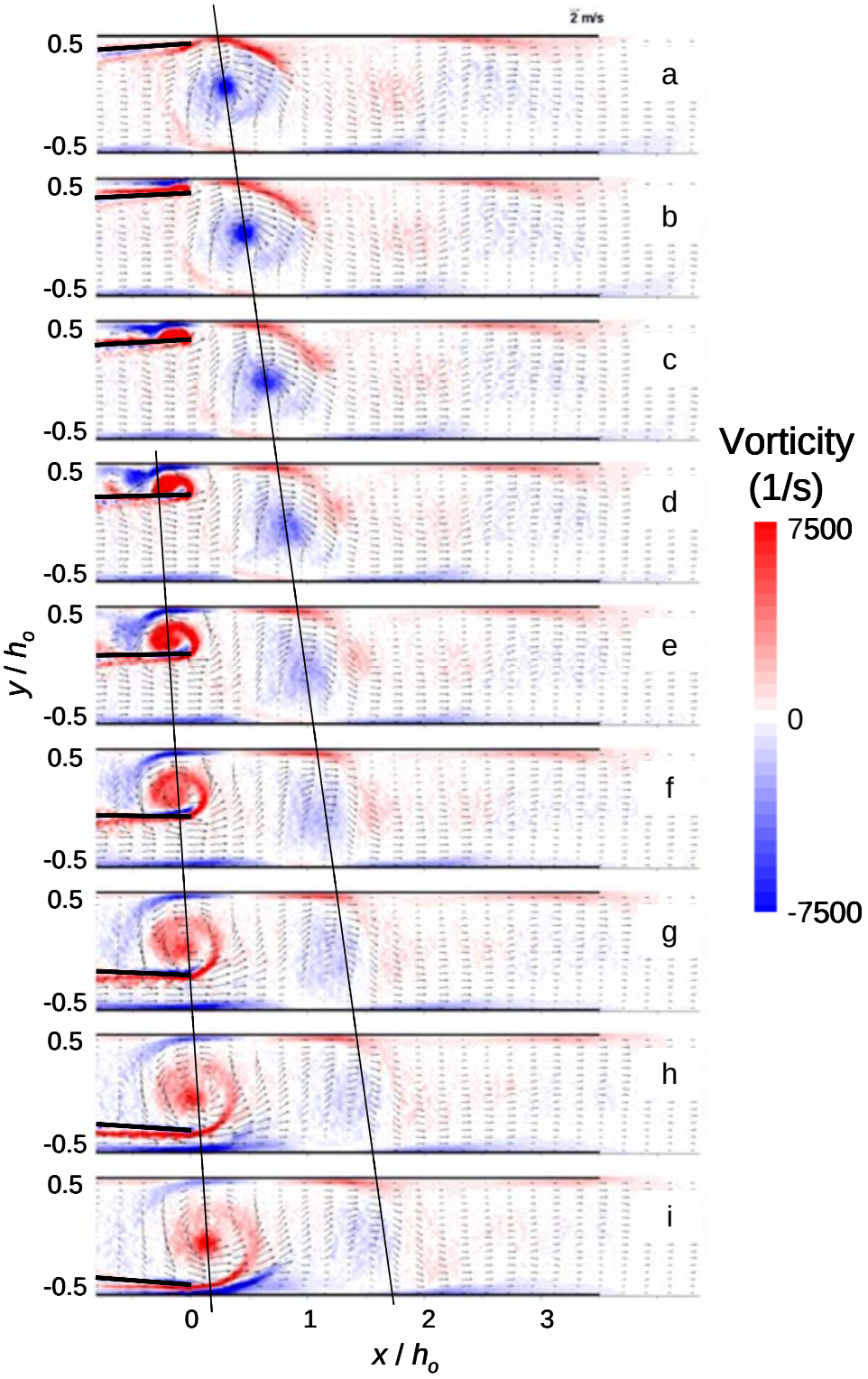

Figure 3.40: Phase-averaged velocity and vorticity distributions for converging channel configuration, one half of complete cycle, α = 5.0°, *t* / *T* = 0 (a), 0.06 (b), 0.11 (c), 0.17 (d), 0.22 (e), 0.28 (f), 0.33 (g), 0.39 (h), and 0.44 (i) (*St* = 0.45)

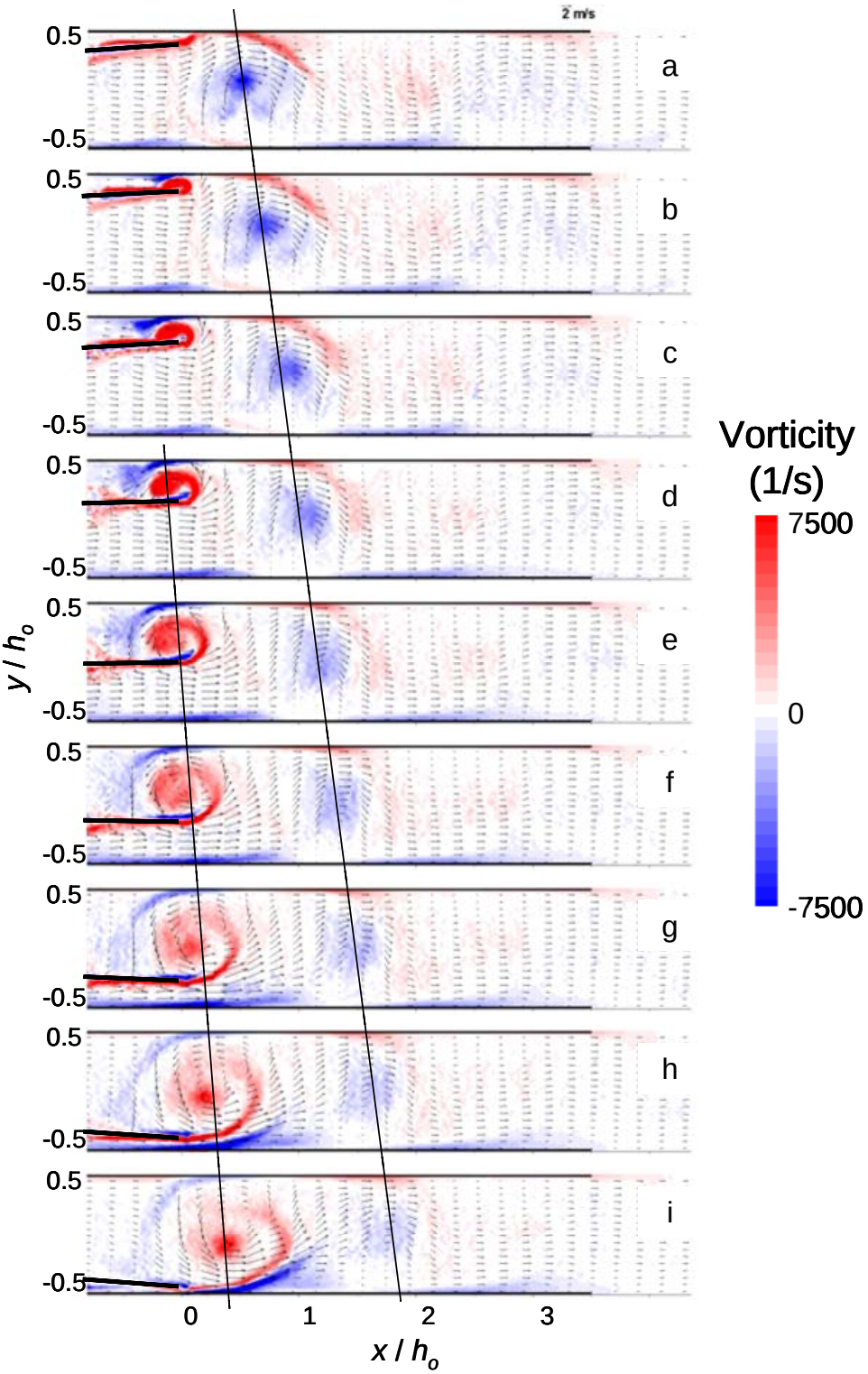

Figure 3.41: Phase-averaged velocity and vorticity distributions for converging channel configuration, one half of complete cycle, α = 10°, t / T = 0 (a), 0.06 (b), 0.11 (c), 0.17 (d), 0.22 (e), 0.28 (f), 0.33 (g), 0.39 (h), and 0.44 (i) (St = 0.45)

The time-averaged streamwise distribution of turbulent kinetic energy is shown in Figures 3.40a-c for $\alpha = 2.5°$, 5°, and 10° respectively. As seen with the vorticity distribution, as α increases from 2.5° to 10°, the center of maximum KE_f intensity moves downstream by $x = 0.12\ h_o$. The total downstream propagation distance of KE_f is nearly invariant with angle though. Although the effect of angle is not significant, these results do show that it may be possible to relocate the maximum local heat transfer coefficient if desired.

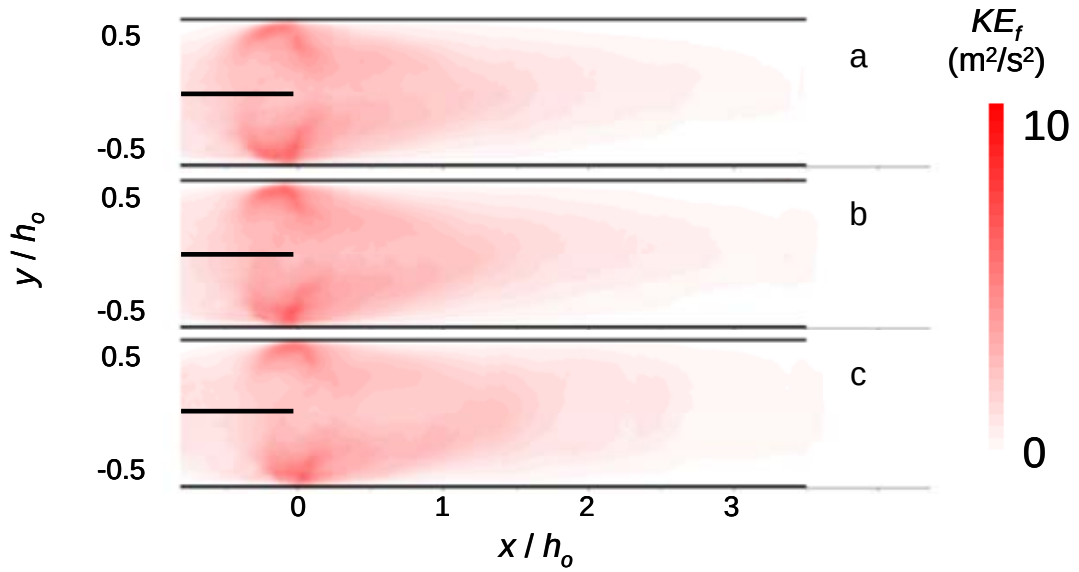

Figure 3.42: Time-averaged distribution of KE_f of converging channel for α = 2.5° (a), 5° (b), and 10° (c)

3.7. Reed-Augmented Steady Flow

In heat transfer applications where a higher volume flow rate of the cooling flow is needed to transport heat away from the channel, the reed may be combined with a time-invariant bulk flow that is driven by an air source or a blower. As stated previously,

the reed-induced flow has two primary advantageous effects. First it disrupts the thermal boundary layer that forms on the channel's walls and enhances the local heat transfer coefficient. Second, the unsteady, reed-induced flow enhances mixing of the heated air with the cross stream core flow. These same advantages can also be introduced into a time-invariant bulk flow, resulting in what will be called reed-augmented flow.

In this segment of the present investigation, the flow channel has the same dimensions as in the earlier investigations (h_o = 7.62 mm, w = 1.1 w_r = 27.9 mm). A schematic diagram of the flow system is shown in Figure 3.43. The source flow is controlled with a needle valve. The air flows into an airtight plenum that diffuses the flow before moving through a diffuser with vanes at 2.5° flair (to reduce separation in the expansion) which is then sealed to the inlet of the channel. The volume flow rate of air is measured with an Aalborg GFC37 mass flow meter. The volume flow rate through the channel does not increase when the reed is activated. The steady volume flow rate, Q_{st}, can be varied, up to 1.65 CFM.

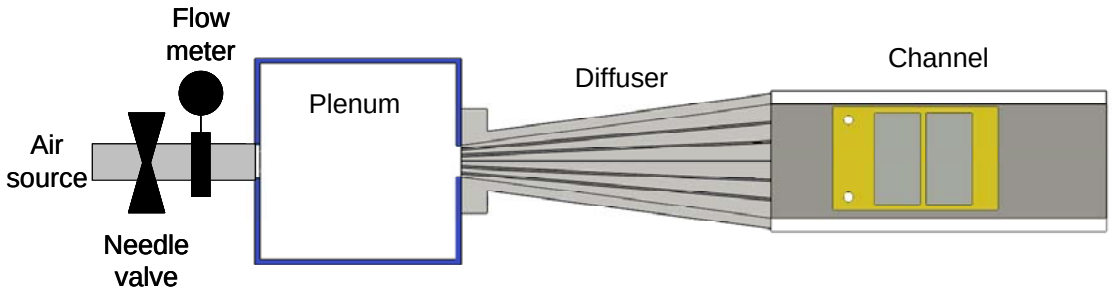

Figure 3.43: Schematic top view of reed-augmented steady flow

The increase in small scale mixing far downstream of the reed for increased Q_{st} is the result of the difference in the vortex formation and propagation in the channel. The phase-averaged velocity and vorticity distributions for the reed-augmented flow are shown in Figures 3.43a-i though Figure 3.45a-i ($Q_{st} = 0.35$, 0.71, and 1.06 CFM respectively). Lines showing the propagation speed of the vortices are once again shown for each figure. The displayed intensity levels of the vorticity in the three flows are held constant for comparison purposes. Figure 3.44 has a total volume flow rate comparable to Figure 3.1 (0.35 vs. 0.43 CFM), yet the formation of the vortices occurs in a vastly different manner. Because of the imposed steady flow, as the vortex is formed, it is immediately advected downstream, whereas the vortices in the reed-driven flow first moved across the height of the channel before moving downstream (as shown in Figure 3.4). At $t / T = 0.22$, the center of the CW vortex is at $x / h_o = 0.6$ and $y / h_o = 0$ for $Q_{st} = 0.35$ CFM, $x / h_o = 1.0$ and $y / h_o = -0.2$ for $Q_{st} = 0.71$ CFM, and $x / h_o = 1.86$ and $y / h_o = -0.22$ for $Q_{st} = 1.06$ CFM. From Figure 3.4, for reed-induced flow the CW vortex center is at $x / h_o = -0.08$ and $y / h_o = -0.07$. The propagation speeds are, $U_{prop} = 1.66$, 1.84, and 2.64 m / s for $Q_{st} = 0.35$, 0.71, and 1.06 CFM respectively. An increase in Q_{st} does not yield a corresponding increase in U_{prop} because the vortices do not propagate at the same y / h_o. At $x / h_o = 2$, the vortex center passes at $y / h_o = 0.38$, 0.80, and 0.75 for $Q_{st} = 0.35$, 0.71, and 1.06 CFM, respectively. Because the velocity near the wall is lower, U_{prop} is also lower. The vortices are advected at roughly the same elevation for $Q_{st} = 0.71$ and 1.06 CFM, and for a 50% increase in Q_{st}, the propagation speed increases by 43%.

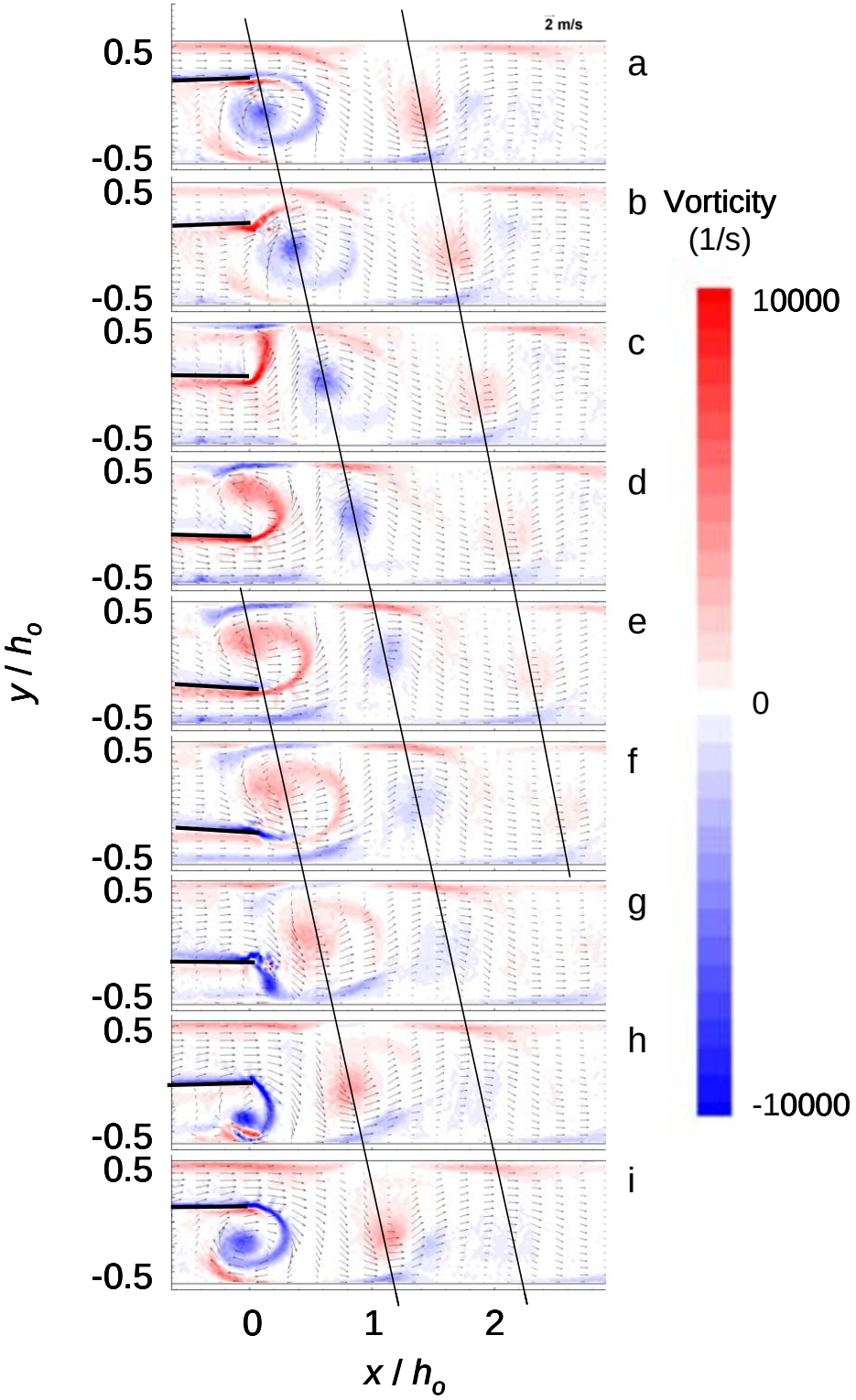

Figure 3.44: Distributions of phase-averaged vorticity and velocity within the channel of reed-augmented flow, $t / T = 0$ (a), 0.11 (b), 0.22 (c), 0.33 (d), 0.44 (e), 0.55 (f), 0.66 (g), 0.77 (h), and 0.88 (i) ($A_{p\text{-}p} / h_o = 0.32$ and $Q_{st} = 0.35$ CFM, $St = 0.38$)

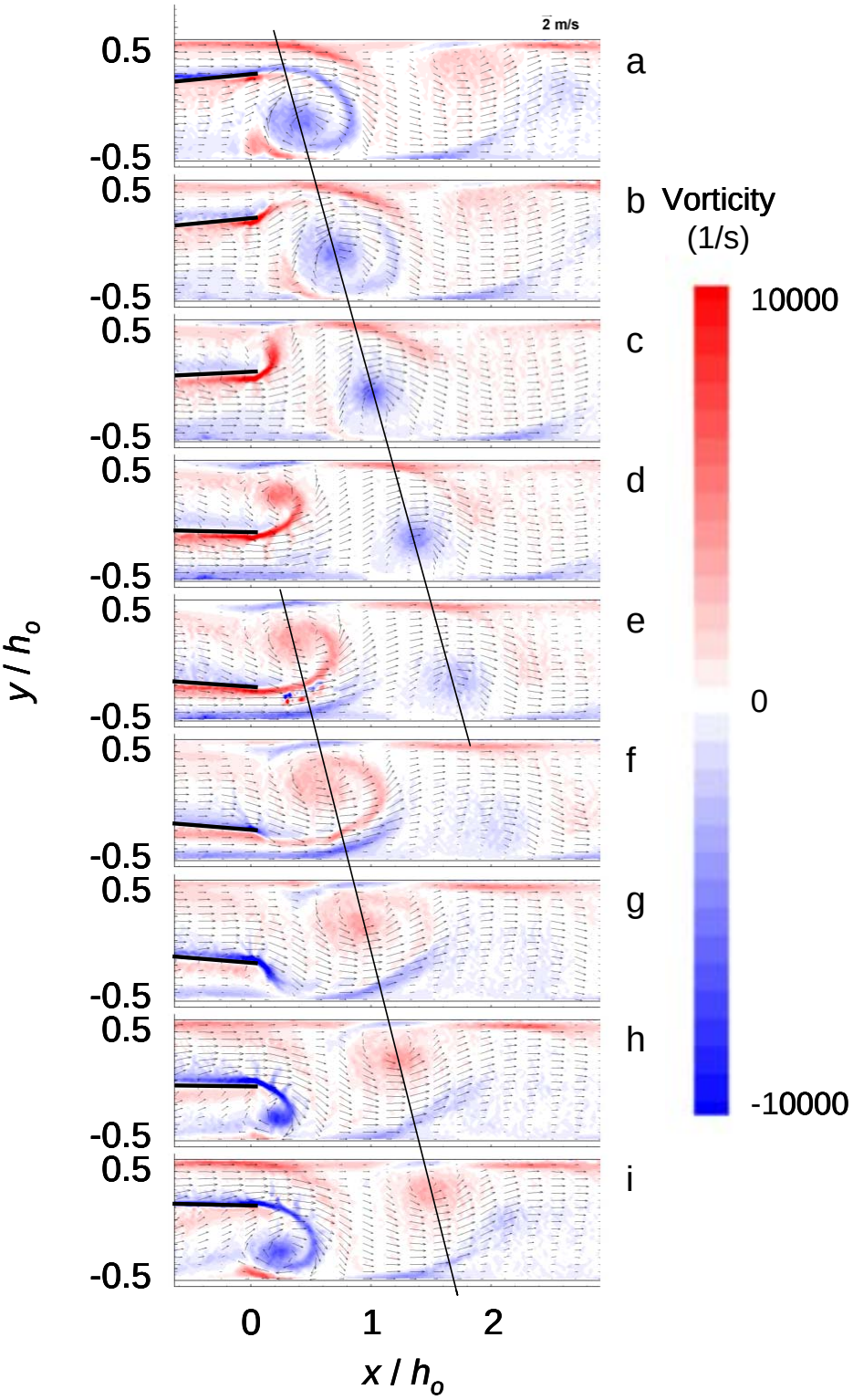

Figure 3.45: Distributions of phase-averaged vorticity and velocity within the channel of reed-augmented flow, $t / T = 0$ (a), 0.11 (b), 0.22 (c), 0.33 (d), 0.44 (e), 0.55 (f), 0.66 (g), 0.77 (h), and 0.88 (i) ($A_{p\text{-}p} / h_o = 0.32$ and $Q_{st} = 0.71$ CFM, $St = 0.19$)

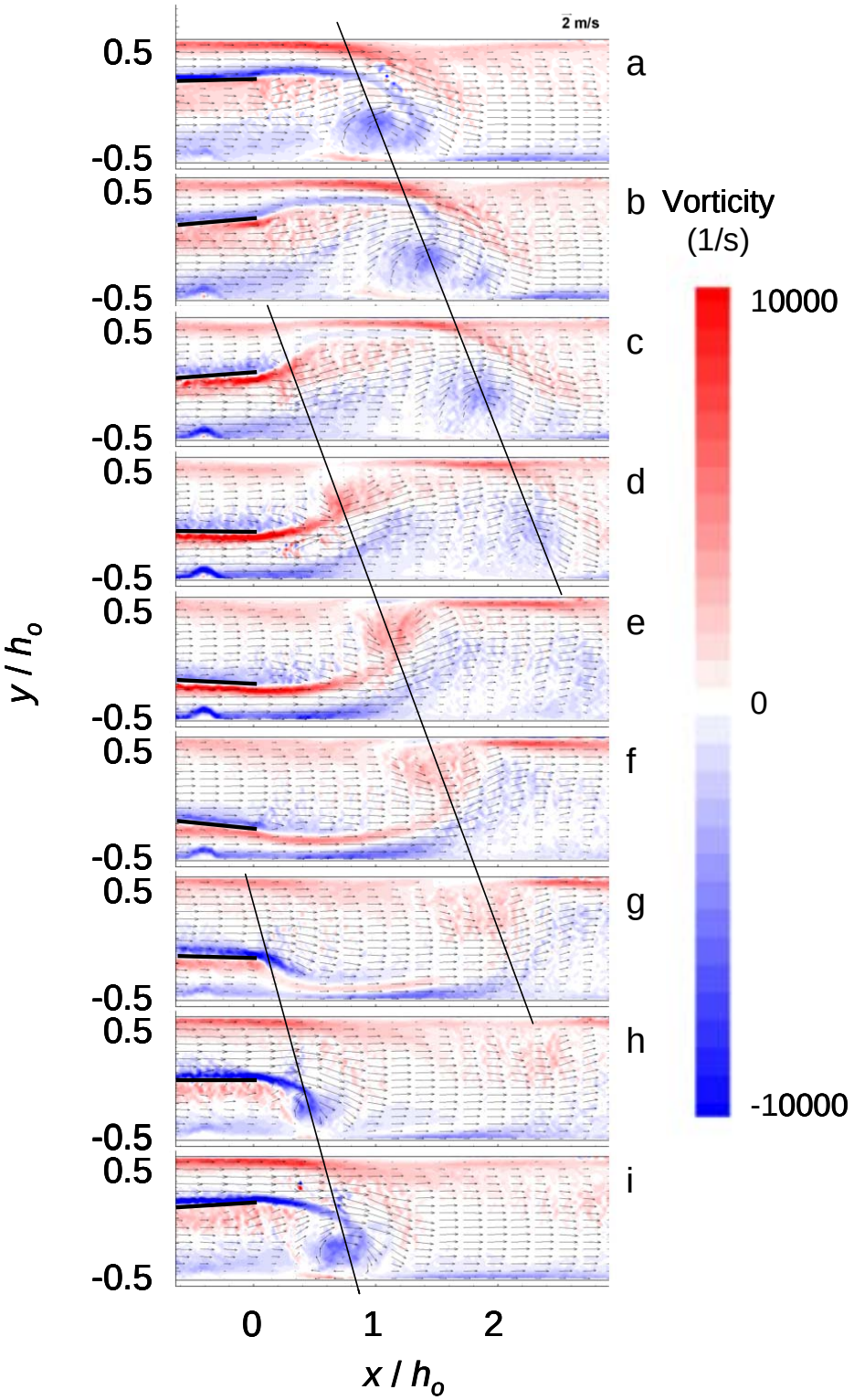

Figure 3.46: Distributions of phase-averaged vorticity and velocity within the channel of reed-augmented flow, $t / T = 0$ (a), 0.11 (b), 0.22 (c), 0.33 (d), 0.44 (e), 0.55 (f), 0.66 (g), 0.77 (h), and 0.88 (i) ($A_{p\text{-}p} / h_o = 0.32$, $Q_{st} = 1.06$ CFM, $St = 0.13$)

The most important flow characteristic of the reed-augmented flow is the additional small-scale mixing that occurs. It has been shown that the reed driven flow induces turbulent kinetic energy down the length of the channel, but with the superimposed steady flow, this mixing is enhanced farther down the length of the channel as shown in Figures 3.46a-e. Figure 3.47a shows the KE_f for steady flow ($Q_{st} = 0.35$ CFM) with the reed present in the channel, but not vibrating in the flow. As expected in steady, laminar channel flow, there is essentially no mixing present in the channel. Figures 3.46b-d show the effect that the vibrating reed has on the steady flow for $Q_{st} = 0.35$, 0.71, and 1.10 CFM respectively. All three flow rates indicate that the reed introduces a large region of mixing. Figure 3.47b indicates that the KE_f profile is similar to that found in reed-induced flow (Figure 3.14j) with the highest intensity at $x / h_o = 0.1$ and $y / h_o = \pm 0.38$. As Q_{st} is increased, the KE_f level both increases in intensity and propagates farther downstream due to the increased Q_{st} that propagates the vortices downstream faster, as seen in Figure 3.44 through Figure 3.46. Thus, as Q_{st} is increased the heat transfer coefficient should increase, and the localized heat transfer improvement should be present for longer downstream distances. Also, with any reed vibration, the KE_f is greatly increased, thus increasing the overall heat transfer immensely.

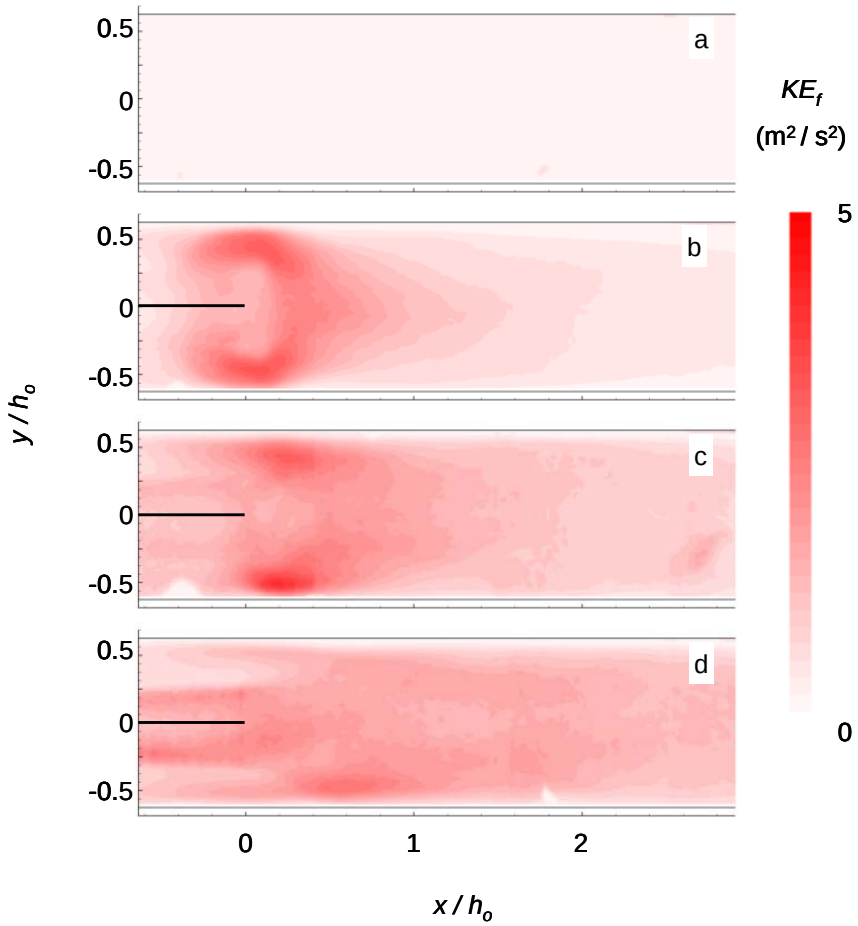

Figure 3.47: KE_f of a) steady flow at Q_{st} = 1.06 CFM, and reed-augmented flow at Q_{st} = 0.35 CFM (b), 0.71 CFM (c) and 1.06 CFM (d) ($A_{p\text{-}p} / h_o$ = 0.45)

The streamwise pressure distribution is shown for both the steady flow and reed-augmented flows in Figure 3.48 (Q_{st} = 0.35 CFM). The pressure in steady flow decreases linearly with downstream distance, approaching $C_p = 0$ at the exit. The static pressure distribution for the reed-augmented flow (Q_{st} = 0.35 CFM) has a similar shape to the reed-induced flow, but $C_p > 0$ just upstream of the tip, whereas the reed driven flow was always negative. This is likely due to the pressure head provided by the steady flow. The pressure just upstream from the tip drops faster though because of the faster downstream propagation of the vortices.

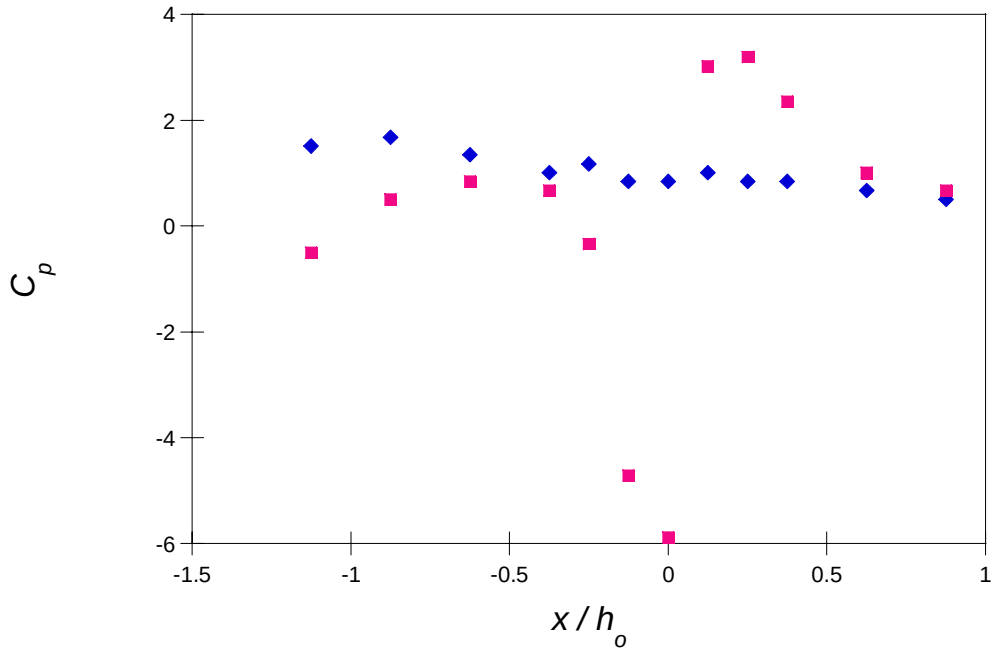

Figure 3.48: Static Pressure profile along channel for steady flow (◆) and reed-augmented flow (■) (Q_{st} = 0.35 CFM).

Chapter 4

Heat Transfer Enhancement by the Vibrating Reed

This section focuses on the effects of the small-scale motions induced by the vibrating reed on heat transfer from the duct surface. In particular, heat transfer is measured in the absence and presence of a bulk flow through the duct.

4.1. Experimental Setup

The experimental configuration for the heat transfer measurements is shown in Figure 4.1. The channel and reed dimensions are the same as discussed in §2.1 - 2. In all the present heat transfer experiments, the channel is mounted vertically to avoid complications from sporadic secondary flow induced by natural convection. The air flows from bottom to top while passing over the heated surface. The thermocouples on the backside of the resistance heater (§2.5) are used to determine the local heat transfer coefficient. The exit air temperature is monitored with a thermocouple sensor mounted on a controlled traverse having three degrees of freedom.

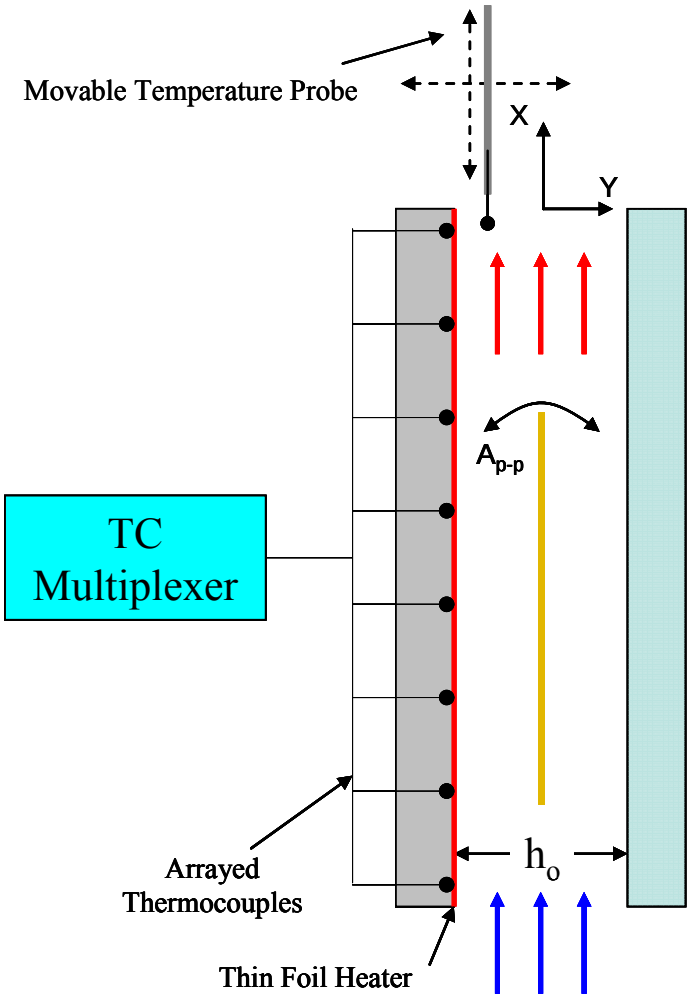

Figure 4.1: Schematic of channel for heat transfer measurements

The performance of the heated surface and the temperature sensors was tested in the absence of the channel side and top walls. The flat plate was cooled using natural convection and the measured surface temperature is compared with a known 2-D similarity solution for a vertical plate under natural convection conditions with variable surface temperature and constant heat flux (Kays and Crawford, 1980). To determine the plate surface temperature, the local Nusselt number, $Nu(x)$, ($x = 0$ is the leading edge of the plate) is computed from:

$$Nu(x) = \left(\frac{Pr}{4 + 9Pr^{0.5} + 10Pr} \right)^{0.2} \left(Gr^*(x)Pr \right)^{0.2} \tag{4.1}$$

where Pr is the Prandtl number (for air $Pr \approx 0.7$), and $Gr^*_{x_{LE}}$ is the modified, local Grashof number:

$$Gr^*_{x_{LE}} = Gr_{x_{LE}} Nu_{x_{LE}} = \frac{g\beta}{k_{air}\nu^2_{air}} Q''_{conv} {x_{LE}}^4 \tag{4.2}$$

where g is the gravitational acceleration, β is the Boussinesq approximation ($\beta = 1 / T_\infty$), k_{air} is the thermal conductivity of air (0.03 W / m K), ν_{air} is the kinematic viscosity of air (15.9×10^{-6} m^2 / s), and Q''_{conv} is the average heat flux per unit area due to convection (all air properties are evaluated at $T_{air} \approx 300$K).

The total power input, Q''_{tot} is dissipated by convective transport, radiation losses, Q''_{rad}, and conductive losses, Q''_{cond}.

$$Q''_{tot} = Q''_{conv} + Q''_{rad} + Q''_{cond}. \tag{4.3}$$

Radiation losses (Q_{rad}) are computed from:

$$Q_{rad} = A\varepsilon\sigma \left(T_s^4 - T_{surr}^4 \right) \tag{4.4}$$

where A is the heater area, ε is the average surface emissivity ($\varepsilon \approx 0.25$ for Inconel 600), σ is the Stefan-Boltzmann constant ($\sigma = 5.67 \times 10^{-8}$ W / m^2 K^4), T_s is the average surface temperature, and T_{surr} is the temperature of the surrounding surfaces. For $T_{surr} = T_{amb}$, $Q_{rad} \approx 0.1\ Q_{tot}$ for natural convection, and $Q_{rad} < 0.03\ Q_{tot}$ in all forced convection tests.

Conduction losses (Q_{cond}), are estimated using Fourier's law:

$$Q_{cond} = k_s A \frac{dT}{dy} \tag{4.5}$$

where k_s is the thermal conductivity of the supporting base. The conduction losses are determined by measuring the temperature drop from the surface through the back side of the supporting base. The back side of the heater is insulated using silicone sealant and therefore $k_s = 0.15$ W / m K. The result is that $Q_{cond} \approx 0.5\ Q_{tot}$ for natural convection and $Q_{cond} < 0.1\ Q_{tot}$ for forced convection.

The localized wall temperature under natural convection, $T_{s,nat}(x)$, is determined using second definition of $Nu(x)$ (and substituting in Newton's law of cooling):

$$Nu(x) = \frac{hx}{k_{air}} = \frac{Q''_{conv} x}{\left(T_{s,nat}(x) - T_\infty\right) k_{air}} \tag{4.6}$$

where h is the convection coefficient. The surface temperature under natural convection is:

$$T_{s,nat}(x) = \frac{Q''_{conv} x}{Nu(x) k_{air}} + T_{\infty} . \tag{4.7}$$

Substituting $Nu(x)$ from Equation 4.1, Equation 4.7 can be rewritten as:

$$T_{s,nat}(x) = \frac{Q''_{conv}{}^{0.8} x^{0.2}}{\left[\left(\frac{Pr}{(4+9Pr^{0.5}+10Pr)}\right)\left(\frac{g\beta}{\nu^2}\right)\right]^{0.2} k_{air}^{0.8}} + T_{\infty} , \tag{4.8}$$

which can be determined from computation or experimental results.

The temperature distribution determined from Equation 4.8 is shown in Figure 4.2 along with the measured temperature distribution on a flat plate. The computed distribution includes radiation and conduction losses based on measurements. The measured temperatures at the leading and trailing edges are approximately 17% higher than predicted while the center temperature is 15% lower. The discrepancy is attributed to the correlation's assumption of an infinitely wide plate, as well as the assumption that radiation and conduction losses are equal across the entire surface. The elevated end plate temperatures can be attributed to the contact resistance between the foil and the Teflon base being neglected.

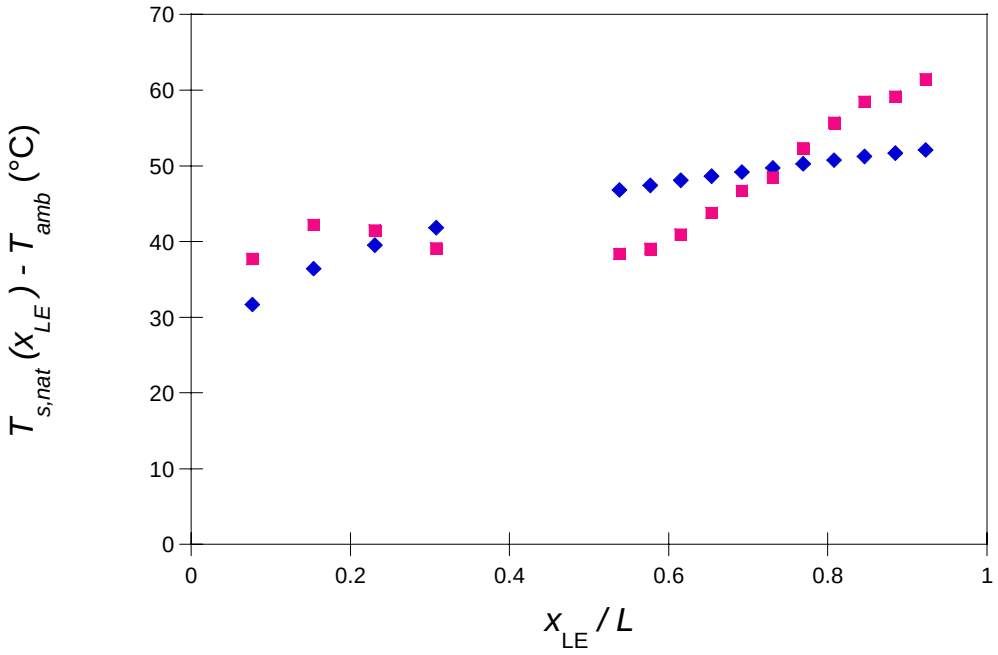

Figure 4.2: Correlation-based temperature distribution of flat plate heater under natural convection (◆) compared to measured values (■).The lack of temperature values between x / L = 0.3 - 0.5 is due to broken thermocouples in this region.

The effect of the reed on localized convection heat transfer is measured in the absence and presence of steady, pressure driven flow as shown schematically in Figure 4.3. The three flow conditions are reed-induced flow, steady flow, and reed-augmented flow. The hardware used for introducing the steady flow is described in §3.7 (the reed is always present even when it is not actuated). Note that when the reed is actuated in the presence of the pressure-driven flow, the flow rate through the channel is kept invariant.

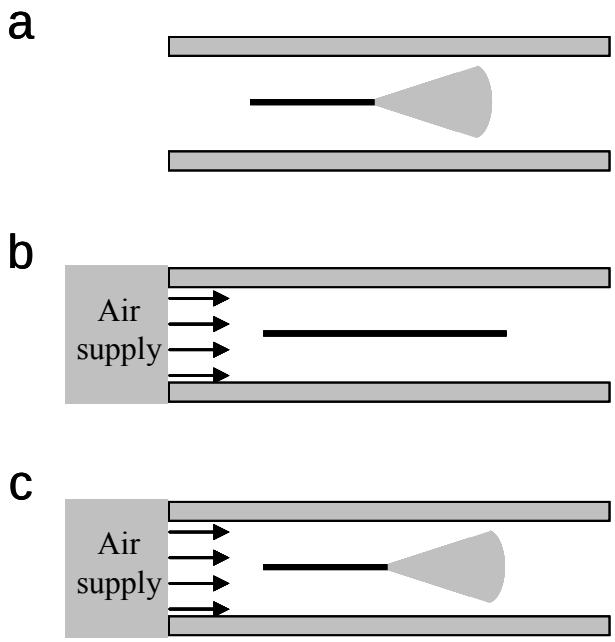

Figure 4.3: Channel-reed configurations for reed-induced (a), steady (b), and reed-augmented (c) flows

4.2. Reed-Induced Flow

As expected, based on the discussion in §3.1, for the reed-induced flow the reed deflection has a critical effect on thermal performance. The thermal resistance along the length of the channel for reed-induced flow is shown in Figure 4.4 for several $A_{p\text{-}p}$. The thermal resistance,

$$\Theta = \frac{T_s - T_\infty}{Q_{conv}} \tag{4.9}$$

is normalized by the local natural convection resistance, Θ_{nat}, measured in the same channel, as shown in Figure 4.5. As the air moves from far upstream of the tip of the

reed, the thermal resistance decreases and reaches a shallow minimum just downstream of the tip near $x / h_o = 0.83$ (e.g. $\Theta = 0.45\ \Theta_{nat}$ for $A_{p\text{-}p} / h_o = 0.75$). This is the same location where the flow separates from the wall, as discussed in §3.1. The thermal resistance decreases with increasing $A_{p\text{-}p}$, which is expected because of the increase in induced small scale motions. As $A_{p\text{-}p}$ decreases, the location of minimum Θ moves slightly upstream (e.g. $x / h_o = 0.42$ for $A_{p\text{-}p} / h_o = 0.24$), where the effect of the induced vortices is more pronounced. It is remarkable that the variations in Θ along the channel (within the present range) are relatively small and that the streamwise rate of change (past the minimum) is small (0.028 for $A_{p\text{-}p} / h_o = 0.75$ from $1.25 \leq x / h_o \leq 2.5$)

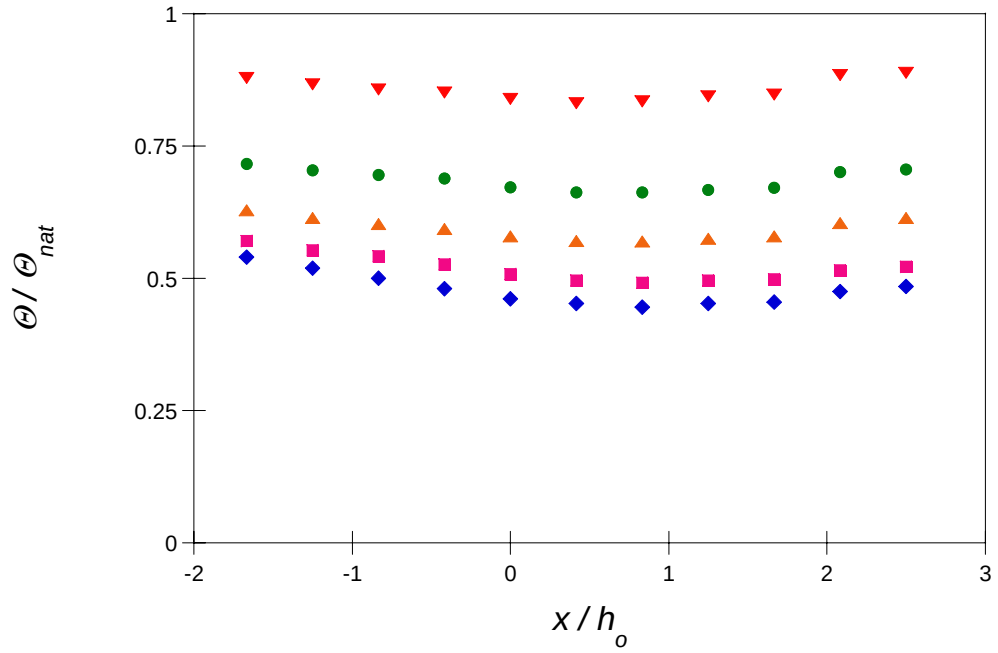

Figure 4.4: Streamwise distribution of normalized thermal resistance for reed-induced flow for $A_{p\text{-}p} / h_o$ = 0.75 (◆), 0.65 (■), 0.45 (▲), 0.35 (●), and 0.24 (▼) (f_{res} = 88 Hz)

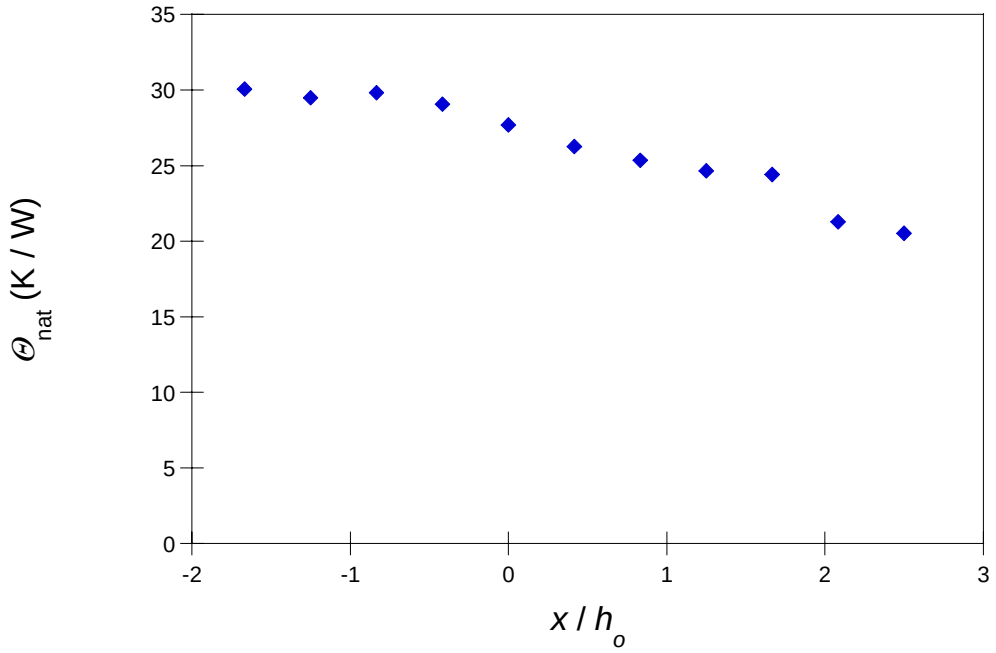

Figure 4.5: Streamwise distribution of natural convection thermal resistance

The localized Nusselt number $\left(Nu_{D_h}\right)$, based on the hydraulic diameter, is defined by:

$$Nu_{D_h} = \frac{hD_h}{k_{air}} = \frac{Q''_{conv} D_h}{\left(T_s - T_\infty\right) k_{air}} \tag{4.10}$$

where D_h, the hydraulic diameter, is defined by:

$$D_h = \frac{4h_o w}{2\left(h_o + w\right)} \tag{4.11}$$

and D_h = 12.0 mm for all experiments presented. The variation in Nusselt number along the length of the channel for several $A_{p\text{-}p}$ is shown in Figure 4.6. For all $A_{p\text{-}p}$,

Nu_{D_h} increases for $-1.7 \leq x / h_o \leq 0.83$, and then begins to saturate for $0.83 < x / h_o \leq 1.7$. This saturation can be attributed to reduction in KE_f for $x / h_o > 1$, as shown in Figure 3.14, or the increase in temperature of the core flow. The increase in Nu_{D_h} for $x > 1.7$ is likely due to conduction end effects of the channel or entrainment of cool air from the ambient, as shown in Figure 3.8. For $A_{p\text{-}p} / h_o = 0.75$, Nu_{D_h} increases by 28% from the reed tip to the exit, achieving a maximum of 19.1. Because Nu_{D_h} is calculated using the channel inlet air temperature (Equation 4.10) instead of the localized air temperature, and the air temperature actually increases in the streamwise direction, the true local Nu_{D_h} number is slightly higher. For large Q, this adjustment is diminished since the air does not have as much time to heat up.

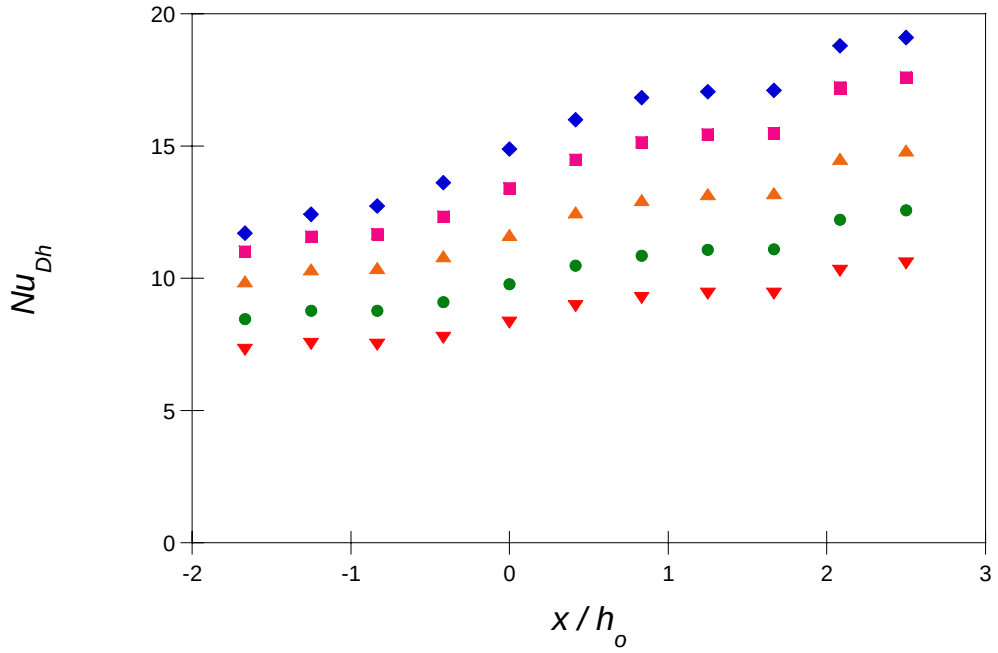

Figure 4.6: Streamwise variation of local Nu_{D_h} in reed-induced flow for $A_{p\text{-}p} / h_o = 0.75$ (◆), 0.65 (■), 0.45 (▲), 0.35 (●), and 0.24 (▼) (f_{res} = 88 Hz)

The normalized thermal resistance decreases with increasing $A_{p\text{-}p}$ everywhere along the length of the channel (Figure 4.7). The data in Figure 4.7 shows that there are two separate domains of linear decrease in thermal resistance: $0 < A_{p\text{-}p} / h_o \leq 0.45$ and $0.45 \leq A_{p\text{-}p} / h_o < 0.75$. For $A_{p\text{-}p} / h_o < 0.45$, as $A_{p\text{-}p}$ increases the reduction in Θ is associated with the increase in Q as well as in the small scale motions induced by the reed. For $A_{p\text{-}p} / h_o > 0.45$, Q begins to saturate, as shown in Figure 3.10, but Θ continues to decrease because the intensity of the small scale motions increases.

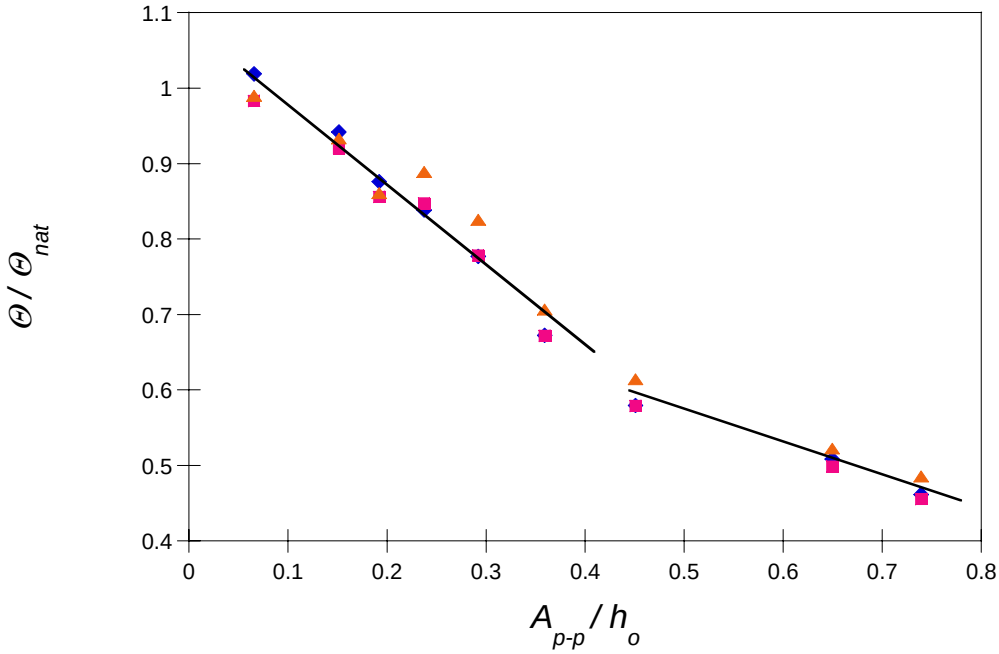

Figure 4.7: Variation of thermal resistance with $A_{p\text{-}p}$ at x / h_o = 0 (◆), 1.25 (■), and 2.50 (▲), (f_{res} = 88 Hz)

As noted in previous sections, the reed-induced flow results in better heat transfer performance than a steady flow at the same Reynolds number. Figure 4.8 compares the thermal resistance at $x / h_o = 0.83$ (where thermal resistance is lowest, as shown in Figure 4.4) for both the reed driven flow and steady, pressure driven flow at various volume

flow rates. The thermal resistance is normalized by the minimum thermal resistance obtained with the reed ($\Theta_{min} = 10.1$ W / m^2 K) at $A_{p\text{-}p} / h_o = 0.75$. The Θ of each flow decreases with increasing Q, and each converges with $\Theta_{nat} = 2.24\ \Theta_{min}$ at $Q = 0$ (natural convection). For any Q, the thermal resistance obtained with the reed is significantly lower than for steady flow

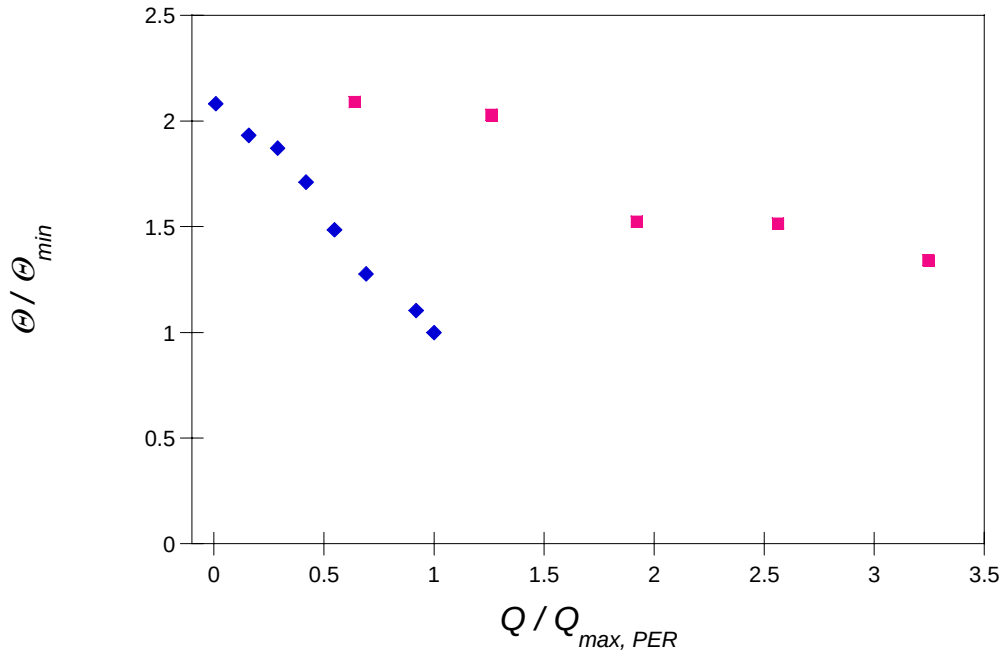

Figure 4.8: Normalized thermal resistance of reed driven flow (◆) and steady flow (■) at various normalized volume flow rates ($x / h_o = 0.83$, $\Theta_{min} = 10.1$ W / m^2 K, $Q_{max,\ PER} = 0.35$ CFM)

4.3. Reed-Augmented Steady Flow

The data presented in §4.2 describe the heat transfer associated with the reed-induced flow. This section focuses on the effect the reed has on an imposed bulk flow through the heated channel, similar to the investigation of §3.7.

Mixing the heated air with the core flow is the primary method for improvement in heat transfer. Figure 4.9 shows the dimensionless temperature of the air across the channel's exit plane for steady and reed-augmented flows at three volume flow rates (Q_{st} = 0.35, 0.71, 1.06 CFM). The heater is along the bottom surface, y / h_o = -0.5. Note that the Q_{st} = 0.35 CFM is in the range of the flow induced by the reed alone. The temperature is measured by traversing a thermocouple probe across the exit plane, measuring a grid of 11 (cross stream) by 10 (spanwise) positions. The dimensionless temperature, Θ' is taken to be:

$$\Theta' = \frac{\left(T_{air} - T_{\infty}\right) k_{air}}{Q''_{conv} D_h} . \tag{4.12}$$

A comparison of the steady flow to the reed-augmented flow at constant Q_{st}, shows that the reed significantly increases mixing across the height of the channel. In both flows, the highest air temperatures are near the heated surface (y / h_o = -0.5), but the temperature distribution within the steady flow is highly stratified across the height, whereas the air temperature in the reed-augmented flow shows far less spatial variation at the exit. This trend holds for the three volume flow rates shown in Figure 4.9. In the steady flow the temperature has little spanwise variation, whereas the reed-augmented flow has a temperature minimum temperature at w = 0 where the effects of the reed have a local maximum. The spanwise asymmetry in the temperature is the result of a nearly-linear spanwise variation in temperature across the heated surface (about 8^{o}C for Q_{tot} = 7.5 W). As a result, the highest air temperature occurs at z / w_o = 0.5.

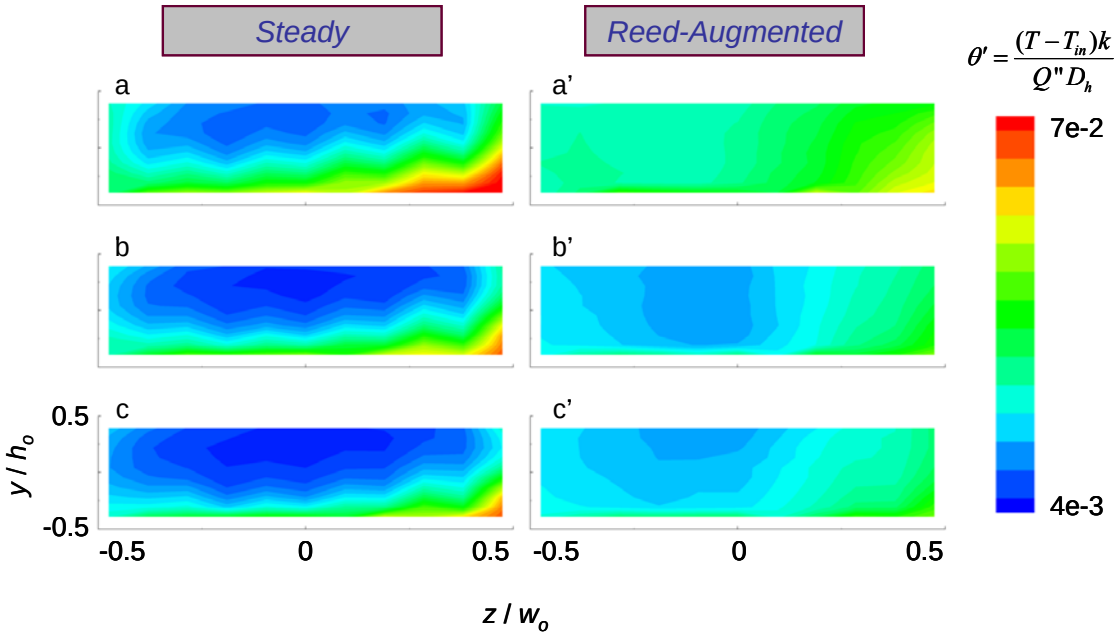

Figure 4.9: Distributions of spanwise temperatures at channel exit for steady flow and reed-augmented flow. Q_{st} = 0.35 (a), 0.71 (b), and 1.06 CFM (c) (Heater at y / h_o = -0.5, f_{res} = 86 Hz)

The average temperature rise, $\Delta T_{rise,avg} = (T_{exit} - T_{\infty})_{avg}$, of the air along the centerline is higher for the reed-augmented flow for all Q_{st}, as shown in Figure 4.10. As the velocity increases, $\Delta T_{rise,avg}$ decreases logarithmically with the difference in $\Delta T_{rise,avg}$ of steady and reed-augmented flows diminishing, indicating that for high Q_{st} the reed's effect also diminishes. The temperatures rise drops by nearly 50% when the flow rate is tripled to Q_{st} = 1.06 CFM for the steady and reed-augmented flows. Figure 4.11 shows the cross stream air temperature along the centerline at the exit plane. It is noteworthy that the temperature in the reed-augmented flow is nearly uniform across the height and has a strong gradient near the surface, whereas the temperature gradient in the steady flow is smaller across the height. This is indicative of the reed's increase in mixing across the channel height. At Q_{st} = 1.07 CFM, the temperature gradients between y / h_o = 0.10 - 0.19

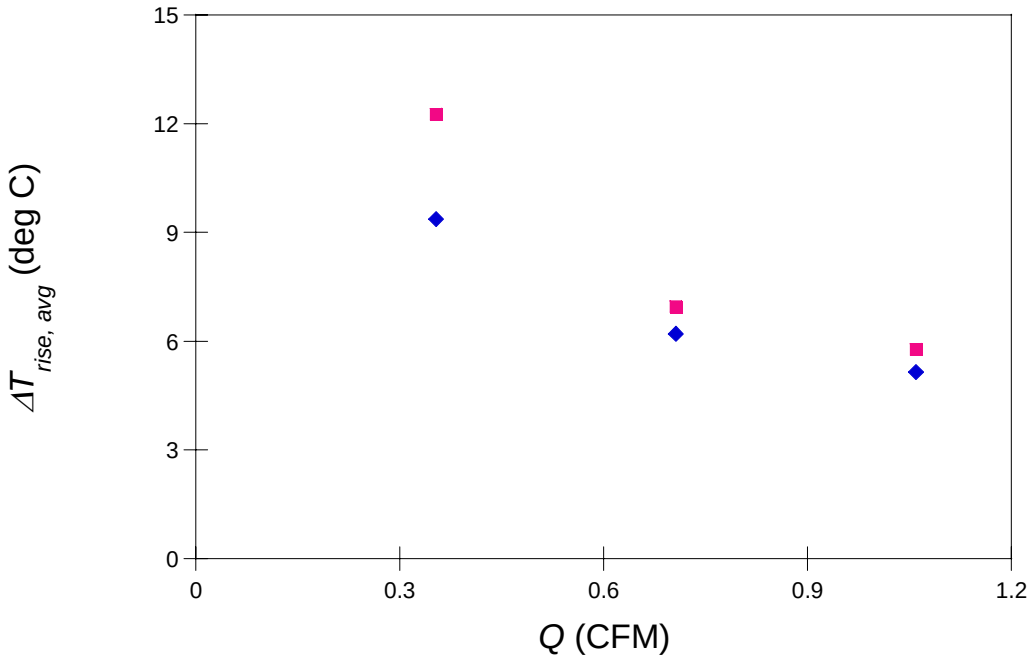

Figure 4.10: Average centerline exit temperature rise for steady (◆) and reed-augmented (■) flows

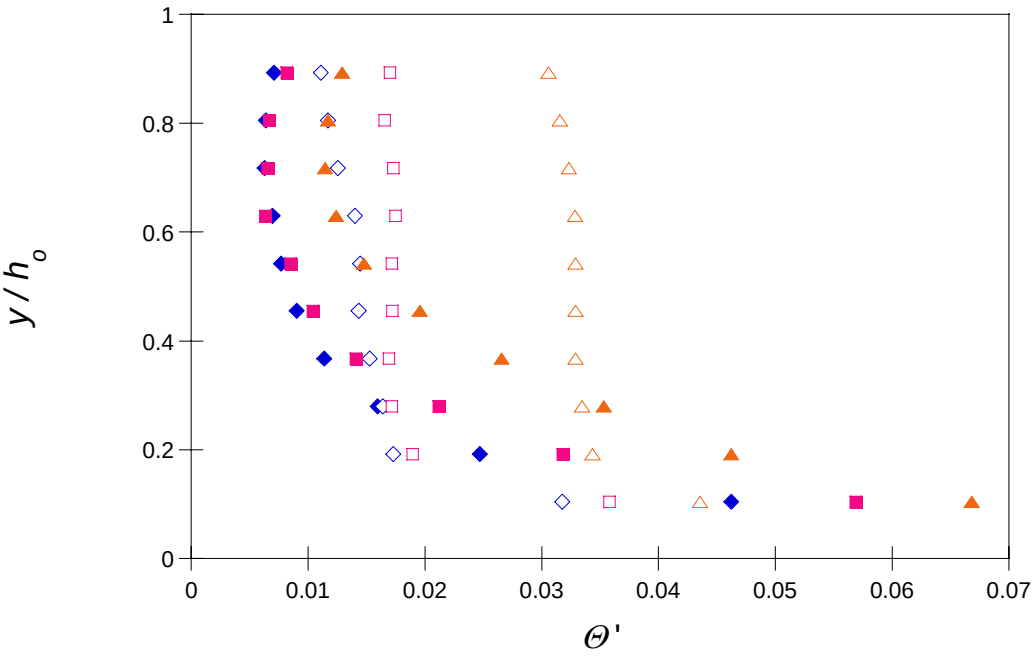

Figure 4.11: Cross stream temperature distribution at exit plane for steady (closed symbols) and reed-augmented (open symbols) flows for Q_{st} = 1.07 (◆), 0.64 (■), and 0.21 CFM (▲)

are -0.25 and -0.17 for the steady and reed-augmented flow, respectively. Also, for identical Q_{st}, the temperature near the wall is higher for the steady flow.

A comparison of the planar temperature profile for the steady and reed-augmented flows at $x / h_o = 0$, 0.83, 1.67, 2.5 and 3.33, are shown in Figure 4.12 for $Q_{st} = 1.06$ CFM. At $x = 0$, both flow conditions result in a highly stratified air distribution because the airflow above the reed, $y / h_o > 0$, is unheated. For the reed-augmented flow, little mixing has occurred yet. Farther downstream, the spanwise temperature distribution in the reed-augmented flow is more uniform due to mixing, whereas the temperature distribution in the steady flow remains stratified. For all x / h_o, the local temperature of the reed-augmented flow is higher than the steady flow indicating more heat being removed from the heated surface.

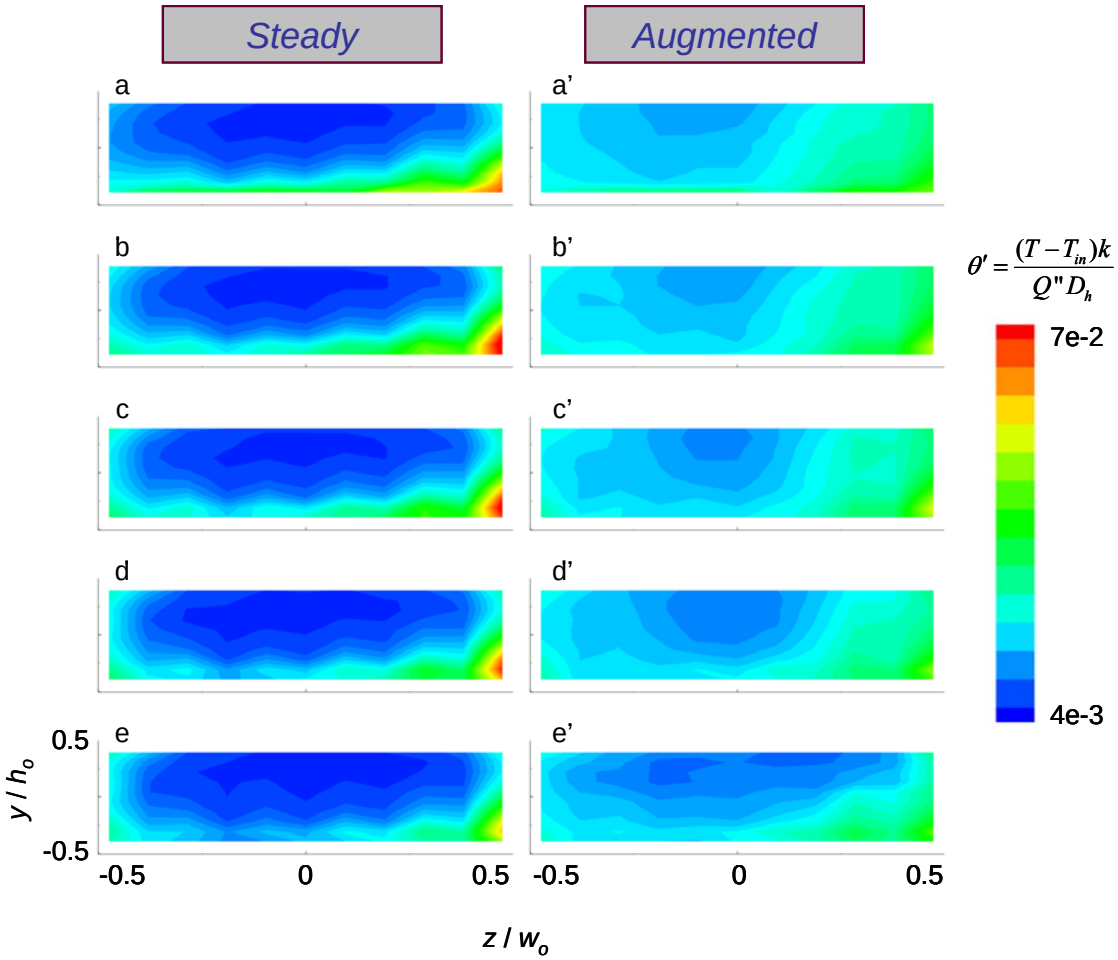

Figure 4.12: Spanwise temperature distribution for steady and reed-augmented flows at x / h_o = 3.33 (a), 2.5 (b), 1.67 (c), 0.83 (d), and 0 (e) (Q_{st} = 1.06 CFM, heater at y / h_o = -0.5)

Streamwise distribution of the cross stream air temperature distributions at the channel centerline ($w = 0$) are shown in Figure 4.13. For the steady flow, the thermal boundary layer is evident along the heated surface as it slowly expands with downstream distance. The temperature fluctuations are contained within a small region near the heated surface ($y / h_o < -0.2$ at exit) and the core flow temperature remains almost invariant. In the reed-augmented flow, this thermal boundary layer is not evident. The lowest temperature occurs at the reed tip near the top wall (because of the unheated air coming from above the reed), but it mixes quickly downstream with the heated air resulting in nearly-uniform

temperature at the exit plane. Figure 4.14 and Figure 4.15 show the differences in cross stream temperature between the steady and reed-augmented flows, respectively. Comparing the two figures it is apparent that the cross stream temperature varies less in the reed-augmented flow (at any x location), along with an overall higher core temperature. Also, the air temperature near the surface is reduced substantially, increasing the local gradient and therefore the heat transfer coefficient. For the reed-augmented flow, the temperature rise between streamwise stations increases steadily for $x / h_o \leq 1.67$, but for $1.67 \leq x / h_o \leq 2.50$ there is a much larger increase. It is conjectured that the majority of mixing occurs within this domain. Although not shown, for lower volume flow rates, this sudden temperature increase occurs farther upstream implying that an increase in the air velocity leads to complete mixing farther downstream. These changes are commensurate with the observations that an increase in Q_{st} results in vortex formation farther downstream along with a maximum in KE_f (see §3.7).

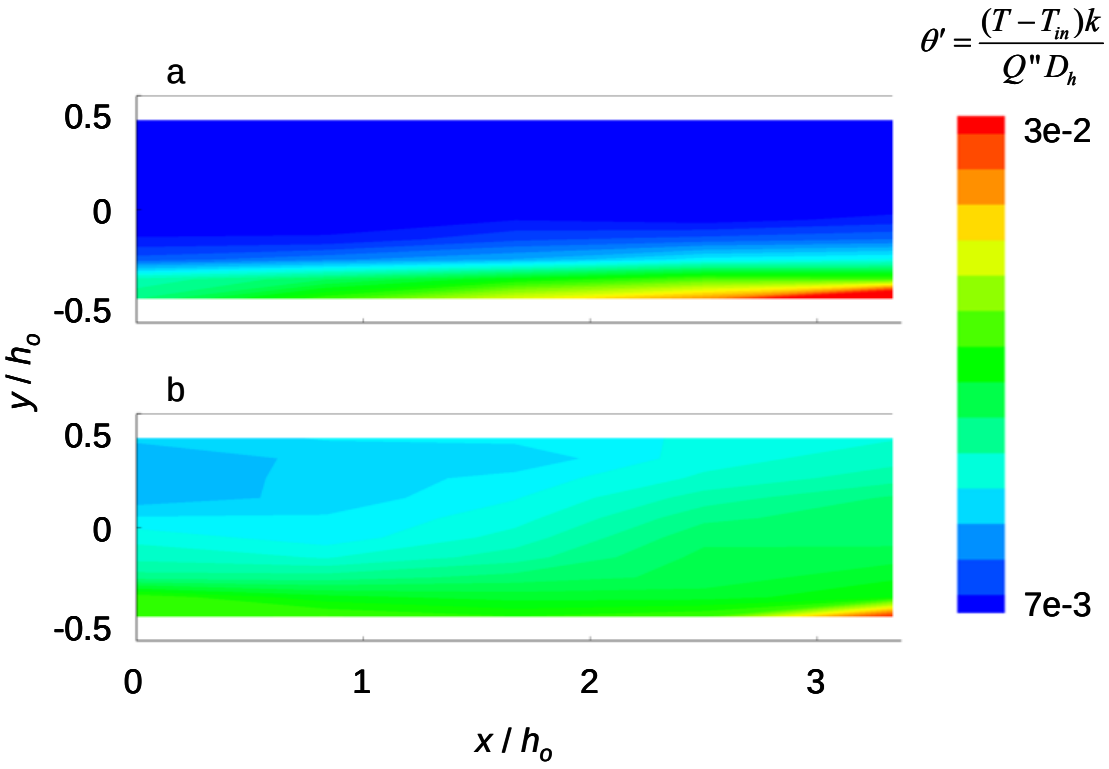

Figure 4.13: Streamwise temperature variation along centerline, $w = 0$, for steady (a) and reed-augmented (b) flows (Q_{st} = 1.06 CFM, heater at y / h_o = -0.5)

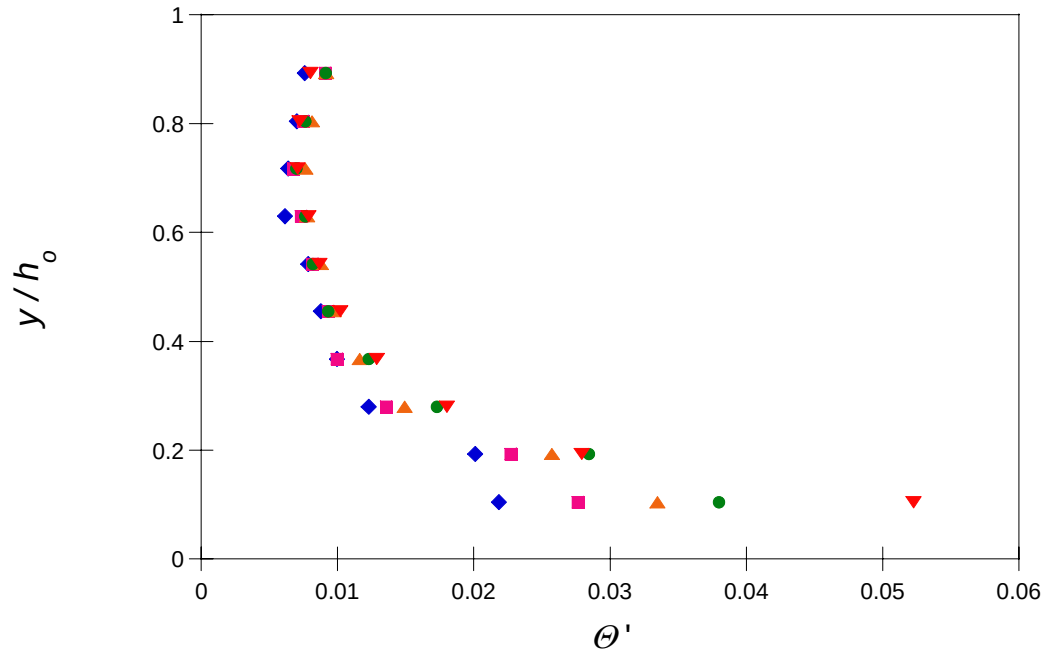

Figure 4.14: Cross stream temperature distributions for steady flow at x / h_o = 0 (◆), 0.83 (■), 1.67 (▲), 2.50 (●), and 3.33 (▼) (Q_{st} = 1.06 CFM)

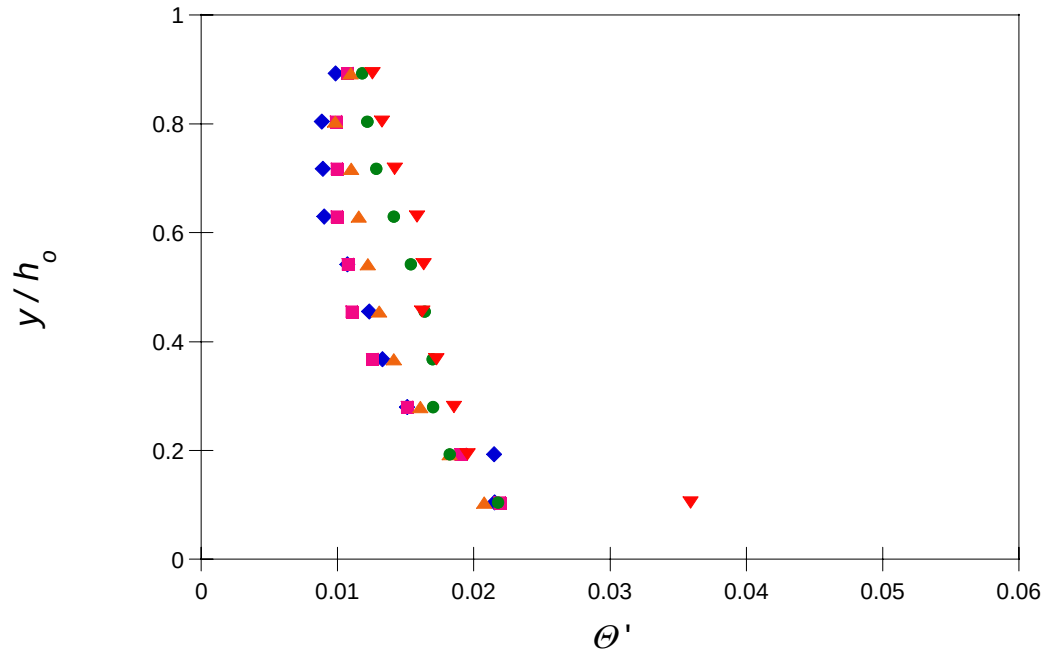

Figure 4.15: Cross stream temperature distributions for reed-augmented flow at $x / h_o = 0$ (◆), 0.83 (■), 1.67 (▲), 2.50 (●), and 3.33 (▼) (Q_{st} = 1.06 CFM)

The streamwise distribution of wall thermal resistance, for both the steady and reed-augmented flows, is shown in Figure 4.16 for $Q_{st} = 0.21$, 0.64, and 1.07 CFM. As expected, for steady flow Θ increases with x due to the increased thermal boundary layer. In the reed-augmented flow this boundary layer is disrupted by the reed induced vortices, resulting in a much lower Θ. At the channel exit, the decrease in thermal resistance from steady to reed-augmented flow is 26%, 34%, and 43% for $Q_{st} = 0.21$, 0.64, and 1.07 CFM, respectively. For the reed-augmented flow, the thermal resistance is minimized at $x / h_o \approx 1.5$, then begins to slowly rise. Once again, this indicates that the maximum improvement in the heat transfer occurs in the region where the flow separates from the wall as seen in Figure 3.1.

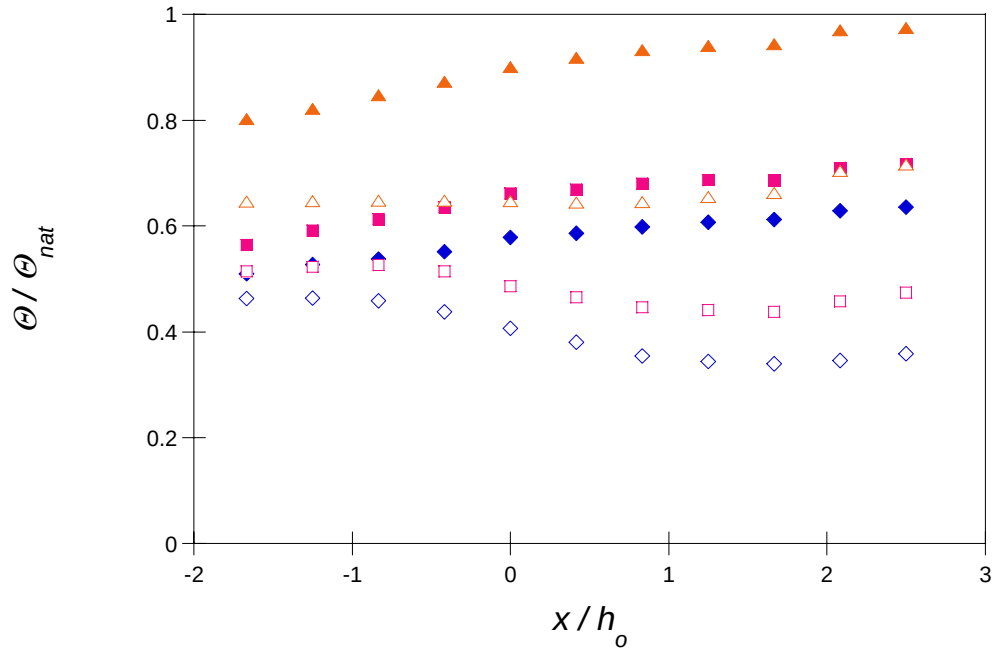

Figure 4.16: Streamwise distribution of thermal resistance at the wall for steady (closed symbols) and reed-augmented (open symbols) flows for Q_{st} = 1.07 (◆), 0.64 (■), and 0.21 CFM (▲) ($A_{p\text{-}p}$ / h_o = 0.53)

The local heat transfer coefficient and Nu_{D_h} at the wall is shown in Figure 4.17 for the same parameters as the previous figure. For all Q_{st}, h increases substantially when the reed is activated. For Q_{st} = 1.07 CFM, h is nearly doubled at the exit plane for the reed-augmented flow (71 vs. 39 W / m^2 K). Also, h increases with increasing Q_{st}. The maximum Nu_{D_h} (28.5) is at the exit for Q_{st} = 1.07 CFM in the reed-augmented flow. It is noteworthy that the Nusselt number at x / h_o = 2.5 for the reed-augmented flow (14.4) is approximately the same for the solely reed-induced flow (Nu_{D_h} = 15.1, as shown in Figure 4.6), at the same $A_{p\text{-}p}$ (0.53 h_o). The slight discrepancy is attributed to the slightly higher flow rate for the reed-induced flow (0.21 vs. 0.27 CFM).

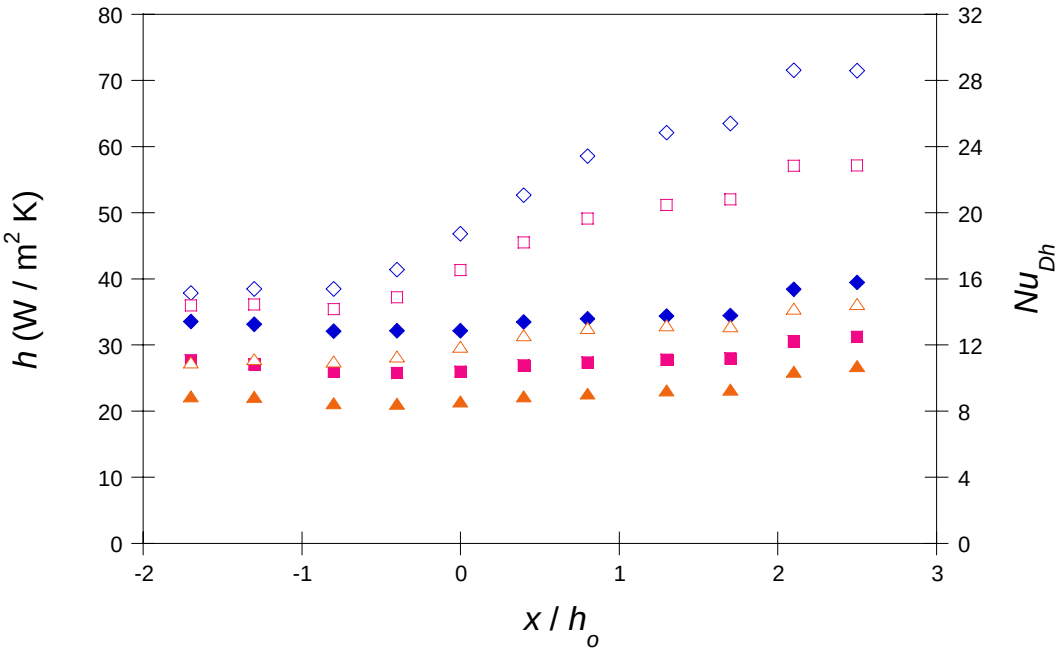

Figure 4.17: Streamwise variation of the convection coefficient and Nu_{D_h} at the wall for steady (closed symbols) and reed-augmented (open symbols) flows for Q_{st} = 1.07 (◆), 0.64 (■), 0.21 CFM (▲) ($A_{p\text{-}p}$ / h_o = 0.53)

It is difficult to compare the Nusselt numbers of the steady flow to earlier investigations because of the flow and heater configurations. Kakaç et. al. (1987) give values of the streamwise variation of Nu_{x^+} for the thermal entrance region of thermally and hydrodynamically developing flow (using the H1 boundary conditions of constant wall heat flux on all the surfaces, axially constant wall heat flux, and circumferentially constant wall temperature). For an aspect ratio of 4, the values of Nu_{x^+} presented by Kakaç et. al. (1987) are compared to the measured values for $Q_{st} = 1.07$ CFM, as shown in Figure 4.18 only for the measured values in the domain $x / h_o > 0$. The dimensionless axial distance from the entrance of the channel is $x^+ = \dfrac{x / D_h}{Re\, Pr}$. The deviation from the literature values are approximately 13%, 17%, and 30% for $Q_{st} = 0.35$, 0.71, and

1.06 CFM, respectively. As Q_{st} is reduced, the measured values approach the results of Kakaç et. al. (1987). The discrepancy is attributed to the difference in the wall heater conditions and the lower channel aspect ratio. As the aspect ratio increases, the values reported by Kakaç et. al. (1987) increase, thus reducing the differences between their results and the present measurements???.

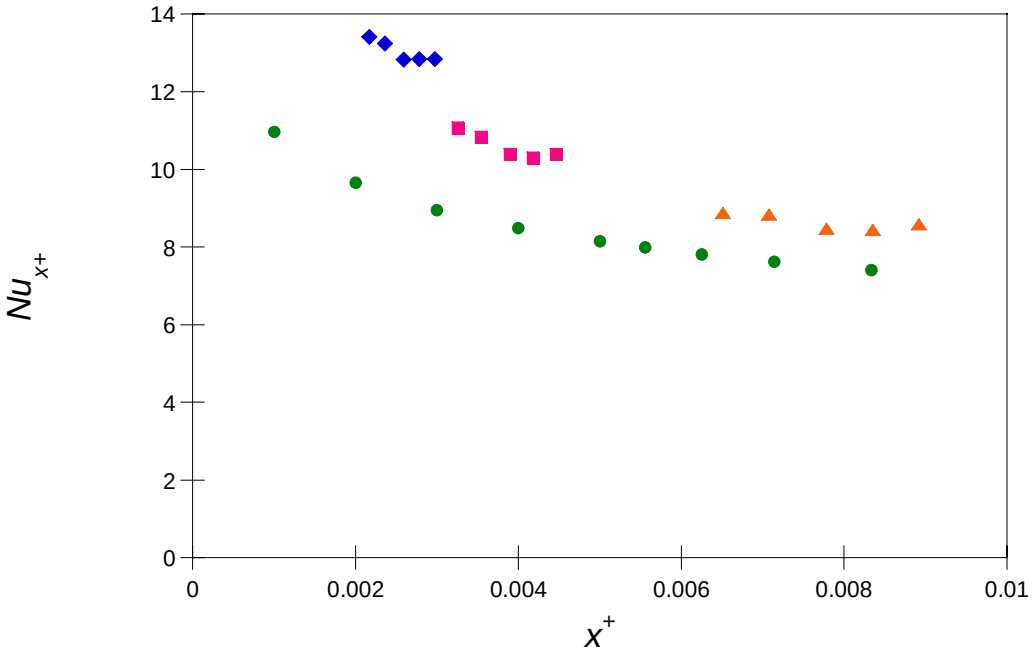

Figure 4.18: Comparison of measured and literature Nu_{x+} for steady flow in the domain of $x / h_o < 0$ for Q_{st} = 1.07 (◆), 0.64 (■), 0.21 CFM (▲) and values reported by Kakaç et. al. (●)

The streamwise variation of the local heat transfer coefficient and Nu_{D_h} for the steady and reed-augmented flows (Q_{st} = 1.65 CFM) is shown in Figure 4.19 for several power inputs, Q_{tot} (the radiation and conduction losses have been accounted for in each Q_{tot}). Comparing the two flows, at Q_{tot} = 7.5 W, the heat transfer coefficient for the reed-augmented flow is slightly higher (3.3 W / m^2 K) at x / h_o = -1.7 due to the unsteadiness associated with the vortex formation (h_{steady} = 58.4 W / m^2 K). As the flow

becomes mixed downstream, the local h decreases by 10% (from tip to exit) for the steady flow (due to the thermal boundary layer), whereas in the reed-augmented flow h increases by 22% (Q_{tot} = 7.5 W, h = 75.5 W / m^2 K). By increasing the power input, h increases linearly by 4.0 W / m^2 K per Watt increase. This increase is due to the convection becoming increasingly dominant over the conduction and radiation losses. Nu_{D_h} and h remain nearly invariant with x for $x / h_o < 0.4$, but then increases farther downstream. The maximum h = 86.0 W / m^2 K and Nu_{D_h} = 34.3 for Q_{tot} = 10.1 W, a 60% increase over that obtained with steady flow. Figure 4.20 shows the reed-augmented heat transfer coefficients normalized by the corresponding local, steady heat transfer coefficient for the same power inputs. At x / h_o = 2.5 the reed-augmented flow h increases by 0.35 h_{steady} for Q_{tot} = 7.5 W from tip to exit, and 0.46 h_{steady} for Q_{tot} = 10.1 W. Near the exit, the temperatures collapse for $Q_{tot} > 8.4$ because the wall temperature, as shown in Figure 4.21 collapse. For steady flow, the wall temperature increases with distance downstream for $x / h_o \leq 0.7$, due to the corresponding increase in the thermal boundary layer. For $x / h_o > 0.7$, the temperature decreases by 5%, likely due to end effects. For the reed-augmented flow at all Q_{tot}, the temperature decreases by approximately 17% from x / h_o = -0.4 to the exit.

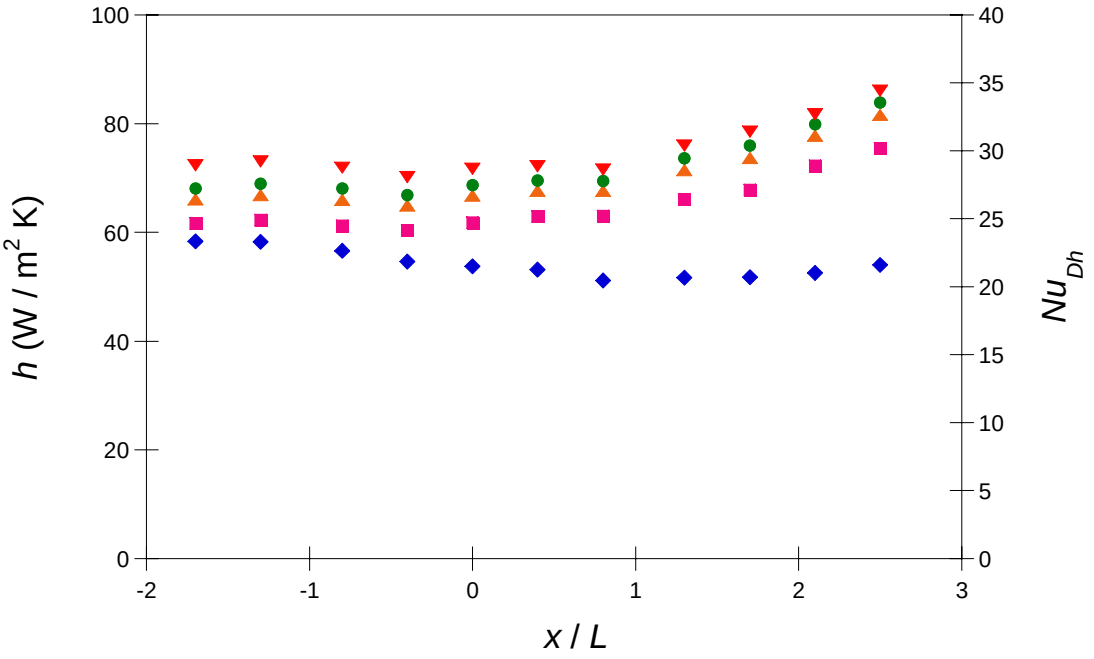

Figure 4.19: Streamwise variation of convection coefficient and Nu_{D_h} for steady flow (Q_{st} = 1.65 CFM) at Q_{tot} = 7.5 W (◆), and reed-augmented flows at Q_{tot} = 7.5 (■), 8.4 (▲), 9.1 (●), and 10.1 W (▼) ($A_{p\text{-}p}$ / h_o = 0.53)

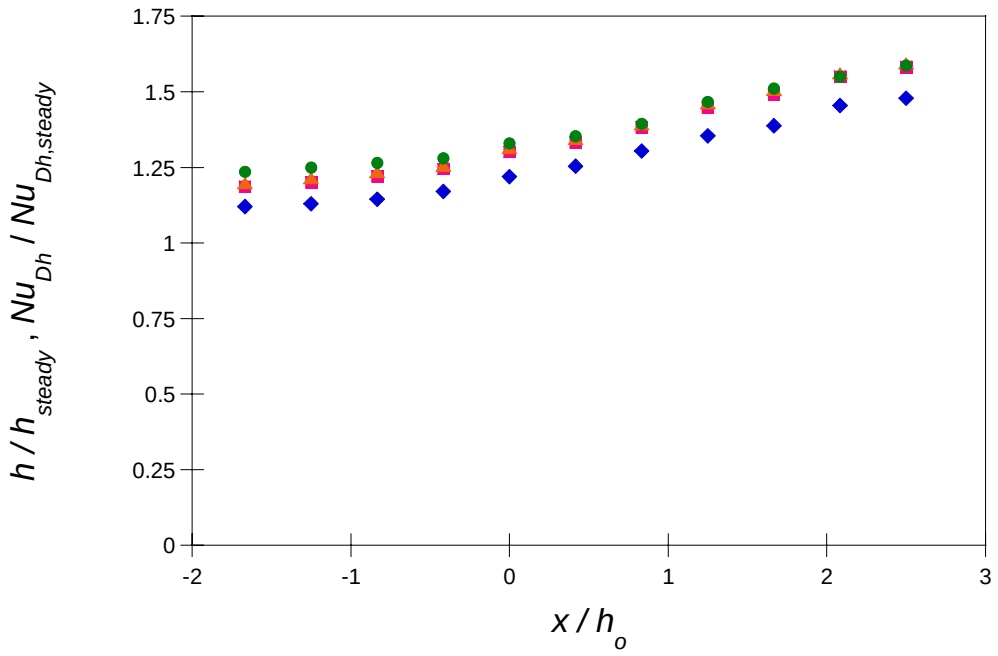

Figure 4.20: Streamwise normalized convection coefficient and Nu_{D_h} for reed-augmented flow (Q_{st} = 1.65 CFM, Q_{tot} = 7.5 W) for Q_{tot} = 7.5 (◆), 8.4 (■), 9.1 (▲), and 10.1 W (●). Local value of h_{steady} is used for normalization. ($A_{p\text{-}p}$ / h_o = 0.53)

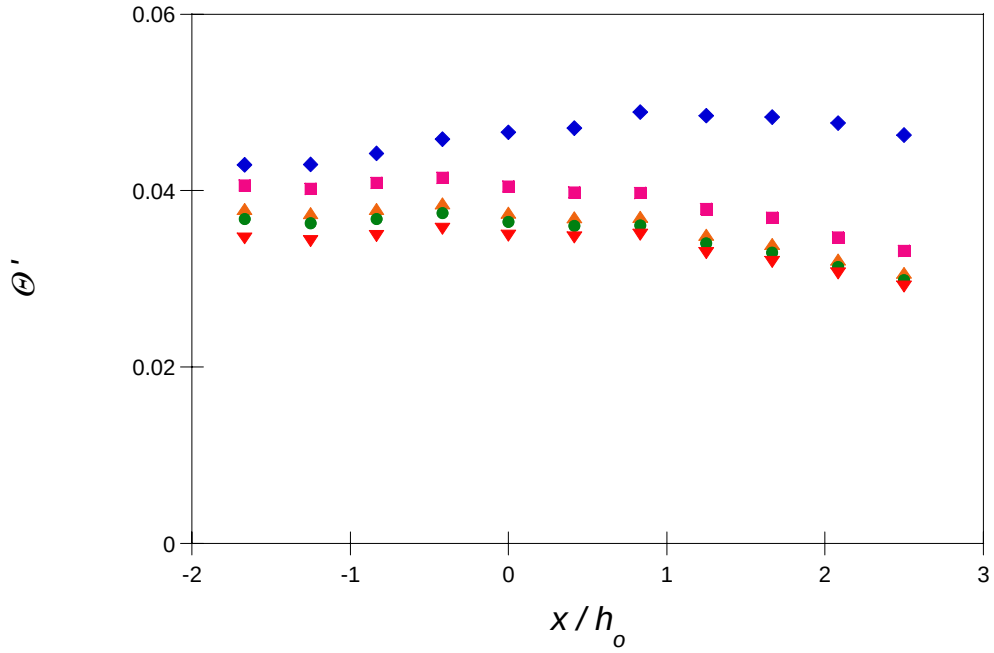

Figure 4.21: Streamwise variation of wall temperature for steady flow (Q_{st} = 1.65 CFM) at Q_{tot} = 7.5 W (◆), and reed-augmented flow at Q_{tot} = 7.5 (■), 8.4 (▲), 9.1 (●), and 10.1 W (▼) ($A_{p\text{-}p}$ / h_o = 0.53)

Chapter 5

Electronics Cooling using an Active Heat Sink

Thermal issues exist over a wide range of power dissipation levels, from handheld devices that dissipate a few Watts to high-performance microprocessors dissipating over 100 W (ITRS, 2001). While cooling requirements at high power levels have resulted in the development of advanced two-phase and pumped liquid cooling techniques, consumer electronic systems still rely on air cooling due to simplicity and relative ease of implementation (Bar-Cohen, 2000). A relatively new challenge in electronics packaging is the cooling of three-dimensional stacked chips due to the increase in volumetric heat generation coupled with the limited heat removal surface area (ITRS, 2001). These devices require effective methods to transfer the heat from the core of the stack to its exterior and ultimate rejection to the ambient.

Air cooling approaches conventionally use fin heat sinks, coupled with a rotary fan, to reject the excess heat to the ambient. This phase of the present work investigates a novel, compact heat sink design in which the rotary fan is replaced with synthetic jet actuators that blow air directly through the base of the heat sink fins. This new approach has several design advantages and achieves a lower thermal resistance compared to conventional designs.

5.1. Brief Review of Synthetic Jet Actuators

Forced convection air cooling is typically based on the use of various configurations of fans and blowers that can fit in medium and large scale enclosures and are used for both local heat transfer augmentation as well as global air circulation. In order to increase power dissipation with fan-heat-sink configurations, designers have typically increased the fan-driven flow rates in addition to increasing the thermal conductivity of the heat sink. Although fans can typically supply ample volume flow rates they can support only relatively low pressure drop and therefore limited flow rates within the fins that reduce their thermal effectiveness.

Synthetic jets offer an attractive solution for highly efficient localized cooling of integrated circuits. These jets are formed by time-periodic, alternate suction and ejection of fluid through an orifice bounding a small cavity that is driven by the time-periodic motion of a diaphragm that is built into one of the walls of the cavity. The jet velocity typically increases with the ratio of diaphragm displaced volume to cavity volume. Unlike conventional jets, synthetic jets are "zero net mass flux" in nature and produce fluid flow with finite momentum with no mass addition to the system and without the need for complex plumbing (Smith and Glezer, 1998). Because of their ability to direct airflow along heated surfaces within confined geometries and induce small-scale motions and mixing, these jets are ideally suited for cooling applications at the package and heat sink levels. While there is extensive literature on cooling with steady and unsteady conventional jets (e.g., Jambunathan et al., 1992), the concept of using synthetic jets for heat transfer is relatively new. It was first implemented by Thompson et al. (1997) who

demonstrated a 250% increase in power dissipation over natural convection over a 49-element MCM using normal impingement cooling with a single synthetic air jet. In a later investigation, Russell et al. (1999) showed that the inherent coupling between a local synthetic jet and global cross flow (driven by a conventional fan) can be exploited for enhanced heat transfer at the package level at substantially reduced global flow rates. A later study (Mahalingam and Glezer, 2005) demonstrated how synthetic jets impinging on a heat sink can increase the heat transfer coefficient by about 2.5 times compared to a steady jet at the same *Re* number.

Recently, Garg et al. (2005) tested the thermal performance of a synthetic jet at normal impingement on a vertically heated surface having a nominal peak velocity of 92 m / s. They achieved a locally maximum heat transfer coefficient of 238 $W / m^2 K$ at U_{max} = 86 m / s. They also determined that the coefficient of performance (COP = heat removed by jet / power consumed by actuator) decreased with increased driving voltage (i.e. higher jet velocity), achieving a COP < 1.

The synthetic jet can be modeled as a Helmholtz resonator. Lasance and Aarts (2008) and Lasance et al. (2008) recently compared measurements of resonant frequency, jet velocity, and driving power with a linear lumped-element acoustic model. While the predicted power was correct, the frequency was over predicted by 15%, and the velocity was over predicted by a factor of three. These shortcomings of the model were attributed to nonlinear losses, which were not accounted for. They also compare heat transfer measurements with those of a fan having an exit area 100 times larger than the jet, and found that the jet outperforms the fan for small heater areas.

5.2. Synthetic Jet Module Design and Testing

As part of the present work, synthetic jet actuators are integrated into a novel heat sink for improved heat transfer in a compact, fan-less design. Earlier versions of synthetic jet cooled heat sinks utilized jet blowing into straight high aspect ratio rectangular channels that are formed between the fins. As shown for example in Figure 5.1a the jet module is placed at one end of the fin channel so that each jet orifice induces air flow along the channel length. Mahalingam and Glezer (2001) used this approach to achieve a thermal resistance of 0.8 K / W in a heat sink measuring $120 \times 70 \times 30$ mm (59.2 W at 70°C), using a total flow rate of about 4.4 CFM. In the present configuration the jets emanate directly through the heat sink base and entrain and expel air across the height of the fins as shown in Figure 5.1b. This jet configuration forms cellular pockets that recirculate air between the fins, with fresh air entrained during one half-cycle of the actuator operation and the heated air expelled laterally during the second half.

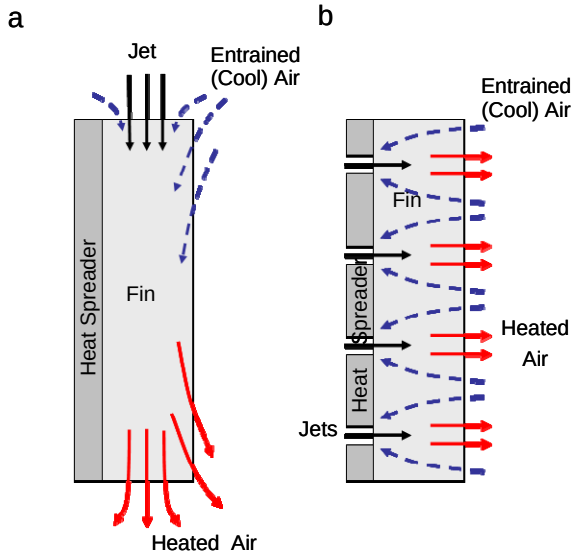

Figure 5.1: Basic principle of operation of a) longitudinal fin flow heat sink and b) cross fin flow heat sink

There are several advantages to inducing air flow across the fins as shown in Figure 5.1b. First, the cooler air moves a shorter distance, and therefore undergoes a lower temperature rise resulting in higher heat transfer coefficient. Second, this configuration enables easier entrainment of cool air where the entrained air is heated during both the suction and ejection strokes of the cycle. Because the cooling air heats up as it moves along the length of the fins, the convective heat transfer coefficient decreases (e.g. Mahalingam and Glezer, 2001). Furthermore, when the jet flow is directed across the fins the jets experience a lower pressure drop and there is no possibility of flow bypass.

5.3. Longitudinal Cooling of Heat Sink Channels

The straight-channel heat sink was briefly tested using a U-shaped design to accommodate the synthetic jet module as shown in Figure 5.5. The U-shape design also minimizes the footprint of the integrated heat sink and actuator. The present heat sink was fabricated from copper and is 50.8 mm wide, 47.6 mm tall and 40.3 mm deep, with overall volume of 97.4 cm^3 (67.6 cm^3 without the volume of the actuator module) as shown in . There are 11 fins on each side where each fin is 0.9 mm thick, 12.7 mm long, and span the entire heat sink height. Foil heaters placed on the bottom surface provide the thermal load.

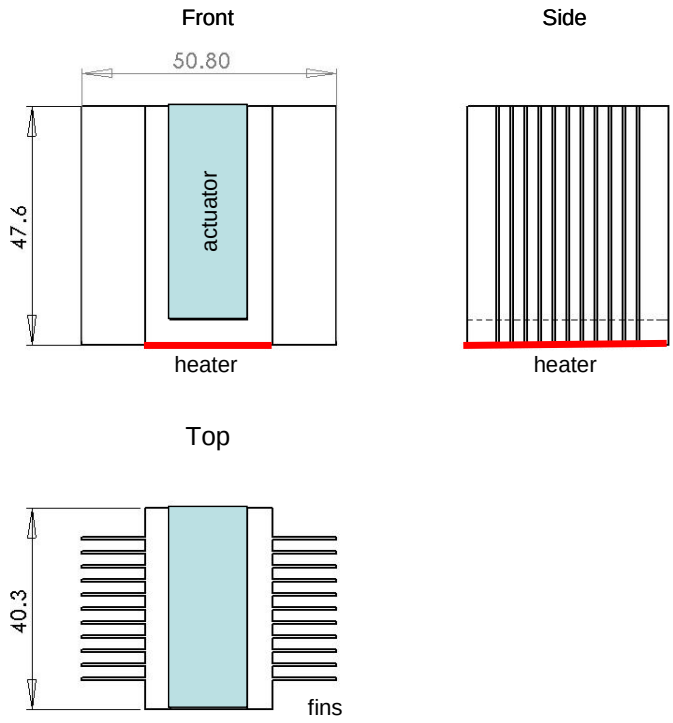

Figure 5.2: Front, side and top views of heat sink with locations of heater and actuator driver shown

The synthetic jets are created by the time-periodic motion of two electromagnetic drivers built into a cavity that is fabricated using stereolithograph material. The cavity design is such that each driver faces a common central chamber and a single chamber as shown schematically in Figure 5.3. Air is ejected and sucked through conduits and nozzles that are placed above the individual channels as shown in Figure 5.4. The electromagnetic actuators were placed in the center of the actuator module (as shown in Figure 5.5) and the air was routed up and out through multiple downward facing nozzles. Each nozzle was centered over a fin with an exit on each side of the fin. The spacing of the nozzles allowed for a small opening above it permitting fresh ambient air to be entrained from above the heat sink.

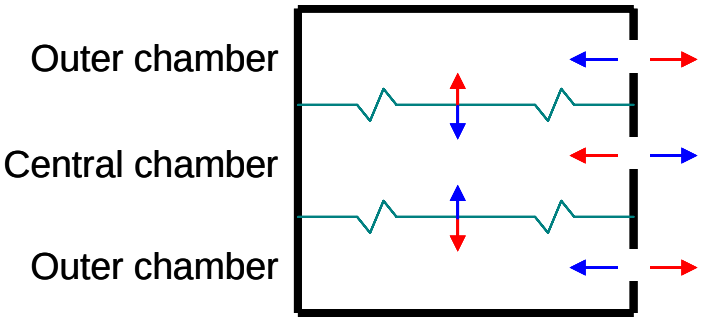

Figure 5.3: Synthetic jet schematic showing the central and outer chambers. Diaphragm motion and corresponding airflow are noted.

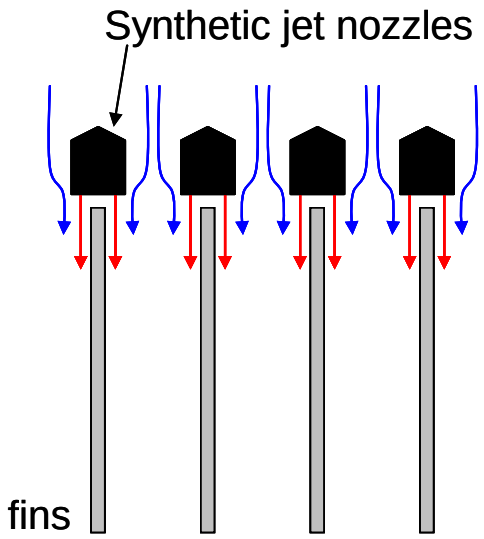

Figure 5.4: Schematic of ejected (—) and entrained (—) airflow between fin channels for longitudinal cooling

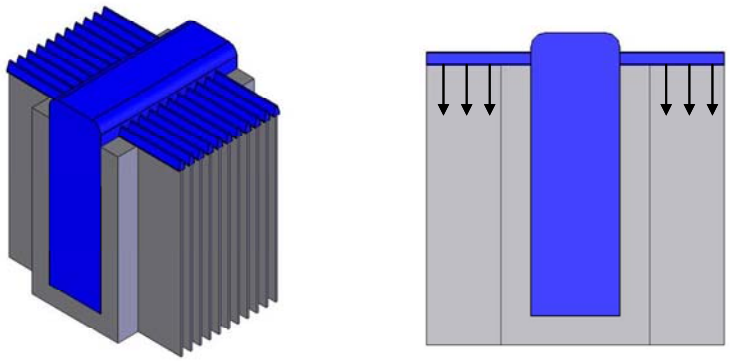

Figure 5.5: Isometric and side views of longitudinally cooled heat sink with actuator module

The time-averaged flow in the vicinity of the straight channel that is formed by two adjacent fins is measured using PIV (Figure 5.6). The data shows that ambient air is drawn between the nozzles near the upper edge of the fins ($y / H > 0.75$). There is also some entrainment through the open (top) end of the channel. However, perhaps the most striking flow feature is the flow bypass along the length of the fins. Much of the air does not progress down the length of the channel, but instead starts exiting the fins at $0.25\,H$ from the jet origin. This flow bypass results in significant cooling inefficiency near the bottom of the heat sink.

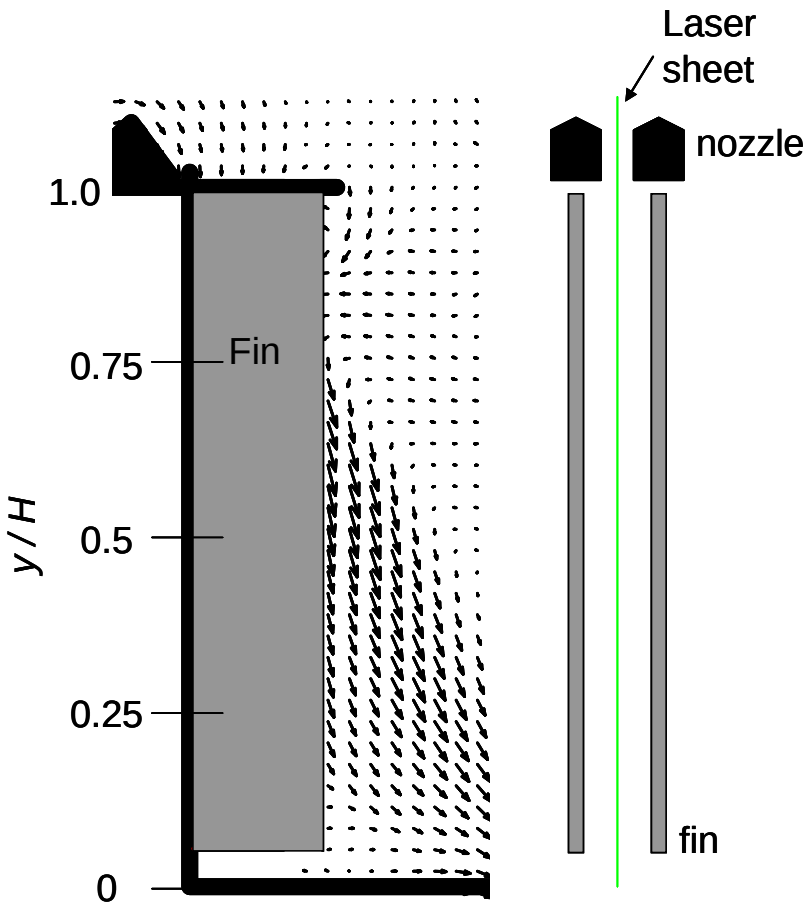

Figure 5.6: Time-averaged velocity field surround the LBHS

It is possible to reduce or even eliminate the flow bypass by modifying the heat sink. This was demonstrated by canting the jets and the top edges of the fins as shown in Figure 5.7. For this test, one fin was removed and replaced with a clear plastic fin allowing PIV access to the flow between the fins. The time-averaged velocity field is shown in Figure 5.8. These data show that while the flow bypass is substantially reduced, there is a separated flow domain near the top half of the (vertical) fin that can result in reduced thermal performance. Of course, canting the jets also reduces the heat transfer area.

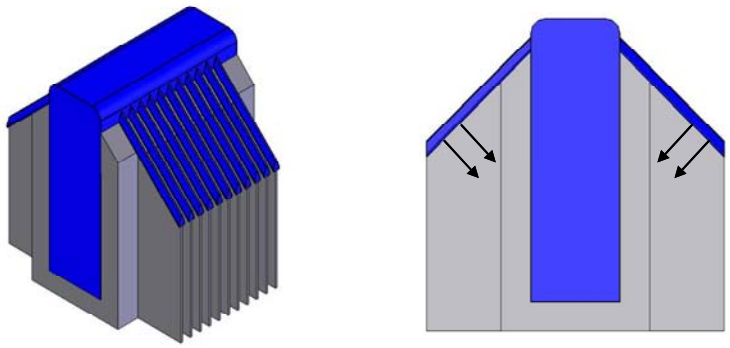

Figure 5.7: Isometric and side views of canted heat sink configuration with actuator module

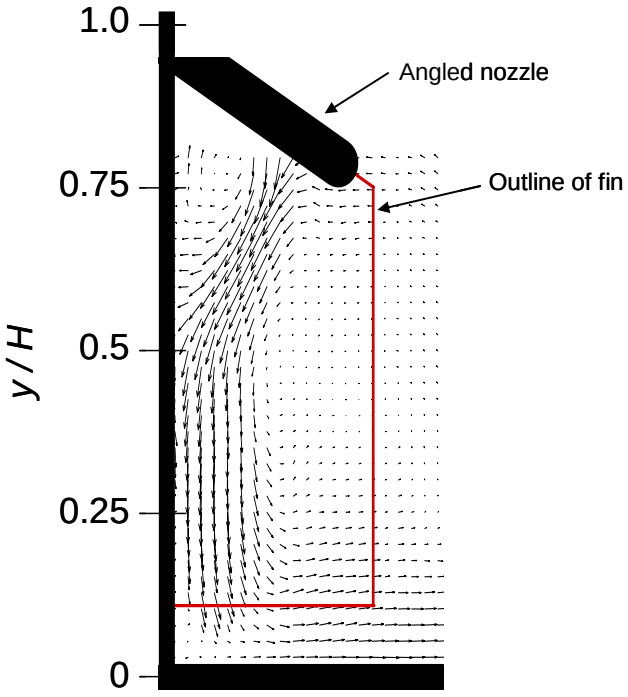

Figure 5.8: Time-averaged velocity field between fins of angled heat sink, with the outline of the fin shown in red

5.4. Cross Fin Flow Heat Sink

The new heat sink was designed to reduce the deficiencies associated with the longitudinal fin flow. Using the same overall dimensions and design of the U-shaped heat sink in Figure 5.5. The heat sink was modified to accommodate cross fin flows as shown in Figure 5.9

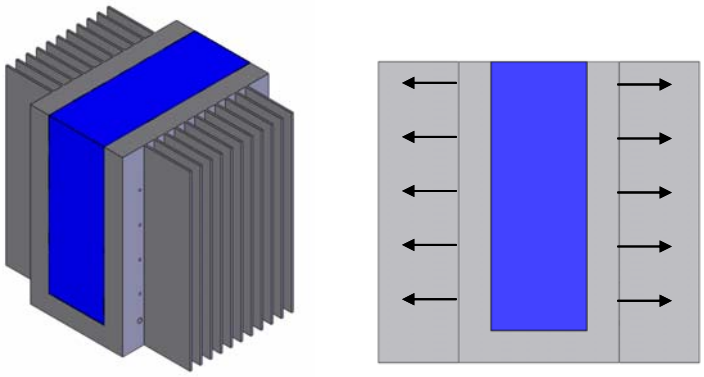

Figure 5.9: Isometric and side views of the cross fin flow configuration with actuator module

As discussed in connection with Figure 5.1 above, this novel concept is based on jet orifices that allow the flow to move directly from the actuator module through the base of the heat sink. The optimal orifice size for maximizing the volume flow rate was determined using SLA models of the heat sink and the flow rate through the fins was measured using PIV. The actuator module was fitted with two electromagnetic drivers as shown in Figure 5.10 (only half of the symmetric module is shown). The actuator module has three cavities that are internally separated by the two electromagnetically-driven diaphragms. Each outer cavity is driven by a single diaphragm while the center cavity is driven by both diaphragms. The phase of the diaphragms is such that the outer cavities

eject air while the center cavity is in the suction cycle. The jet created by each of the two outer cavities can be easily directed between the fins through orifices in the base. The total airflow through the center cavity drives a single jet near the bottom of each fin channel on both sides of the heat sink. The outer actuator cavity (on both sides of the heat sink) drives four jets through each channel. The diameter of these four smaller orifices was optimized by varying the ratio of the total orifice areas driven by the center and outer cavities, A_c / A_o, and measuring the volume flow rate through the fins. These results are shown in §5.5.

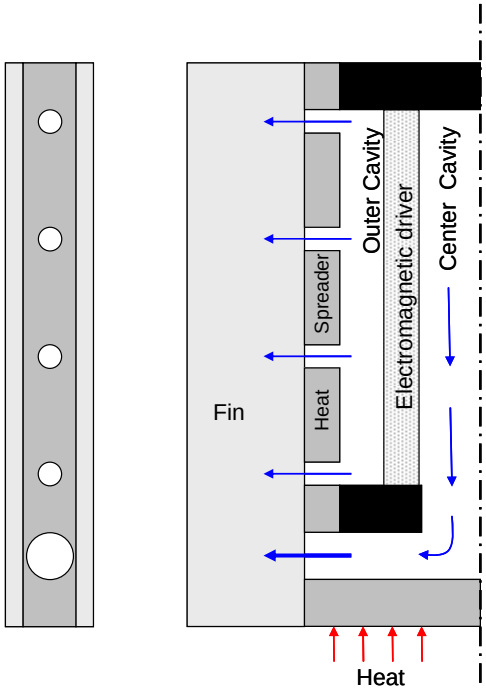

Figure 5.10: Cross-section of the jet actuator showing the outer and center cavities and jet orifices

It is noteworthy that the presence of the orifices do not decrease the thermal performance significantly due to the decrease in conduction path through the base of the heat sink. A one-dimensional conduction analysis showed that the spreading resistance of the base

increases by only 5% by placing these orifices in the base, and this increase is partly compensated for by the increase in cooled surface area created by the orifices; therefore no appreciable increase in thermal resistance is expected.

The temperature of the heat sink base is monitored using T-type thermocouples and the measured temperatures are digitized using a data acquisition system employing cold junction compensation. The measurements have a resolution of 0.1 °C and an accuracy of 0.4 °C. The maximum error for each temperature reading is ±1.5 °C resulting in a maximum error of ±2 - 3% for the temperature range of the present data. The pressure differential is measured using a hook gage with a resolution of 0.06 Pa resulting in an error of ±1 - 8% for the pressures measured. All PIV was measured using the system discussed in §2.3.

5.5. Cross Fin Flow Performance Characterization

The variation of the volume flow rate of the actuator module with orifice area was characterized to maximize the flow rate as shown in Figure 5.11. For these measurements, $A_o = 29.8$ mm^2 and $f_d = 150$ Hz. These data show that the volume flow rate has a maximum at approximately $A_c / A_o = 0.87$ and therefore the corresponding orifice diameter is used for all further testing.

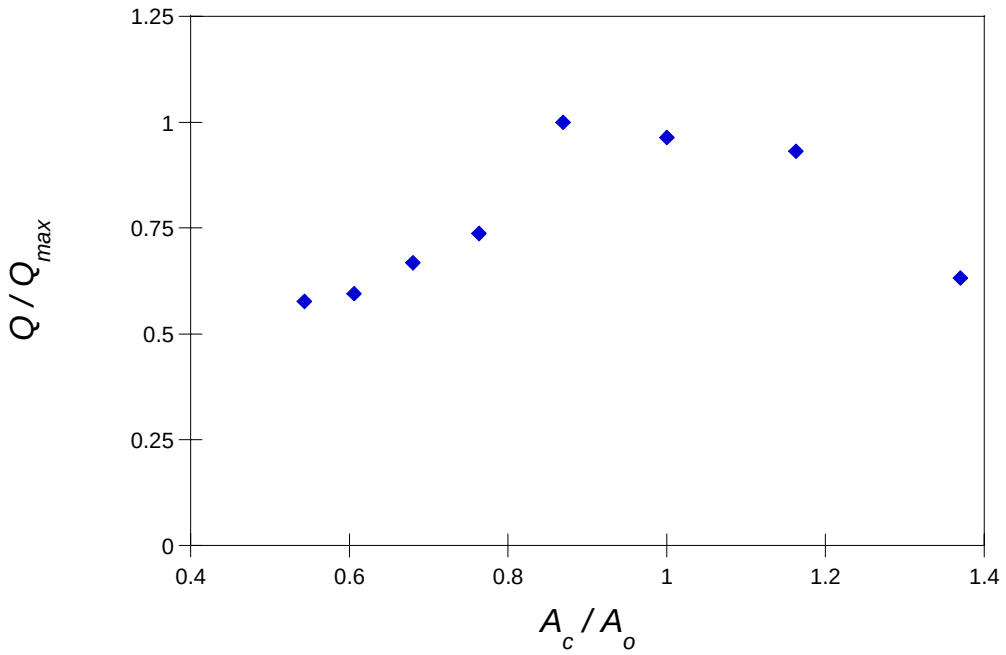

Figure 5.11: Variation of time-averaged volume flow rate through fins with orifice area ratio [f_d = 150 Hz, Q_{max} = 3.92 × 10^{-4} m^3 / s (0.83 CFM)]

Figure 5.12 shows time-averaged distributions of the cross fin velocity component (normal to the base) at the edge of the fins for $A_b / A_f = 0.87$ ($f_d = 150$ Hz). The distribution is characterized by four peaks at $y / H = 0.31$, 0.46, 0.62, and 0.74 (compared to the location of the orifices at $y / H = 0.27$, 0.44, 0.61, and 0.79 ($H = 47.6$ mm). The velocity of the jets exiting near the top of the heat sink is higher (77%) than near the bottom. This variation results from an internal pressure difference between the center and outer cavities (across the diaphragm). To equalize this pressure differential, a vent was placed in the center cavity. The value $A_{c,v}$ includes the center cavity orifice area plus the area of the vent. Flow is entrained into the channel for $y / H < 0.24$ and $y / H > 0.79$. The lower region indicates that the center cavity orifice provides more air entrainment near the bottom of the heat sink than ejection. The variation of the pressure difference across the diaphragm ($P_{c,v} - P_o$) with area ratio is shown in Figure 5.13. For $A_{c,v} / A_p = 1.05$ the

pressure differential becomes zero. Further increasing the vent area causes the pressure in the outer cavity to be greater than in the center cavity. The differential pressure coefficient for increasing driving frequency, f_d, for various vent sizes is shown in Figure 5.14. As f_d increases, C_p increases as f_d^2, and decreases for increasing $A_{c,v} / A_o$.

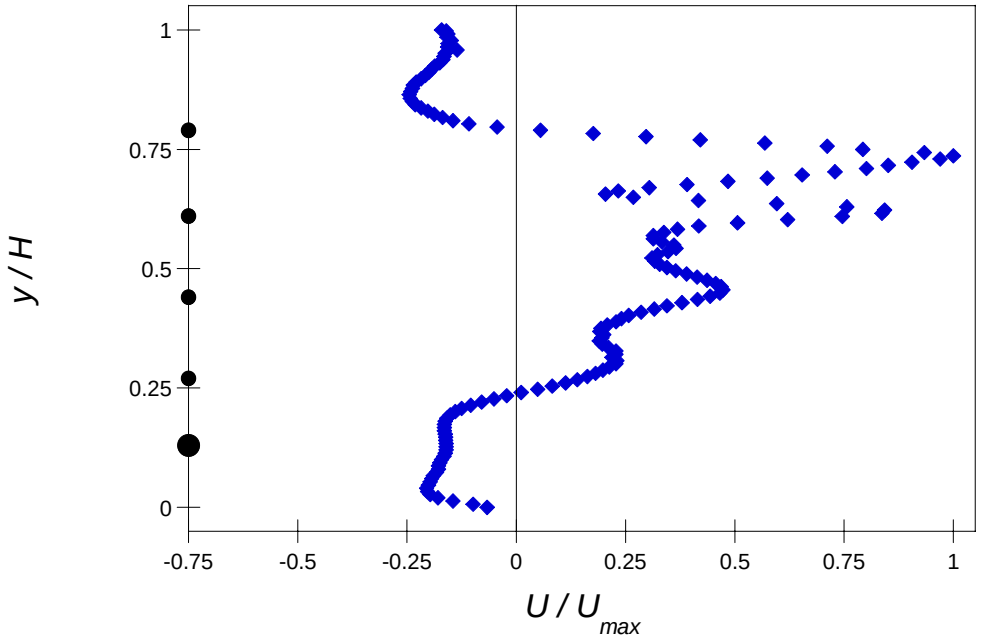

Figure 5.12: Normalized time-averaged streamwise velocity profile at fin tip along height, $C_p \neq 0$, with orifice locations shown (f_d = 150 Hz, U_{max} = 0.76 m / s)

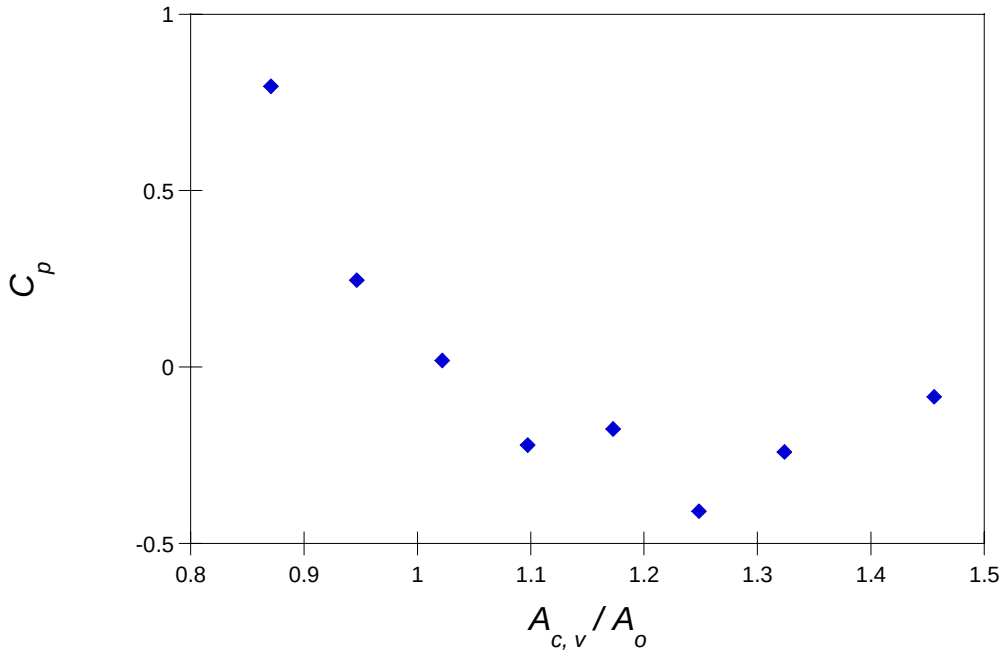

Figure 5.13: Variation of the pressure difference $\left(C_p = \frac{P_{c,v} - P_o}{0.5 \rho U_{\max}^2} \right)$ **between outer and center cavities with (total) orifice exit area ratio (f_d = 150 Hz)**

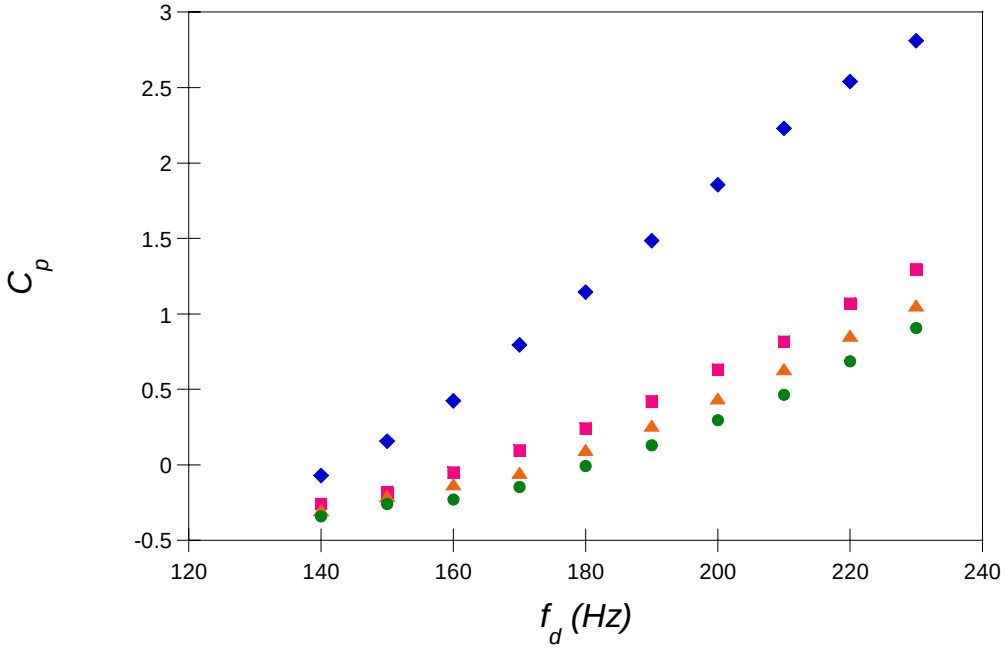

Figure 5.14: Variation of pressure difference with actuator frequency for $A_{c,v} / A_o$ = 0.87 (◆), 0.95 (■), 1.02 (▲), and 1.10 (●)

For each of the area ratios shown in Figure 5.14, the operating frequency $C_p = 0$ is determined (f_d = 143 Hz, 163 Hz, 173 Hz, 180 Hz for $A_{c,v} / A_o$ = 0.87, 0.95, 1.02, and 1.10 respectively). Distributions of the cross stream velocity components are measured when the actuators are operated at the frequency when $C_p = 0$ and are shown in Figure 5.15 (U_{max} = 0.82 m / s) for each area ratio. It is remarkable that balancing the pressure on both sides of the diaphragm leads to reasonably uniform jets. There are four distinct peaks where each of the jets exit through the base. Near the base of the heat sink where the heat load is placed, there is a domain of entrained flow through the fins. The absence of a jet emanating from the bottommost orifice indicates that this orifice works differently in suction and blowing. It is conjectured that this is the result of the vent in the central cavity. The volume flow rate (for half the heat sink) is calculated from the velocity distributions in Figure 5.15 and shown in Figure 5.16 assuming that the velocity exiting the fin is uniform across the fin spacing. Since the synthetic jets are zero net mass flux devices, the overall volume flow rate is zero. Therefore, the volume flow rate of the device is determined by summing only the amount of air exiting the fin channel. The volume flow rate of air is independent of A_o when $C_p = 0$ and Q_{max} = 0.83 CFM.

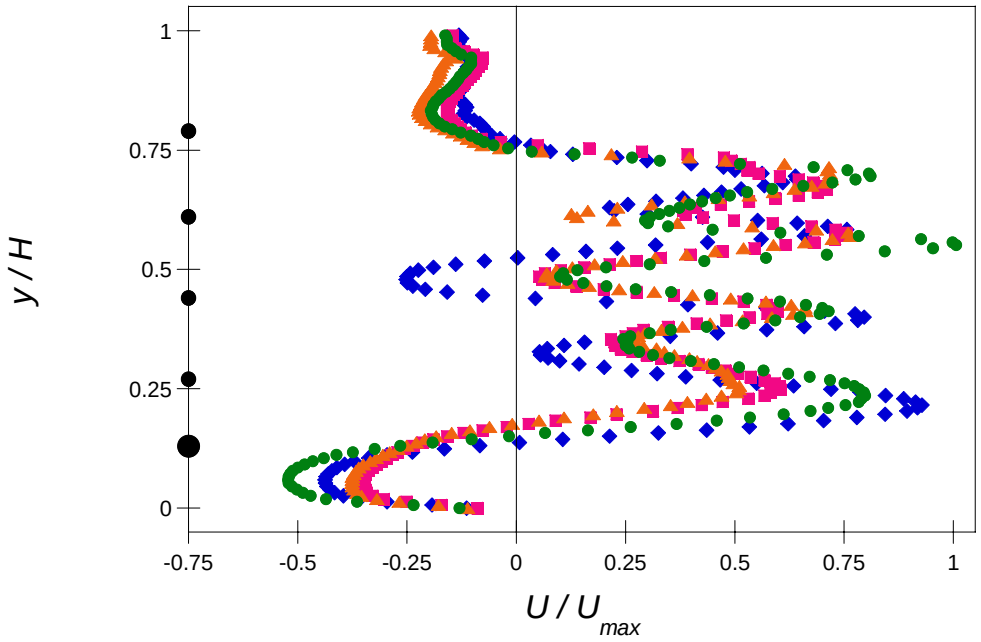

Figure 5.15: Time-averaged streamwise velocity distribution at fin tip for $A_{c,v} / A_o = 0.87$ (◆), 0.95 (■), 1.02 (▲), and 1.10 (●) with orifice locations shown ($C_p = 0$, $U_{max} = 0.82$ m / s)

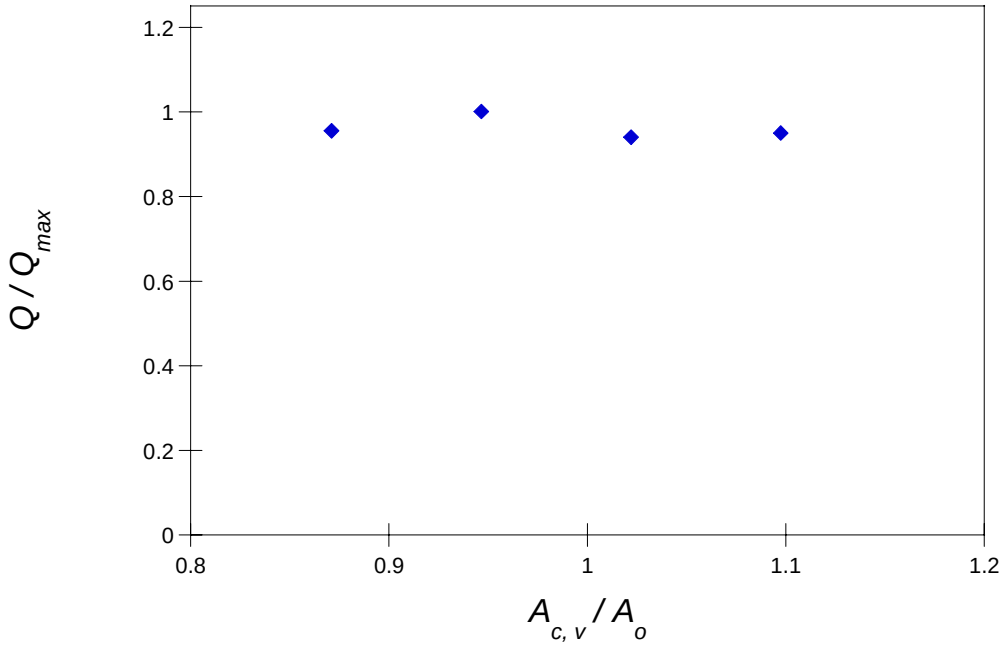

Figure 5.16: Exhaust volume flow rate for $C_p = 0$ ($Q_{max} = 3.92 \times 10^{-4}$ m^3 / s, 0.83 CFM)

As expected, for a given amplitude the induced volume flow rate increases with frequency. Figure 5.17 shows the variation of the time-averaged volume flow rate with actuation frequency for various exit area ratios and the ejected volume per cycle (Q_{max} = 3.82 × 10^{-4} m^3 / s, 0.81 CFM). When $A_{c,v} / A_o$ is increased, the volume flow rate decreases, but the overall ejected volume is nearly invariant, as expected. The reduction in Q results from increased air ejection through the vent reducing the volume of air ejected through the vent in the synthetic jet module. The center cavity entrains more air from between the fins than through the vent, but ejects more out the vent. This means that the orifice for the center cavity is more efficient in suction than in blowing. Although this appears to be inefficient, it actually results in better heat transfer, as will be discussed below.

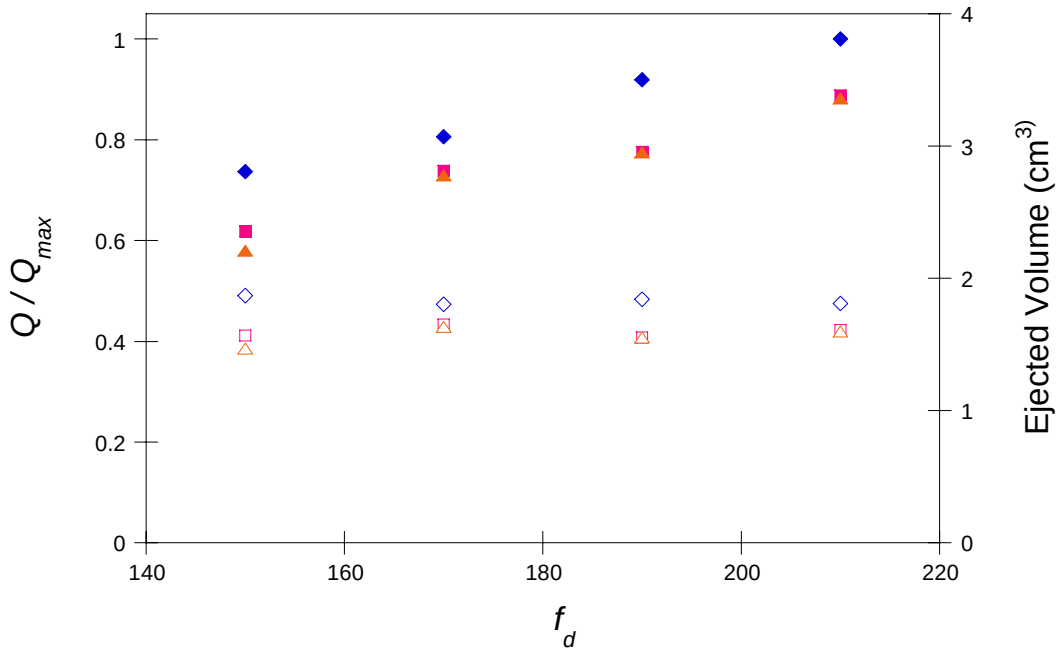

Figure 5.17: Variation of volume flow rate and ejected volume per cycle with actuation frequency for $A_{c,v} / A_o$ = 0.95 (◆), 1.02 (■), and 1.10 (▲), filled symbols – Q / Q_{max}, open symbols – ejected volume (Q_{max} = 3.82 × 10^{-4} m^3 / s, 0.81 CFM)

The thermal performance of the cross fin flow cooling is compared with the longitudinal cooling as shown by the thermal resistance in Figure 5.18. Identical electromagnetic drivers were used in the two heat sinks, with the same actuation signal. The thermal resistance for the cross fin cooling is normalized with the lowest value for the longitudinal cooling (Θ_o = 2.61 K / W). The lowest thermal resistance for the cross fin cooling is approximately 0.60 Θ_o (Θ = 1.53 K / W). The corresponding convective resistance results in an overall heat transfer coefficient of 45 W / m^2 K. The method for determining h is shown in Appendix B. Longitudinal cooling achieves a heat transfer coefficient of 22 W / m^2 K. As the exit area ratio, $A_{c,v} / A_o$, increases, the thermal resistance decreases. This is somewhat surprising since the volume flow rate decreases as well, however, as shown in Figure 5.15, the suction velocity at the bottom heat spreading surface of the heat sink increases with increasing $A_{c,v} / A_o$. Therefore, even though the overall volume flow decreases, the increase in suction velocity near the heat source leads to an increase in heat transfer. Also, as the frequency is increased, the jets become somewhat asymmetric, with the peak velocity skewed towards the bottom, as shown in Figure 5.19. As f_d increases, the suction velocity at $y / h_o = 0.05$ increases from U / U_{max} = -0.32 to -0.58, while the jet velocity at $y / H = 0.21$ increases from $U / U_{max} = 0.62$ to 1.0. Also as f_d increases, the entrainment velocity for $y / H > 0.8$ increases by 0.07 U_{max} from 150 to 210 Hz. The increased entrainment near the bottom surface (where the heater is located) along with the increased jet velocity near the bottom, results in higher heat transfer. It is conjectured that these trends hold for 210 Hz < f_d < 260 Hz (where Θ becomes saturated).

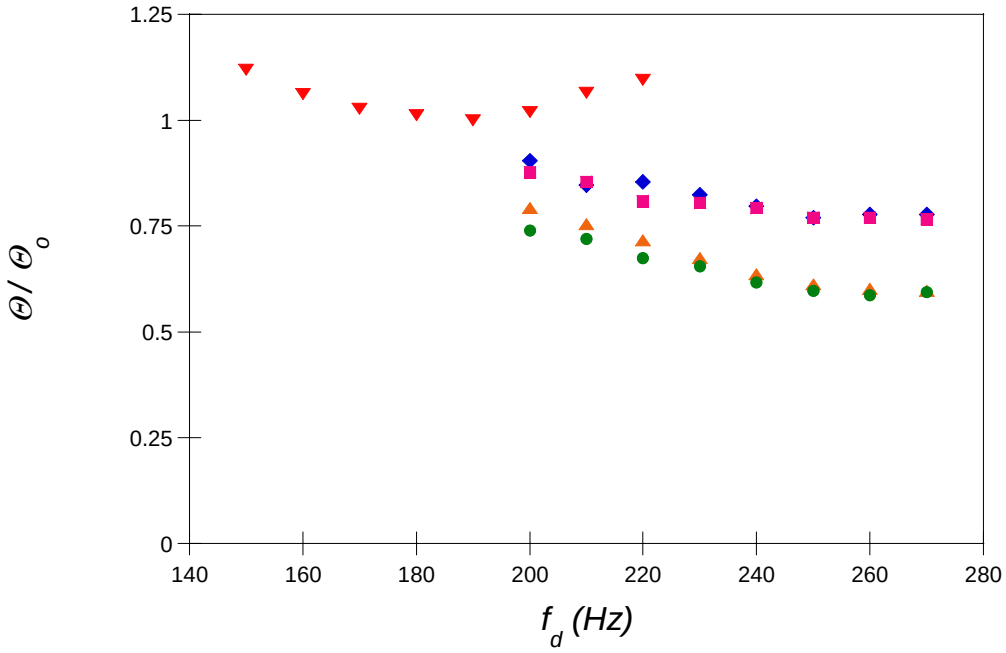

Figure 5.18: Variation of thermal resistance with frequency for cross flow heat sink for $A_{c,v} / A_o$ = 0.87 (◆), 1.02 (■), 1.46 (▲), 1.85 (●), and longitudinal flow heat sink (▼) (actuator voltage held constant)

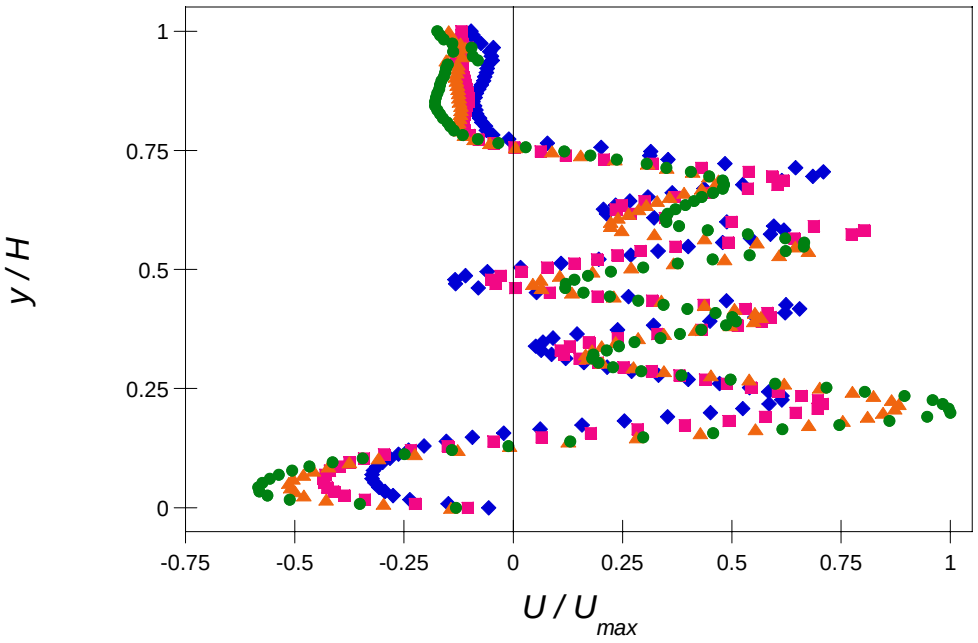

Figure 5.19: Time-averaged streamwise velocity distribution at fin tip for f_d = 150 (◆), 170 (■), 190 (▲), and 210 Hz (●) ($C_p \neq 0$, U_{max} = 0.76 m / s))

The electromagnetic actuator voltage can be varied to increase the amplitude of deflection of the diaphragm, increasing the per cycle volume flow rate, thus providing higher heat transfer. Figure 5.20 shows the thermal resistance for the cross fin cooling when the actuation frequency is held constant but the input voltage is increased for various $A_{c,v} / A_o$ ratios. As $A_{c,v} / A_o$ increases, the thermal resistance decreases by about 20%. The thermal resistance decreases with actuation voltage and levels out as the maximum input to the actuator is reached. The minimum thermal resistance is approximately 50% ($\Theta = 1.25$ K / W) of the resistance of the longitudinally cooled heat sink resulting in an overall heat transfer coefficient of 55 W / m^{2}K.

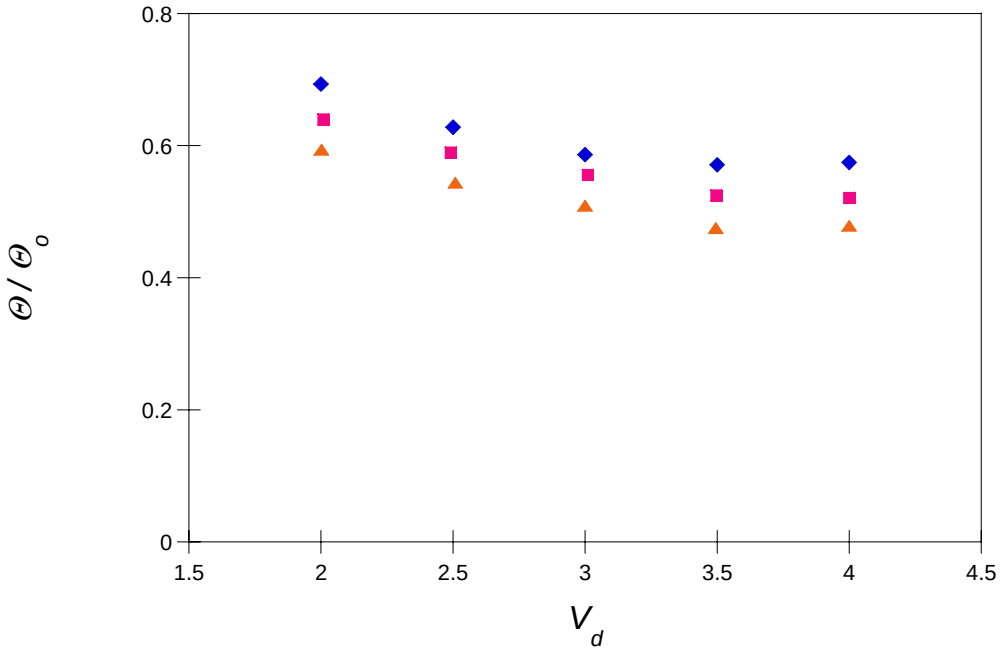

Figure 5.20: Thermal resistance for increasing speaker input voltage for $A_{c,v} / A_o$ = 0.87 (◆), 1.47 (■), and 1.85 (▲) (Θ_o = 2.61 K / W, f_d = 260 Hz)

The thermal resistance of the cross fin cooled heat sink is lower than that of a comparable conventional, fan-cooled heat sink. As an example, the present heat sink is compared

with a commercial heat sink (Aavid, PN3354B, measuring 50.4 × 50.7 × 25 mm) having similar overall dimensions (excluding the flow driver). The envelope volumes of the present and commercial heat sinks are 67.6 cm^3 and 63.9 cm^3, respectively. The thermal resistance of the latter is listed as 2.6 K / W with air flow of 12.7 × 10^{-4} m^3/s (2.7 CFM). These data show that compared to the new synthetic jet design, the commercial heat sink requires 1.6 times the volume flow rate to achieve a thermal resistance that is twice as high, therefore proving to be much less efficient for cooling.

5.6. Radial Heat Sink

The advantages of the cross fin cooling can be further exploited in a radial heat sink configuration. In this design the plane of the electromagnetic actuators is parallel to the heated surface. The radial fins are circumferentially distributed around the perimeter as shown in Figure 5.21, with a section of the fins removed to show the actuator module.

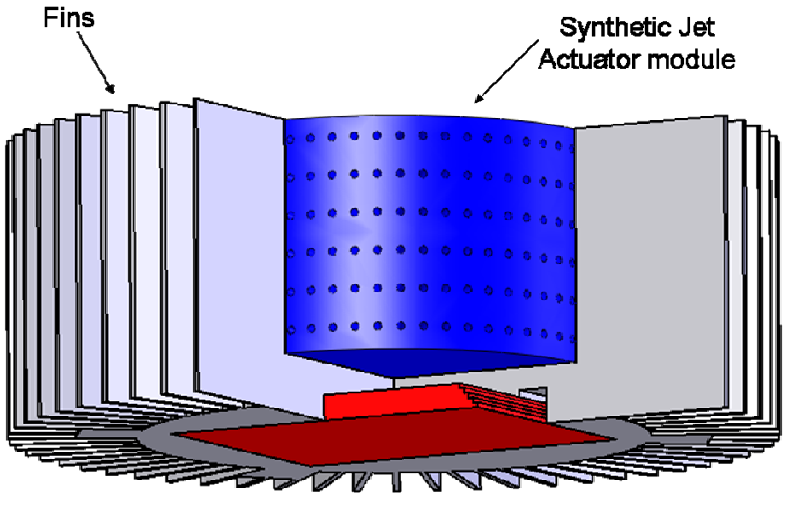

Figure 5.21: Radial heat sink design showing actuator module

The radial design provides several improvements over the straight channel design. First, the heat sink can be scaled up or down more easily. Any number of electromagnetic actuators can be stacked vertically for a finer incremental increase in air flow. Second, since the electromagnetic drivers are mounted parallel to the axis of the orifices, the air flow routing is greatly simplified as shown in Figure 5.22, compared to Figure 5.10. The air flow induced by the moving diaphragm is routed radially outward through an orifice centered between two individual fins. Since all of the orifices have the same diameter, the jets are uniform and the average pressure drop across each diaphragm is zero. Although the overall footprint of the radial design is larger than the straight channel design, the overall volume is smaller for the same number of drivers.

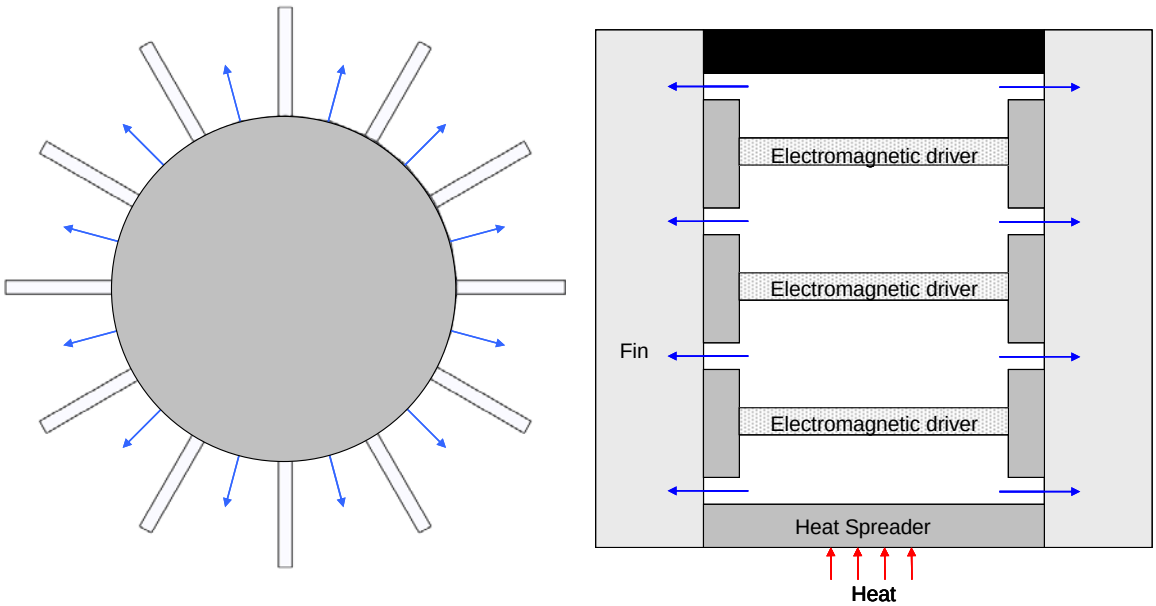

Figure 5.22: Schematic of top view and internal flow routing for radial heat sink

In the present design, the copper heat sink is 50.8 mm in diameter with a total of 60 fins surrounding the core, each 12.7 mm long and 0.9 mm thick. The center is bored out to

allow a SLA module that contains three electromagnetic drivers (the same drivers that are used in the earlier experiments). The fin hub and the heat spreader are each 5.08 mm thick. Foil heaters are attached to the bottom of the heat sink to provide the thermal load and the temperature along the conduction is monitored by T-type thermocouples that are epoxied into the metal.

Distributions of the time-averaged radial air speed at the edges of the fins are shown in Figure 5.23. There are six orifices between the fins at $y / H = 0.22$, 0.36, 0.51, 0.65, 0.79, and 0.92. The diaphragms are operated such that the lowest jet is 180° out of phase of the adjacent two jets which are in phase. These two jets are in turn 180° out of phase with the following two and so on. The bottom jet shows that it entrains air between the fins for $y / H < 0.2$. The top jet acts similarly. Because of the alternating suction and blowing of sequential jets/pairs, there are only two distinct jets that emerge from the heat sink, emanating from the two phase-matched pairs of jets. Because the volume displaced by the two center pairs of jets is greater than the single outer jets, these jets dominate the flow field. The jets that are induced with this heat sink are higher velocity (U_{max} = 1.20 m/s) than with the straight channel cross fin design. This is partly due to the reduced head losses of the simplified flow routing. There is a large region of entrained flow between the two paired orifices ($0.4 < y / H < 0.65$) because of the cross-talk between them. This is partly beneficial in that cool, fresh air is constantly entrained into the system. Figure 5.24 shows the variation of the time-average volume flow rate exiting the radial heat sink for with actuation frequency. As f_d increases, the volume flow rate increases but becomes asymptotic. The maximum volume flow rate is 3.83 CFM, higher than the straight channel design, but the radial design uses three actuators instead of two.

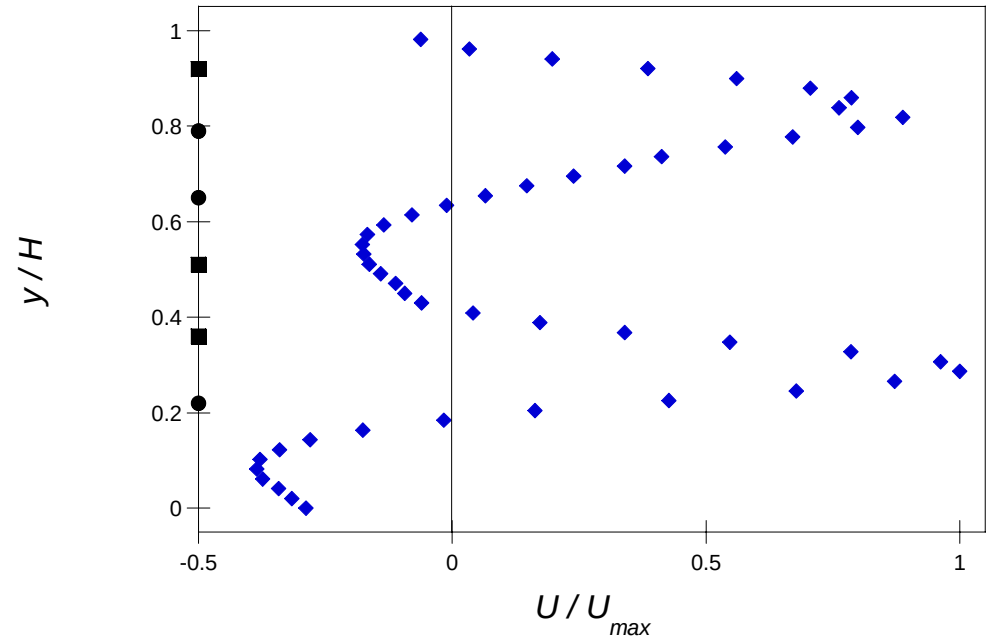

Figure 5.23: Time-averaged radial velocity distribution at fin tip of radial heat sink with orifice locations shown; in-phase orifices denoted by square or circle (f_d = 330 Hz, U_{max} = 1.20 m / s)

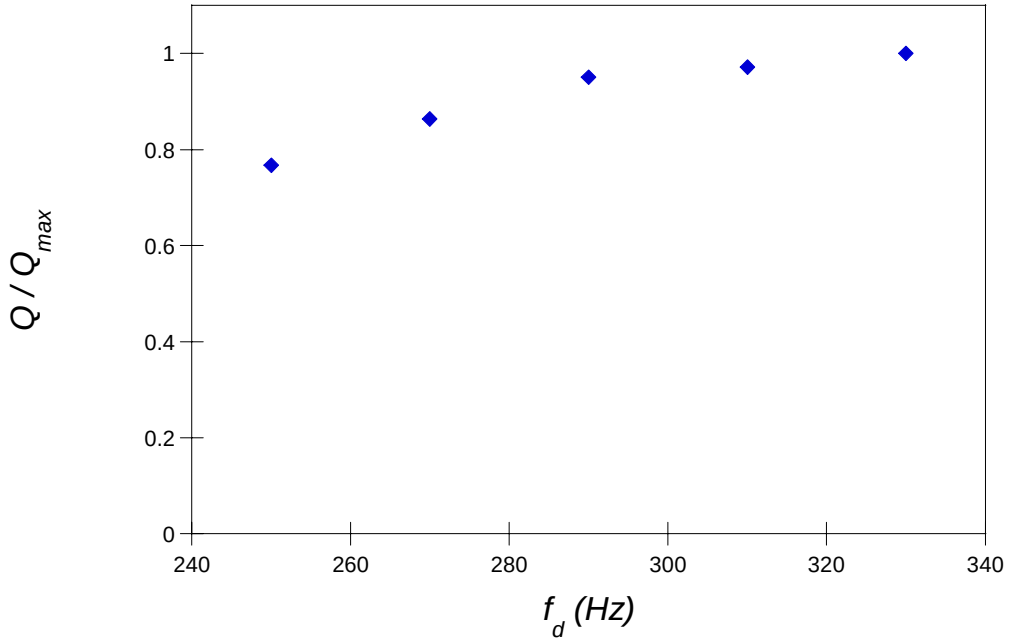

Figure 5.24: Time-averaged volume flow rate exiting between fin pairs of radial heat sink (Q_{max} = 1.81 × 10^{-3} m^3 / s, 3.83 CFM)

The variation of the thermal resistance of the radial heat sink with f_d is shown in Figure 5.25 for fixed actuation amplitude. The thermal resistance depends weakly on frequency (in this range) and there is a minimum thermal resistance at 290 Hz (the thermal resistance is normalized using the minimum thermal resistance obtained with the longitudinal design, $\Theta_o = 2.61$ K / W). The thermal resistance is much lower for all f_d than the other heat sink designs investigated, approximately $\Theta / \Theta_o = 0.3$. To further reduce Θ, the displacement of the actuator's diaphragm is increased for higher flow rates by increasing the actuation voltage. Figure 5.26 shows the affect of increasing V_i at $f_d = 290$ Hz. As the voltage is increased, the thermal resistance decreases linearly to a minimum of $\Theta / \Theta_o = 0.28$. This correlates to a heat transfer coefficient of 72 W / m^2 K using the method described in Appendix B. When the actuator frequency and voltage are held constant and the heater input power, P_i, is increased, the thermal resistance is invariant as shown in Figure 5.27. These data demonstrate that the radial heat has lower thermal resistance than the straight channel heat sinks discussed in §5.3-4 which have a minimum thermal resistance of $\Theta / \Theta_o = 0.48$.

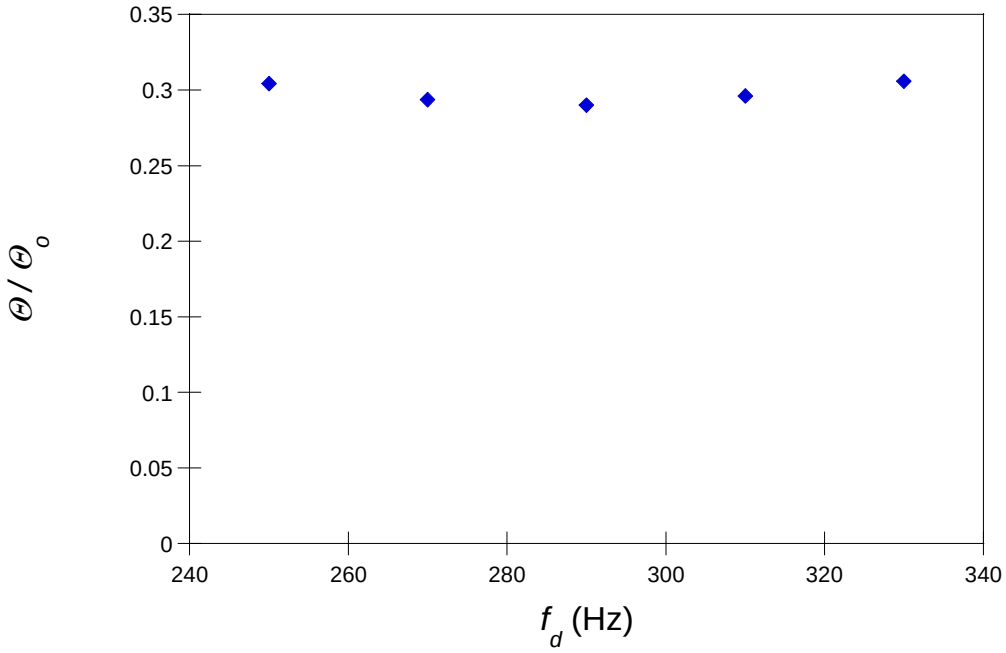

Figure 5.25: Normalized thermal resistance of radial heat sink for various input frequencies (Θ_o = 2.61 K / W, V_i = 8.4 V)

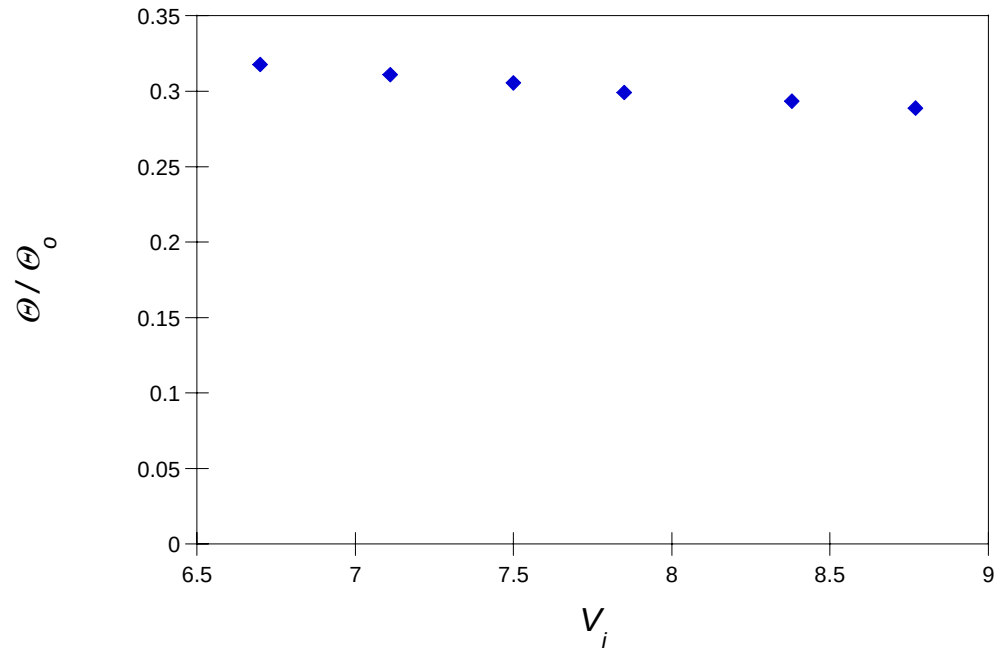

Figure 5.26: Normalized thermal resistance of radial heat sink for various input voltages (Θ_o = 2.61 K / W, f_d = 290 Hz)

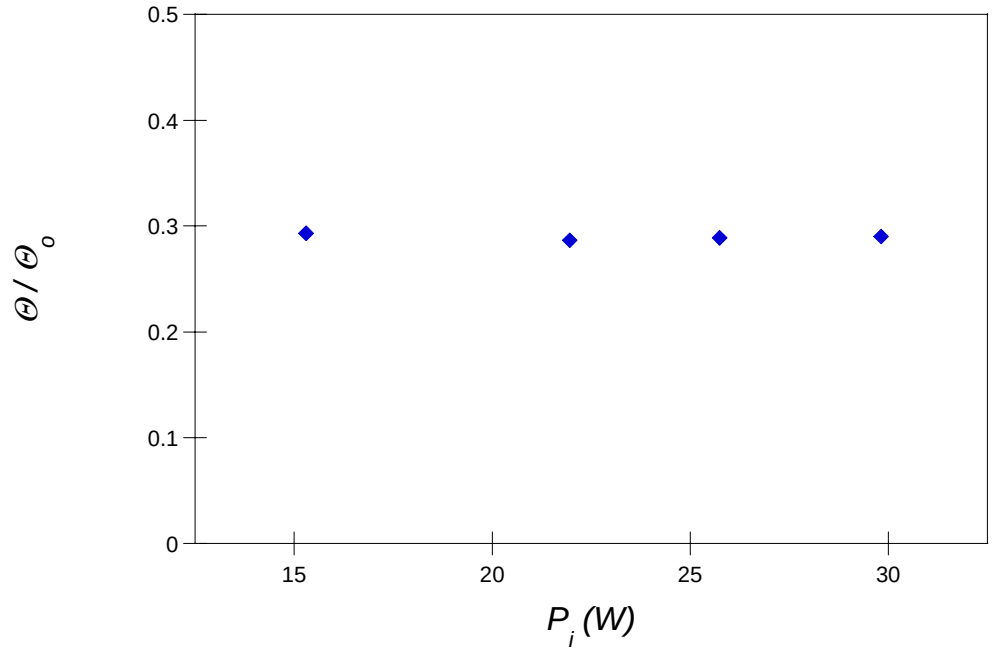

Figure 5.27: Normalized thermal resistance of radial heat sink for various input powers to heat sink (Θ_o = 2.61 K / W, f_d = 290 Hz, V_i = 8.4V)

Chapter 6

Conclusions

Enhanced heat transfer in electronic hardware by direct, small-scale actuation is investigated experimentally in two test bed configurations. The first configuration exploits the unsteady motions induced by a vibrating reed embedded within a heated duct (in contact with hardware that needs cooling) to enhance forced convection transport heat from the duct surfaces. The flow within the duct is either exclusively driven by the reed or, for higher heat flux, is augmented by an induced core flow. The time harmonic motion of the reed results in the regular shedding of vortical structures that interact with the inner surfaces in the absence and presence of a core flow. The second configuration focuses on the effects of small scale motions induced by a synthetic jet on heat transfer within an advanced heat sink. The synthetic jets emanate directly through the base of the heat sink and induce a recirculating flow between the fins, resulting in a lower thermal resistance than what is typically achieved with traditional fans. Of particular interest are the effects of small-scale motions and enhanced mixing on heat transfer compared to conventional time-invariant flows at similar or higher Reynolds numbers.

The flow field and heat transfer enhancement induced by a cantilevered, vibrating, piezoelectric reed mounted in a high aspect ratio channel is investigated experimentally. The vibrating reed induces a reverse Kármán vortex street with a Reynolds number of 600. The flow small-scale mixing inherent in this flow results in an increase in the heat transfer capability compared to steady flow at the same Reynolds number.

The reed is constructed from a thin metal shim bonded with piezoelectric plates that are operated in a shearing mode, oscillating the reed. During each half cycle, as the reed moves away from one the channel surfaces the tip motion results in the formation and shedding of a vortex whose sense is such that it rolls up towards the gap between the reed and the wall. The vortex center does not move downstream until the reed reaches its closest proximity to the opposite surface and begins to move back. The vortex moves towards the opposite surface of the channel as it begins to be advected downstream by its own self-induced channel velocity. The process repeats during the second half of the cycle where an opposite sense vortex is formed around the tip of the reed. The time-averaged vorticity field indicates that the highest vorticity occurs just between the tip of the reed and the adjacent surface.

The peak time-averaged streamwise velocity in the channel occurs at the centerline near the tip of the reed, whereas farther downstream, there are two local peaks near each of the walls as a result of the advection of the counter rotating vortices. By increasing the peak to peak amplitude ($A_{p\text{-}p}$) of the reed deflection, the induced volume flow rate increases, and then saturates at approximately $A_{p\text{-}p} / h_o = 0.45$ possibly owing to reed blockage. Near the walls, there is a domain of reversed flow adjacent to the tip of the reed, and as $A_{p\text{-}p}$ decreases, this domain extends farther into the center of the channel.

The unsteady flow induced by the reed results in substantial Reynolds stresses along the channel. The maximum $u'u'$ occurs near the channel walls adjacent to the tip and the maximum $v'v'$ is in the center of the channel just downstream from the tip. Distributions

of the time-averaged turbulent kinetic energy indicate high levels of small-scale mixing throughout the channel that lead to higher heat transfer from the channel walls.

The static pressure along the channel wall (in the center plane) is within the range of 0 - 10 Pa. The minimum pressure occurs just upstream of the tip, and the pumping motion induced by the reed leads to an increase in head (above atmospheric). An increase in the channel length and pressure drop results in a linear decrease in volume flow rate.

Configurations of tandem and parallel reeds were also investigated. When the two reeds are placed in tandem the estimated volume flow rate increases by approximately 35% compared to a single reed. Within the constraints of the present setup, this change in the volume flow rate appears to be insensitive to the reed spacing or phase difference between the two reeds. It is noteworthy that actuation by tandem reeds provides an increase in total head.

The interaction of two reeds in parallel is affected by the phase difference between them. When the reeds are operated in-phase, the time-averaged velocity distribution indicates that the peak velocity induced by each reed moves closer to the walls and the velocity distribution is similar to the distribution of a single reed. Changing the phase difference increases the peak time-averaged velocity and skews it towards one wall, while creating a deficit at the other wall. For $\Delta\Phi = 90°$ (bottom reed leading), the peak velocity increases by 15% and shifts towards the bottom wall while creating a deficit near the top wall. The volume flow rate obtained with two reeds is *more than twice* the flow rate achieved with a single reed. The phase-averaged vorticity field shows that for $\Delta\Phi = 0°$, because there is

no separation between the two reeds, only two (total) vortices are created for each cycle. For $\Delta\Phi = 180°$, two pairs of counter-rotating vortices are formed. It is likely that the vortex formation for $\Delta\Phi = 180°$ will result in higher heat transfer than for $\Delta\Phi = 90°$.

The effect of altering the spanwise spacing between the reed and the sidewalls was also investigated. Although most of the experiments use a width ratio, $w / w_r = 1.1$, it is shown that the maximum volume flow rate at the exit is obtained at $w / w_r = 1.2$ and is invariant at larger widths. Increasing the gap between the reed and wall results in a secondary velocity peak near the sidewalls in the proximity of the tip. This secondary velocity peak is the result of air being pushed spanwise by the oscillating reed, and could result in enhanced mixing of the air near the tip, resulting in higher heat transfer.

The effect of the reed in the presence of a bulk flow was also investigated using bulk flow rates that are 1 - 3 times the flow induced by a single reed. For $Q_{st} = 0.35$ CFM (comparable to reed-induced flow, $Re = 381$), the vortices do not migrate across the channel following the reed. When Q_{st} is increased, vortex formation occurs farther downstream from the tip. At $t / T = 0.33$, the vortex formation moves from $x / h_o = 0$ to 0.8 by increasing Q_{st} from 0.35 to 1.06 CFM, ($Re = 1140$). Perhaps the most remarkable effect of the actuation is the increase in KE_f. The vibrating reed introduces significant small scale motions and mixing. For increasing Q_{st} the KE_f propagates farther downstream likely increasing local heat transfer along the entire channel.

A channel similar to that used in the fluid experiments was constructed to measure the effects of the reed-induced flow on the local heat transfer, in the absence and presence of

bulk flow. The reed introduces small scale motions and mixing that substantially enhances heat transfer over steady flow at the same Reynolds number.

The present measurements show that for the reed-induced flow the minimum thermal resistance occurs at $x / h_o = 0.83$ for all $A_{p\text{-}p}$, the same location that the flow experiments indicated high levels of cross stream velocity transport. As $A_{p\text{-}p}$ is increased the thermal resistance decreases linearly for $A_{p\text{-}p} / h_o < 0.45$. For $A_{p\text{-}p} / h_o > 0.45$ the decrease is reduced. The Nu increases with downstream distance, achieving a maximum of 19.1 at the channel exit for $A_{p\text{-}p} / h_o = 0.75$. Finally, for the maximum reed-induced Q, ($Q = 0.35$ CFM) the reed reduces the thermal resistance of the surface by nearly 50% over that of steady flow.

In the presence of a bulk flow, the reed significantly augments the heat transfer within the channel compared to what is achieved by the reed alone. The temperature distribution of the air exiting the channel shows more uniformity for the reed-augmented flow over steady flow, verifying that the reed mixes the heated air with the core flow. The average temperature of the exhaust air is ~30% higher for reed-augmented flow at $Q_{st} = 0.3$ CFM ($Re = 320$), but this increase diminishes with increasing Q_{st} due to the decrease in residence time. The reed-augmented flow disrupts the thermal boundary that limits the heat transfer in steady flow as shown by the streamwise temperature distribution. The streamwise length required for full mixing increases with Q_{st}.

The surface thermal resistance in steady flow increases along the length of the channel, whereas the reed-augmented flow resistance decreases by up to 43% from the tip to exit

for $Q_{st} = 1.07$ CFM ($Re = 1140$). The highest convection coefficient obtained is 71 W / m^2 K, with a corresponding $Nu_{D_h} = 28.5$.

The vibrating reed technology appears to be suitable for scaling (up or down), but such scaling poses some challenges. For small-scale hardware (e.g., hand held), the reed must be effectively scaled down to provide cooling enhancement. As shown in §4.3, even small vibration amplitudes disrupt the thermal boundary layer, and lead to an increase in heat transfer. Also, the blade material can be selected to optimize the deflection. In addition, it may be important to protect the duct to prevent degradation of its performance by environmental conditions (water, dust, etc.).

Finally, the effects of induced small scale motions on the flow within channel that are formed by heat sinks fins are investigated using several active heat sink configuration that use synthetic jet actuation. In the first configuration the jets flow longitudinally along the length of the fins. This approach results in significant flow bypass and the cooling air exits the channel about 0.25 H from the inlet. The flow bypass can be reduced by canting the jets towards the base of the fins, but this creates a recirculating flow within the channel. The lowest thermal resistance obtained with this design is 2.61 K / W.

Improved heat transfer utilizes a similar heat sink where the synthetic jets entrain air through orifices within the base of the fin channels. This method results in cellular pockets of recirculating air moving across the (short) lateral length of the fins that eliminate the bypass and entrain cool air directly.

The jet orifice size was varied to maximize the flow rate for a given jet driver. It is shown that by controlling the pressure difference across the actuators' diaphragm and it operating frequency, it is possible to alter the cross fin velocity distribution along the length of the fin and with it the heat transfer characteristics.

The minimum thermal resistance obtained with the cross fin configuration is 1.25 K / W. This was obtained with a higher operating frequency ($f_d = 270$ Hz) at which the time-averaged velocity distribution is skewed such that the highest entrainment velocity (inflow) and the highest jet velocity (outflow) are near the bottom of the heat sink (and the heat load).

This thermal resistance is much lower than what is obtained with a comparable commercial fan-driven heat sink having a similar volume. Even with a volume flow rate that is approximately 50% higher than that obtained with the synthetic jets (2.7 CFM), the commercial heat sink has a thermal resistance of 2.6 K / W.

Finally, this cross fin approach is implemented in a radial heat sink. Because the jet drivers are housed within the hub the flow passage to the jet orifices are greatly simplified. This design can be easily scaled to allow for the more actuators, and the radial fins result in a larger cooling surface area. As a result of the lower pressure drop, the total flow rate increases by 50% per actuator and the minimum thermal resistance is 0.78 K / W.

Appendix A

First-order Unimorph Resonant Frequency Calculation

The governing equations of a cantilevered beam are used to guide the selection of the shim material and PER size. The analysis performed by Timoshenko (1955) and summarized by Jacobson (1995) is used. To determine the resonant frequency of the combined beam, the composite cantilever flexural rigidity (*EI*) must be determined. For this analysis, the epoxy bondline between the piezo-ceramic and the shim material is ignored. Also, this analysis assumes that the cross-section remains the same along the length. Figure A.1 shows the cross section of the cantilevered beam.

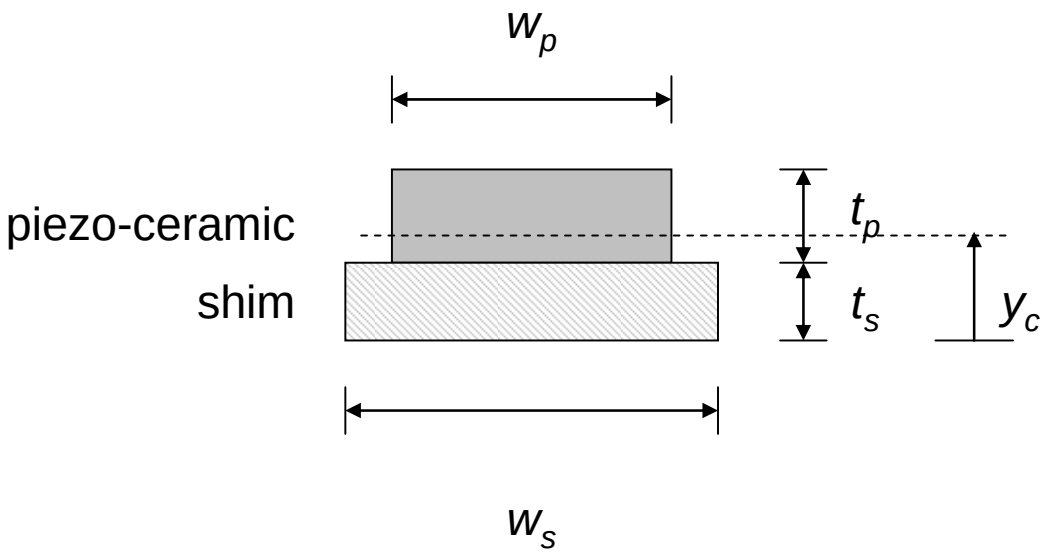

Figure A.1: Cross-section of composite cantilever beam

To simplify the calculation, an adjusted width, w_p', is determined for the piezo-ceramic so that it has the same Young's modulus (*E*) as the shim material (Beer and Johnston, 1992).

$$w_p' = \frac{w_p E_p}{E_s} \tag{A.1}$$

where the subscript p denotes the piezo-ceramic and s denotes the shim material. Next, the centroid (y_c) of the combined cross-section is determined by:

$$y_c = \frac{t_s}{2} + \frac{t_p}{2}\left(\frac{t_s + t_p}{\frac{w_s t_s}{w_p'} + t_p}\right) \tag{A.2}$$

where t is the thickness of the denoted material. Next, the moment of inertia is determined for the composite beam from the equation:

$$I' = \left[\frac{w_s t_s^3}{12} + w_s t_s\left(y_c - \frac{t_s}{2}\right)^2\right] + \left[\frac{w_p' t_p^3}{12} + w_p' t_p\left(y_c - \left(\frac{t_p}{2} + t_s\right)\right)^2\right] \tag{A.3}$$

The composite flexural rigidity is then:

$$EI = E_s I' \tag{A.4}$$

Using the beam mass per unit length (γ):

$$\gamma = \rho_s w_s t_s + \rho_p w_p t_p \tag{A.5}$$

and knowing the beam length (l), we can use the extensive work of Timoshenko to determine that the resonant frequency of a cantilevered unimorph beam is:

$$f_{res} = \frac{3.515}{2\pi}\sqrt{\frac{EI}{\gamma l^4}} \tag{A.6}$$

Table A.1 shows the material properties that were used for the parameterization of the cantilevered beam for various thicknesses, lengths, and materials. The results are shown in Figure A.2 and Figure A.3. The resonant frequency is a linear function of the thickness of the material, and a function of $L^{0.5}$. For a constant thickness, the material selection is less important, with brass and copper having nearly identical f_{res}, as a result of the factor ρ / Y being ~15% different. Aluminum, steel and Inconel 600 are even more similar, with ρ / Y varying by < 8.6%.

Table A.1: Reed material properties

Material	Young's Modulus of Elasticity (GPa)	Density (kg / m^3)	ρ / Y ($\times 10^9$)	d_{31}
PZT-5H	62	7800	125.8	3.2×10^{-10}
Brass	105	8470	80.7	
Copper	120	8470	70.6	
Aluminum	73	2800	38.4	
Steel	190	7920	41.7	
Inconel 600	207	8470	40.9	

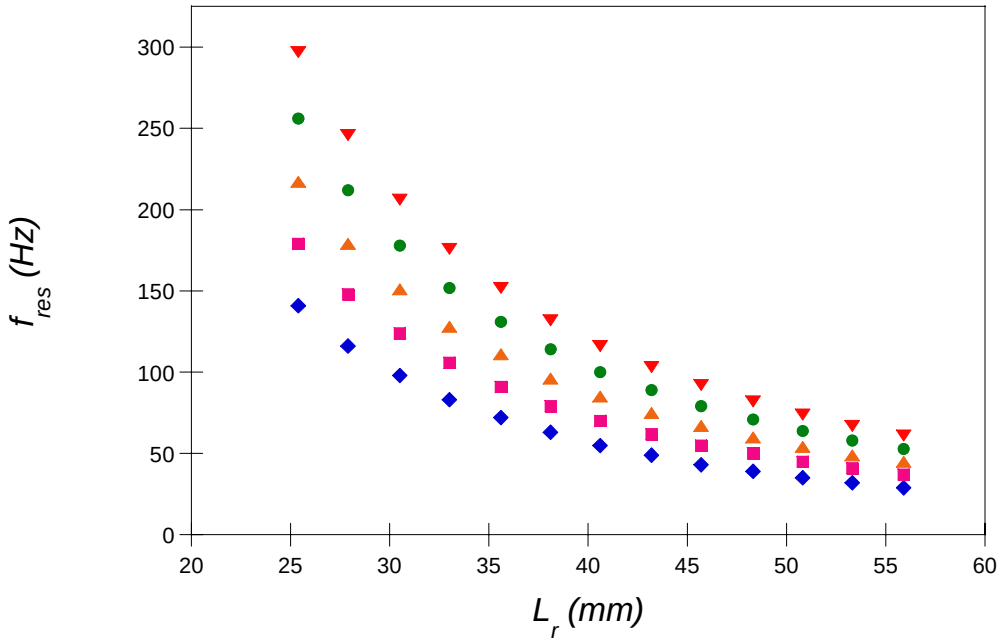

Figure A.2: PER resonant frequency vs. reed shim length for various brass shim thicknesses; t_r = 0.05 mm (◆), 0.10 mm (■), 0.15 mm (▲), 0.20 mm (●) and 0.25 mm (▼)

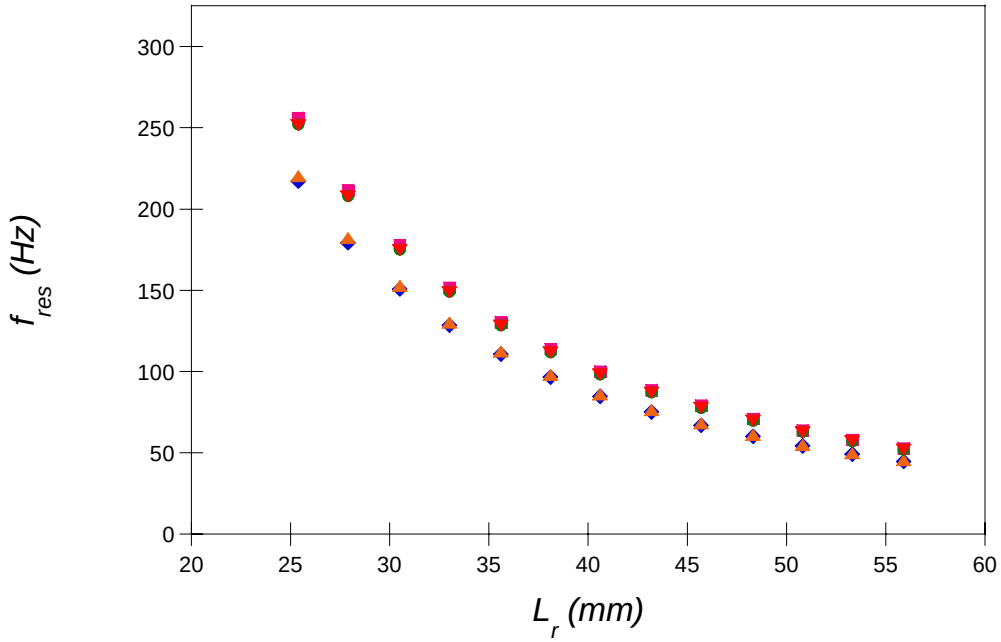

Figure A.3: PER resonant frequency vs. reed shim length for various shim materials; brass (◆), aluminum (■), copper (▲), steel (●), and Inconel 600 (▼), (t_r = 0.15 mm)

Appendix B

Calculation of Heat Sink Resistances

Figure B.1 displays the thermal resistance network between the base of heat sink and the airflow between the fins of a heat sink. The air enters between the fins at temperature T_{amb}, is heated and exits at temperature T_{exit}. It is assumed that the temperature of the fins and the temperature of the heat sink base are uniform.

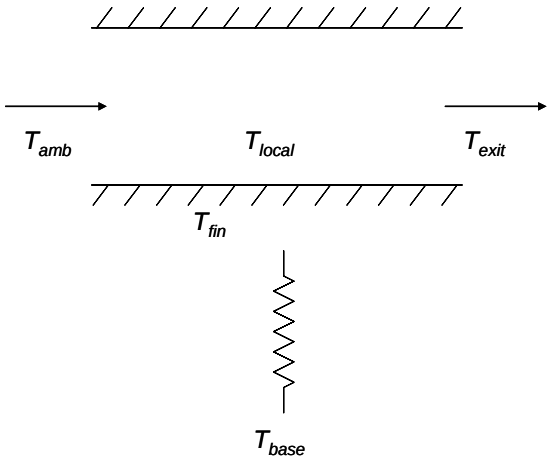

Figure B.1 Thermal resistance model from heat sink base to airflow through fins

The total thermal resistance of a heat sink is:

$$\Theta_{tot} = \frac{T_{base} - T_{amb}}{Q_{tot}} \tag{B.1}$$

where Q_{tot} is the input power into the heat sink base. Equation B.2 is equivalent by adding and subtracting the T_{fin} and T_{local}.

$$\Theta_{tot} = \frac{T_{base} - T_{fin} + T_{fin} - T_{local} + T_{local} - T_{amb}}{Q_{tot}} \tag{B.2}$$

The first two temperatures can be combined and the terms rewritten as spreading resistance, Θ_{sp}. The middle two temperatures can be combined, and using Newton's law of cooling, can be substituted for convective resistance, $1 / h A_f$. The last two temperatures constitute the resistance due to mass flow. The local temperature can be approximated as the average of the inlet and exit temperatures. Equation B.2 can now be reduced as the following:

$$\Theta_{tot} = \Theta_{sp} + \frac{1}{hA_f} + \frac{\frac{T_{exit} + T_{amb}}{2} - T_{amb}}{Q_{tot}} \tag{B.3}$$

which simplifies to:

$$\Theta_{tot} = \Theta_{sp} + \frac{1}{hA_f} + \frac{T_{exit} - T_{amb}}{2Q_{tot}}\,. \tag{B.4}$$

To simplify the last term, the total heat removed by the airflow, Q_{tot}, is shown in Equation B.5.

$$Q_{tot} = \dot{m} c_p (T_{exit} - T_{amb}) \Rightarrow \frac{T_{exit} - T_{amb}}{Q} = \frac{1}{\dot{m} c_p} \tag{B.5}$$

Equation B.4 now reduces to:

$$\Theta_{tot} = \Theta_{sp} + \frac{1}{hA_f} + \frac{1}{2\dot{m}c_p} \tag{B.6}$$

Equation B.6 only contains explicit flow and geometric terms, except for the spreading resistance. This is calculated by using the following equations.

$$\Theta_{sp} = f_1 f_2 \tag{B.7}$$

$$\lambda = \frac{\pi^{1.5}}{\sqrt{A_p}} + \frac{1}{\sqrt{A_s}} \tag{B.8}$$

$$B = \tanh(\lambda t) \tag{B.9}$$

$$\lambda_{k,A_p} = A_p k R_o \lambda \tag{B.10}$$

$$f_1 = \frac{B + \lambda_{k,A_p}}{1 + B\lambda_{k,A_p}} \tag{B.11}$$

$$f_2 = \frac{\sqrt{A_p} - \sqrt{A_s}}{k\sqrt{\pi A_p A_s}} \tag{B.12}$$

In the above, A_p is the area of the base plate to which the fins are attached, A_s is the area of the heat source, t is the thickness of the base plate, k is the conductivity of the heat sink, and R_o is the sink to ambient theta, also sometimes named the average heat sink

thermal resistance. This term is dependent on the geometry and material properties of the heat sink. It is often arbitrary in its affect to the total thermal resistance.

Using the above analysis to predict the total thermal resistance requires calculation of several terms and approximation of others. To start, the mass flow rate of air has to be accurately measured prior to the experiment. As noted, the local temperature is also approximated by the average between inlet and exit temperatures. The convective coefficient usually is not known, so an approximation is often used. This term is the hardest to correctly approximate, so it can instead be determined after the experimental total thermal resistance is found and backing it out of all of the equations.

REFERENCES

Açikalin, T., Raman, A. and Garimella, S. V. (2003). "Two-dimensional streaming flows induced by resonating, thin beams." *Journal of the Acoustical Society of America* **114**(4 I): 1785.

Açikalin, T., Sauciuc, I. and Garimella, S. V. (2005). Piezoelectric actuators for low-form-factor electronics cooling, Proceedings of the ASME Summer Heat Transfer Conference, San Francisco, CA, United States, American Society of Mechanical Engineers, New York, NY **2**: 939.

Adrian, R. J. (1991). "Particle-Imaging techniques for experimental fluid mechanics." *Annual Review of Fluid Mechanics* **23**: 261.

Akhtar, I. and Mittal, R. (2005). "A Biologically Inspired Computational Study of Flow Past Tandem Flapping Foils."

Anderson, J. M., Streitlien, K., Barrett, D. S. and Triantafyllo, M. S. (1998). "Oscillating foils of high propulsive efficiency." *Journal of Fluid Mechanics* **360**: 41.

Bar-Cohen, A. (2000). "Computer-Related Thermal Packaging at the Millennial Divide." *Electronics Cooling* **6**(1): 8.

Biswas, G., Torii, K., Fujii, D. and Nishino, K. (1996). "Numerical and experimental determination of flow structure and heat transfer effects of longitudinal vortices in a channel flow." *International Journal of Heat and Mass Transfer* **39**(16): 3441.

Blackwelder, R. F., Liu, D. and Jeon, W. (1998). "Velocity perturbations produced by oscillating delta wing actuators in the wall region." *Experimental Thermal and Fluid Science* **16**(1-2): 32.

Brockmeier, U., Fiebig, M., Guentermann, T. and Mitra, N. K. (1989). "Heat transfer enhancement in fin-plate heat exchangers by wing type vortex generators." *Chemical Engineering & Technology* **12**(4): 288.

Bürmann, P., Raman, A. and Garimella, S. V. (2002). "Dynamics and topology optimization of piezoelectric fans." *IEEE Transactions on Components and Packaging Technologies* **25**(4): 592.

Cattafesta III, L. N., Garg, S. and Shukla, D. (2001). "Development of piezoelectric actuators for active flow control." *AIAA Journal* **39**(8): 1562.

Chang, M. Y. and Lin, T. F. (1998). "Experimental study of aspect ratio effects on longitudinal vortex flow in mixed convection of air in a horizontal rectangular duct." *International Journal of Heat and Mass Transfer* **41**(4-5): 719.

Edwards, F. J. and Alker, C. J. R. (1974). Improvement of forced convection surface heat transfer using surface protrusions in the form of (A) cubes and (B) vortex generators. Proceedings of the Fifth International Heat Transfer Conference, Tribune du CEBEDEAU (Centre Belge d'Etude et de Documentation des Eaux), Tokyo, Jpn, Jpn Soc of Mech Eng, Tokyo: 244.

Fiebig, M., Brockmeier, U., Mitra, N. K. and Guntermann, T. (1989). "Structure of velocity and temperature fields in laminar channel flows with longitudinal vortex generators." *Numerical Heat Transfer* **15**(3): 281.

Garg, J., Arik, M., Weaver, S., Wetzel, T. and Saddoughi, S. (2005). "Meso scale pulsating jets for electronics cooling." *Journal of Electronic Packaging, Transactions of the ASME* **127**(4): 503.

Gopalkrishnan, R., Triantafyllou, M. S., Triantafyllou, G. S. and Barrett, D. (1994). "Active vorticity control in a shear flow using a flapping foil." *Journal of Fluid Mechanics* **274**: 1.

Hodges, D. H. and Pierce, G. A. (2002). Introduction to structural dynamics and aeroelasticity. New York, Cambridge University Press.

Honohan, A. (2003). The Interaction of Synthetic Jets with Cross Flow and the Modification of Aerodynamic Surfaces. Mechanical Engineering. Atlanta, Georgia Institute of Technology. **Ph.D**.

Ihara, A. and Watanabe, H. (1994). "On the flow around flexible plates, oscillating with large-amplitude." *Journal Of Fluids And Structures* **8**(6): 601.

Incropera, F. P. and DeWitt, D. P. (1996). Fundamentals of Heat and Mass Transfer. New York, John Wiley & Sons. Inc.

ITRS (2001). International Technology Roadmap for Semiconductors. Semiconductors Industries Association Report.

Jacobson, S. A. (1995). An experimental investigation towards the active control of turbulent boundary layers. Mechanical Engineering, Stanford University. **Ph.D:** 262.

Jambunathan, K., Lai, E., Moss, M. A. and Button, B. L. (1992). "A review of heat transfer data for single circular jet impingement." *International Journal of Heat and Fluid Flow* **13**(2): 106.

Kakaç, S., Shah, R. K. and Aung, W. (1987). Handbook of single-phase convective heat transfer. New York, Wiley.

Kays, W. M. and Crawford, M. E. (1980). Convective Heat and Mass Transfer. New York, McGraw-Hill.

Kimber, M., Garimella, S. V. and Raman, A. (2007). "Local heat transfer coefficients induced by piezoelectrically actuated vibrating cantilevers." *Journal of Heat Transfer* **129**(9): 1168.

Lasance, C. J. M. and Aarts, R. M. (2008). "Synthetic Jet Cooling Part I: Overview of Heat Transfer and Acoustics". *24th IEEE SEMI-THERM Symposium*. San Jose, CA.

Lasance, C. J. M., Aarts, R. M. and Ouweltjes, O. (2008). "Synthetic Jet Cooling Part II: Experimental Results of an Acoutic Dipole Cooler." *24th IEEE SEMI-THERM Symposium*, San Jose, CA.

Li, J. G. (1996). A Mechanism for Heat Transfer Enhancements by Vortex Shedding. Fluids Engineering Division Conference, FED, San Diego, California, ASME **239**: 533.

Lighthill, M. J. (1960). "Note on swimming of slender fish." *Journal of Fluid Mechanics* **9**(Part 2): 317.

Lighthill, M. J. (1969). "Hydromechanics of aquatic animal propulsion." *Annual Review of Fluid Mechanics* **1**: 413.

Lighthill, M. J. (1971). Large-amplitude elongated-body theory of fish locomotion. Proceedings of the Royal Society of London. Series B, Biological Sciences, **179**: 125.

Mahalingam, R. and Glezer, A. (2001). An actively cooled heat sink integrated with synthetic jets, Proceedings of the National Heat Transfer Conference, Ananheim, CA, American Society of Mechanical Engineers, New York, NY **1**: 199.

Mahalingam, R. and Glezer, A. (2005). "Design and thermal characteristics of a synthetic jet ejector heat sink." *Journal of Electronic Packaging, Transactions of the ASME* **127**(2): 172.

Mathew, J., Qi, S., Sankar, B. V., Sheplak, M. and Cattafesta III, L. N. (2006). "Optimized design of piezoelectric flap actuators for active flow control." *AIAA Journal* **44**(12): 2919.

Moon, J. W., Kim, S. Y. and Cho, H. H. (2005). "Frequency-dependent heat transfer enhancement from rectangular heated block array in a pulsating channel flow." *International Journal of Heat and Mass Transfer* **48**(23-24): 4904.

Olayiwola, B. and Walzel, P. (2008). "Cross-flow transport and heat transfer enhancement in laminar pulsed flow." *Chemical Engineering and Processing: Process Intensification* **47**(5): 929.

Raffel, M., Willert, C. E. and Kompenhans, J. (1998). Particle image velocimetry : a practical guide Berlin, Springer.

Russell, C. M. B., Jones, T. V. and Lee, G. H. (1982). Heat Transfer enhancement using vortex generators, Heat Transfer, Proceedings of the International Heat Transfer Conference, Munich, Ger, Hemisphere Publ Corp, Washington, DC: 283.

Russell, G. B., Black, W. Z., Glezer, A. and Hartley, J. G. (1999). Microjet cooling of single level integrated modules, 5th International Workshop Thermal Investigations of ICs and Systems, Rome, Italy, TIMA Lab: 72.

Sano, M. (2003). "Enhancement of heat transfer in a turbulent channel flow with insertion of a flat body." *Heat Transfer - Asian Research* **32**(4): 354.

Schmidt, R. R. (1994). Local and average transfer coefficients on a vertical surface due to convection from a piezoelectric fan, Proceedings of the Intersociety Conference on Thermal Phenomena in Electronic Systems, Washington, DC, Publ by IEEE, Piscataway, NJ: 41.

Smith, B. L. and Glezer, A. (1998). "Formation and evolution of synthetic jets." *Physics of Fluids* **10**(9): 2281.

Smyth, R. and Salman, Y. K. (1991). "Combined free and forced convection heat transfer in a rectangular duct." *International Communications in Heat and Mass Transfer* **18**(5): 669.

Tanaka, T., Itoh, M., Hatada, T. and Matsushima, H. (2003). "Influence of inclination angle, attack angle, and arrangement of rectangular vortex generators on heat transfer performance." *Heat Transfer - Asian Research* **32**(3): 253.

Theodorsen, T. (1934). General theory of aerodynamic instability and the mechanism of flutter Langley, VA, U.S. Advisory Committee for Aeronautics.

Thompson, M. R., Denny, D. L., Black, W. Z., Hartley, J. G. and Glezer, A. (1997). Cooling of microelectronic devices using synthetic jet technology, 11th European Microelectronics Conference. Proceedings, Venice, Italy, ISHM-Italy: 362.

Tiggelbeck, S., Mitra, N. K. and Fiebig, M. (1991). Flow structure and heat transfer in a channel with multiple longitudinal vortex generators, American Society of Mechanical Engineers, Heat Transfer Division, (Publication) HTD, Atlanta, GA, Publ by ASME, New York, NY **182**: 79.

Timoshenko, S. (1955). Vibration problems in engineering. New York, Van Nostrand.

Toda, M. (1979). "Theory of air flow generation by a resonant type PVF/2 bimorph cantilever vibrator." **22**(3-4): 911.

Triantafyllou, M. S., Triantafyllou, G. S. and Yue, D. K. P. (2000). "Hydrodynamics of fishlike swimming." *Annual Review of Fluid Mechanics* **32**: 33.

Turk, A. Y. and Junkhan, G. H. (1986). Heat transfer enhancement downstream of vortex generators on a flat plate, Heat Transfer, Proceedings of the International Heat Transfer Conference, San Francisco, CA, USA, Hemisphere Publ Corp, Washington, DC, USA **6**: 2903.

Yao, K. and Uchino, K. (2001). "Analysis on a composite cantilever beam coupling a piezoelectric bimorph to an elastic blade." *Sensors and Actuators, A: Physical* **89**(3): 215.

Yoo, J. H., Hong, J. I. and Cao, W. (2000). "Piezoelectric ceramic bimorph coupled to thin metal plate as cooling fan for electronic devices." *Sensors and Actuators, A: Physical* **79**(1): 8.

Zhu, J. X., Mitra, N. K. and Fiebig, M. (1993). "Effects of longitudinal vortex generators on heat transfer and flow loss in turbulent channel flows." *International Journal of Heat and Mass Transfer* **36**(9): 2339.

Zhu, Q., Wolfgang, M. J., Yue, D. K. P. and Triantafyllou, M. S. (2002). "Three-dimensional flow structures and vorticity control in fish-like swimming." *Journal of Fluid Mechanics* **468**(468): 1.

VITA

Donavon Gerty was born on June 25, 1978 in Columbus, Ohio to Robert and Melinda Gerty. After being impressed by work in a wind tunnel, he decided to pursue a degree in mechanical engineering at University of Dayton. After receiving his Bachelor's of Mechanical Engineering in a terrible ice storm in December 2000, he moved to Atlanta to attend Georgia Institute of Technology where he worked for Dr. Ari Glezer in the Fluid Mechanics Research Lab. A short eight years later, he earned his Ph.D. in December 2008. Assuming that the security clearance goes through, he'll be starting his illustrious career at Sandia National Labs in Albuquerque, NM.